Cold Atom Manipulation for Quantum Computing and Control

A Thesis
Presented to
The Academic Faculty

by

Jacob A. Sauer

In Partial Fulfillment
of the Requirements for the Degree
Doctor of Philosophy

School of Physics
Georgia Institute of Technology
August 2004

Cold Atom Manipulation for Quantum Computing and Control

Approved by:

_____

Alex Kuzmich

_____

Michael S. Chapman, Advisor

_____

Brian Kennedy

_____

Chandra Raman

_____

David. S. Citrin

Date Approved ___August 26, 2004___

For all that we are a part of...

ACKNOWLEDGEMENTS

I would like to begin by thanking Professor Michael S. Chapman for his patience and understanding throughout my graduate career at Georgia Tech. Mike has a very diverse background that allows him to understand problems from many different angles. His insight often prevents us from spending great amounts of time searching in the wrong place for an answer. Without his leadership and positive words of encouragement, none of the work in this thesis would have been possible.

I would also like to thank Professor Murray Barrett for his help in setting up the laboratory and for sharing much of his expertise in electronics and optics with me. Murray began as Mike's first graduate student only one year before I started and laid a large part of the foundation for the laboratory. He brought with him knowledge, experience, and determination that proved very successful in his graduate work. I feel honored to have had Murray as my mentor and friend.

In the latter portion of my Ph.D. work, I have had the pleasure to work with three very wonderful and talented people. Kevin Fortier has worked most closely with me on the cavity QED experiment. His dedication and determination are truly appreciated. Ming Shien Chang joined the lab to work on the BEC experiment as Murray was leaving. Ming Shien's diligence is has truly amazed all of us in the lab. Chris Hamley joined the lab in the middle of my graduate career as an undergraduate. His well of knowledge appears to have no bottom. Chris's technical talent and hard work in the laboratory will certainly be appreciated in years to come.

Several Professors at Georgia Tech have offered their expertise and experience for which I am very grateful. Many thanks to Professors Phil First, Alex Kuzmich, Brian Kennedy, Chandra Raman, and Li You. I would also like to thank Mark Kimmel, a very talented research scientist, who I have asked for help on many a late night in the lab. Mark was also very helpful in showing us how to set up and operate our Ti:Sapphire laser system.

Finally, I would like to thank my parents and, most of all, my wife Ingrid. My mother and father have both displayed a tremendous interest in my graduate work. They have been very understanding when I was so busy in the laboratory. Ingrid has been a wonderful wife and friend during my graduate career. Her undying love and devotion have strengthened me and given me hope in dark times. Particularly during the last few months, while I finished my thesis, she has been so very understanding and helpful.

TABLE OF CONTENTS

LIST OF FIGURES

SUMMARY

Devices that exploit the properties of quantum mechanics for their operation can offer unique advantages over their classical counterparts. Interference of matter waves can be used to dramatically increase the rotational sensitivity of gyroscopes. Complete control of the quantum evolution of a system could produce a new powerful computational device known as a quantum computer. Research into these technologies offers a deeper understanding of quantum mechanics as well as exciting new insights into many other areas of science. Currently, a limiting factor in many quantum devices using neutral atoms is accurate motional control over the atoms. This thesis describes two recent advancements in neutral atom motional control using both magnetic and electromagnetic confining fields. Part I reports on the demonstration of the first storage ring for neutral atoms. This storage ring may one day provide the basis for the world's most sensitive gyroscope. Part II describes the optical delivery of neutral atoms into the mode of a high-finesse cavity for applications in quantum computing and communication.

CHAPTER I

INTRODUCTION

The world of quantum mechanics remained hidden from us until the beginning of the last century. This was due, in part, to the fact that quantum effects become washed out as the size of a system grows to the point where we can make observations on it. As our measurement techniques have improved, we have been able to discover more and more about the quantum world. We now have the ability to manipulate individual systems on a quantum level, which has led to devices that exploit properties of quantum mechanics in their operation. These quantum technologies promise amazing performance in ultra-sensitive measurements with atom interferometers and the more revolutionary field of quantum computing and quantum information. In this thesis, we present research into these two quantum technologies, both of which rely on the motional manipulation of gaseous neutral atoms. Part I reports on the demonstration of a neutral atom storage ring, a device which could one day provide the world's most sensitive gyroscope. Part II demonstrates delivery of atoms into a *cavity quantum electrodynamics* (QED) system for use in quantum computing.

1.1   *Storage Ring for Neutral Atoms*

The name "storage ring" typically conjures up images of the kilometer-long particle accelerators used in high energy physics. In the second half of the twentieth century, these accelerators enabled us to collide particles at very high kinetic energies, revealing a complex subatomic structure. The circular geometry plays an important role in the design and performance of modern accelerators. Circular accelerators can generate higher kinetic energies than their linear counterparts due to the repeated periodic acceleration in each orbit and can store or recycle high energy particles with minimal losses. Today, the largest particle accelerators, such as Fermilab's Tevatron or CERN's large hadron collider (LHC) project, use a ring geometry to accelerate particles to kinetic energies of 1 TeV and a projected 7

TeV respectively.

There have been proposals to employ a circular geometry to store particles at the opposite end of the energy spectrum as well. In 1989, Thompson *et al.* suggested confining slow spin polarized hydrogen in a storage ring to facilitate creating a Bose-Einstein condensate [1]. Rings using magnetic and electric confining fields to store ultra-cold atoms [2] and polar molecules [3] have also been proposed. Recently, Crompvoets *et al.* realized a prototype storage ring for cold neutral molecules employing electrostatic fields [4]. The proposals are motivated in part by the prospects of increasing the phase-space density in the ring to achieve cold (possibly monochromatic) beam generation or to study controlled collisions. Perhaps the most compelling motivation is the possibility of guided atom interferometry inside the ring.

Atom interferometry began in 1991 when atoms were split on micro-fabricated transmission gratings and then recombined [5, 6]. Shortly thereafter, another atom interferometry technique was developed that used momentum kicks from off-resonant Raman pulses to split and recombine individual atomic wavepackets [7, 8]. Currently, these free-space interferometers offer the world's most sensitive measurement of short term rotations and should soon surpass inertial and gravitational sensors [9]. Guided atom interferometers, which use electric, magnetic, and electromagnetic forces to guide and interfere matter waves, promise even greater measurement sensitivities. The possibility of realizing a guided atom interferometer relies on advances made over the last 15 years in laser cooling and trapping of gaseous atoms to the micro-Kelvin regime. Only at these low temperatures, can the relatively weak electric and magnetic fields available in the laboratory provide the necessary confinement for guiding atoms.

An attractive application of guided atom interferometry is the possibility of creating a matter-wave Sagnac interferometer. Just as light waves interfere, so do quantum matter waves, which are characterized by their de Broglie wavelength of $\lambda_{dB} = h/(mv)$, where h is Plank's constant, m is the mass of the particle, and v is its velocity. In a Sagnac interferometer, these waves propagate in both directions around a closed topology, such as a ring. The rotation in the plane containing the ring will cause an effective length difference

in the two paths, which produces a relative phase shift. Optical versions of these devices are in widespread use today in navigation and provide the backbone of the inertial guidance systems used in commercial and military aircraft. Atom based devices offer $> 10^{11}$ times greater phase sensitivity than comparable optical devices, deriving from the fact that the Sagnac rotational phase is proportional to the relativistic energy of the particle, which is much larger for massive particles (mc^2) than for photons ($\hbar\omega$). This enhancement in sensitivity is what motivates much of the current research in guided atom interferometry. The demonstration of a storage ring is an important first step in the realization of many guided atom applications, including a Sagnac interferometer. Part I of this thesis describes the first storage ring for neutral atoms.

1.2 Quantum Computing

We now find ourselves in the information age, where the industrial machines of yesterday are being enhanced and sometimes replaced by smaller, smarter devices. Computers and information processing have changed the way we live, the way we work, and the way we learn. The pace of development is rapid, following the well-known empirical phenomenon "Moore's Law" [10], whereby the power of computers, characterized by the number of integrated units on a semi-conductor chip, roughly doubles every 18 months. This predicts an exponential increase in the density of components on a single chip so that in a few years, each component will consist of only a few atoms. Clearly quantum effects will prevent these "classical" logic machines from operating effectively when made so small. However, where quantum mechanics closes one door, it opens another; in this case in the form of quantum information processing and quantum computing.

Quantum computers rely on coherent information encoding and an intrinsic massive parallelism provided by coherent evolution of purely quantum systems. The roots of this field are in important work by Feynman [11] and Deutsch [12] as well as others, but the landmark event occurred in 1994, when Shor presented his quantum algorithm [13] for taking discrete logarithms, a corollary of which provides for an exponential increase in speed of number factorization. Since most of today's encryption relies on the presumed mathematical

difficulty of factoring large numbers, the successful demonstration of a quantum computer would have a huge impact on data encryption and national security.

Another quantum algorithm, developed by Grover [14], allows for searching in an unordered database in a time of only $O(\sqrt{N})$ instead of $O(N)$, where N is the size of the data set. This can be used to speed up the processing of many tasks that require a large amount of conventional computing resources, such as the traveling salesman problem and the telephone book lookup problem. This technique can also be used to break other, non-factorization based, encryption much more efficiently than classical computation.

The operation of a quantum computer relies on the successful realization of several important criteria. We need a well-characterized two level quantum system, or "qubit", to store quantum information. Controlled interactions should manipulate the individual states of these qubits as well as the quantum states of multiple qubit arrays, while unintentional interactions, such as coupling to the environment must be avoided. The latter interactions are collectively known as "decoherence" and present a fundamental difficulty in performing quantum computations. A quantum computer should be initializable, in the sense that we can prepare the input state of all qubits before a calculation is performed. The system must be scalable so as to accommodate a dynamic number of qubits depending on the application. Finally, a quantum computer must be able to read out its states with quantum measurements.

In addition to Shor's algorithm, perhaps an equally important development in 1994 was a paper by I. Cirac and P. Zoller [15] that proposed an experimentally viable implementation of a quantum computer with trapped ions. Experimentally, quantum computers are still in their infancy, but there are groups pursuing its advancement in many areas of physics, including neutral atoms, trapped ions, quantum dots, super-conducting quantum interference devices, and bulk nuclear magnetic resonance [16]. We are particularly interested in the approaches based on neutral atom-cavity quantum electrodynamics (QED). The hyperfine ground states of neutral atoms provide excellent candidates for qubits because they are long lived and interact weekly with the environment. The cavity can couple the quantum

states of neutral atoms to single photons, which offer excellent transport of coherent quantum information. A key step in this quantum computing scheme relies on the successful positioning of neutral atoms inside the mode of a high-finesse optical cavity.

Part II of this thesis reports on successful deterministic delivery of neutral atoms into a cavity QED system using optical trapping fields. We present results from measurements in the cavity, as well as a detailed study of the atomic positioning laser system. This achievement lays the groundwork for a scalable quantum information processing system based on neutral atoms and cavities.

1.3   Organization of This Thesis

The thesis is roughly divided into two parts. The first part describes results from the first demonstration of a neutral atom storage ring. The second part describes a neutral atom cavity QED experiment, which focuses on preparing neutral atoms for applications in quantum computing and manipulating the position of neutral atoms while inside a high-finesse optical cavity. A common theme in all of this work is controlling and manipulating the positional degrees of freedom of ultracold neutral atoms.

In Ch. 2, I describe the theoretical framework behind the storage ring. Atom interferometry and its applications in guided optics are first discussed. Mechanisms for guided atom optics are presented in the next section on magnetic guiding and trapping. I then describe laser cooling, which is common to both experiments in this thesis. The section concludes with a description of the concept of the storage ring.

Ch. 3 begins with a description of the storage ring construction, the vacuum chamber, and the imaging system. This is followed by experimental results from the first generation Ring. In the next section I describe the second generation ring and its experimental results. Then I summarize the storage ring experiment, and consider future applications and improvements to the system.

Ch. 4 introduces the concepts of the cavity QED system. This begins with an introduction motivating research in neutral atom quantum computing. Next I give an overview of our approach, stating the challenges we face, and describe other work in the field. Finally, I

describe the relevant theoretical background for the atom-cavity QED experiments, dipole force traps, and atomic positioning.

Ch. 5 reports on the cavity QED experiment. First, the experimental apparatus is described. This includes the design and construction of the cavity. Next I present data from atoms optically guided through the cavity field. Finally, deterministic delivery of a group and single atoms into the cavity mode is demonstrated.

An in-depth discussion of the optical positioning system is given in Ch. 6. I begin by giving a detailed description of the known loss mechanisms for optical dipole traps. Then, each laser system is described and data is presented to characterize the system's performance. I conclude the chapter and the thesis with a summary of the cavity QED experiment and offer future recommendations.

CHAPTER II

THEORETICAL BACKGROUND FOR THE STORAGE RING

In this chapter, we will discuss the theoretical framework and operation of the storage ring. Three aspects of atomic physics that play a key role in the development of the storage ring are presented. First, we give an overview of atom interferometry in section 2.1. Then we present properties of magnetic guiding in section 2.2. Next, a section on laser cooling (2.3) prepares us for applications in the ring experiment, as well as the cavity QED experiment. Finally, we describe the concept of the ring in section 2.4.

2.1 Atom Interferometry

Optical interferometers are well known for their ultra-high sensitivity and are used for precision measurements in many areas of research. This sensitivity allowed Michelson and Morley in 1887 to demonstrate the lack of "ether" as a propagation medium for electromagnetic waves with a light interferometer [17]. In 1924, de Broglie proposed that matter should exhibit wave-like behavior as well. Shortly thereafter, interference of matter was observed in electrons [18], and neutrons [19]. The field of atom interferometry began in 1991 when atoms were split on micro-fabricated transmission gratings and then recombined [5, 6]. Only months later, another atom interferometry technique was developed that used momentum kicks from off-resonant Raman pulses to split and recombine individual atomic wavepackets [7, 8]. Currently, these free-space interferometers offer the world's most sensitive measurement of short term rotations and should soon surpass inertial and gravitational sensors [9].

Perhaps the best demonstration of the advantage in using atom interferometry over light is given by the Sagnac effect as shown in Fig. 1. A Sagnac interferometer allows light or matter waves to propagate in both directions around a closed loop. The rotation in the
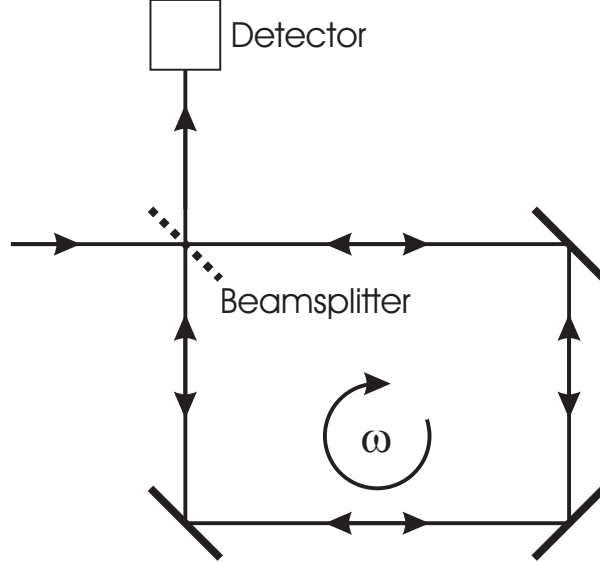
Figure 1: An optical Sagnac interferometer. Light propagates in both directions around a closed loop.

plane containing the loop will cause an effective length difference in the two paths, which produces a phase shift given by [20]:

$$\Delta\Phi = \mathbf{A} \cdot \boldsymbol{\omega} \frac{E}{\hbar c^2} \tag{1}$$

Where A is the vector area element enclosed by the loop, $\boldsymbol{\omega}$ is the rotation vector, and E is the relativistic energy, which is 10^{11} times greater for an atom (mc^2) than a optical photon $(\hbar\omega)$! While all 11 orders of magnitude probably cannot be experimentally realized because of differences in particle flux and enclosed area, it is this tremendous sensitivity enhancement that motivates much of the research in atom interferometry today. The Sagnac phase shift has been measured in free space interferometers using Raman pulses [8, 9] and atomic gratings [21] and has been used to demonstrate a short-term rotation-rate sensitivity of $6 \cdot 10^{-10}$ rad/s [22].

Guided atom interferometers, which use magnetic fields to confine the trajectories of neutral atoms have also been proposed [23, 24, 25, 26]. These offer several advantages over free-space interferometers. A limiting factor in the sensitivity of free-space interferometers
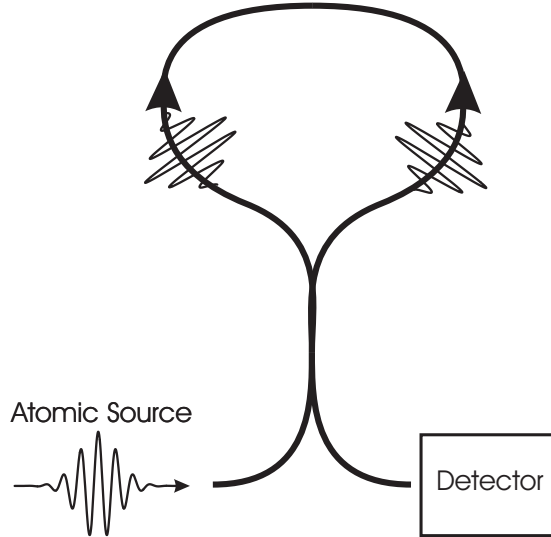
Figure 2: A guided atom interferometer with a Sagnac geometry. Since both atomic amplitudes travel the same path, much of the common-mode noise is rejected.

is their small enclosed area. The relatively small momentum kick imparted by the Raman pulse makes the splitting angle between quantum motional states of the atom very shallow. In order to enclose the largest area possible, these interferometers are several meters long and are limited by gravitational sag in the beam. Guided atom interferometers, on the other hand, can have wide splitting angles and can be made to enclose a greater area over much shorter distances. Furthermore, guided interferometers readily lend themselves to the Sagnac geometry (see Fig. 2), which allows both components of the matter wave to propagate along the same path in opposite directions. This eliminates many common-mode phase shifts caused by differences in the potentials along each path. The free-space interferometers typically are of the Mach-Zender type, which has separate arms for each path and is thus sensitive to these phase shifts.

The atom analog of single mode propagation of a laser beam in an optical fiber is atomic propagation along a single transverse energy level in the guide. One way to accomplish this would be to inject a Bose-Einstein condensate (BEC) into the guide and prevent excitation to higher transverse energy states. However, recent theoretical proposals have shown that it is also possible to build interferometers that operate in a multi-mode fashion with thermal

atoms, by adjusting experimental parameters so that constructive interference from each guided mode overlaps at the detection point [26].

Atom interferometers do indeed offer tremendous potential, both as exquisitely sensitive measurement devices, and as an experimental basis for investigating properties of the guided atoms themselves. In order to see how such an interferometer could be realized however, we must first understand how neutral atoms can be confined and manipulated by magnetic fields. This is the subject of the next section.

2.2   *Magnetic Guiding*

Confinement of neutral atoms requires interaction with a spatially dependent force (we refer to a *trap* when atoms are confined in three dimensions and a *guide* when they are confined in only two). Neutral atoms are not susceptible to the the strong Coulomb force used to trap ions and charged molecules because they do not posses a net charge. Instead, we must use other weaker forces for positioning, such as the interaction between the atom's magnetic dipole and externally applied magnetic fields. This section explores the history and theoretical background of magnetic trapping and guiding and studies those field geometries used for experiments.

The first observation of magnetic trapping in neutral atoms was made by Migdall *et al* [27] in 1985 with laser-cooled sodium, although magnetic confinement of neutrons had already been demonstrated previously that year [28]. Shortly thereafter, the number and density of trapped atoms rapidly increased [29], and these traps were extended to include cryogenically cooled atomic hydrogen [30, 31]. In 1995, magnetic traps were used to create an atomic Bose-Einstein Condensate (BEC) [32, 33] which, with the exception of an all-optical technique [34], remains the only method for making BECs.

Two dimensional magnetic guides have also been developed. The first of these guides was demonstrated by Schmiedmayer in 1995 by guiding atoms from an atomic beam along a 1 m long section of wire [35]. Ultra-cold atoms were first guided by Denschlag *et al.* in 1999 along a single current carrying wire [36]. The atoms orbited in a Kepler like potential around the wire or were confined beside the wire when an external bias field was applied.

Two-wire guides with an external bias field have also been demonstrated [37, 38]. In these guides, the wires are etched onto the surface of a glass substrate or semiconductor chip. An external bias field moves the potential minimum above the surface. Four wire magnetic guides have been loaded directly by producing an atomic trap on the guide axis [39, 40]. The versatility of these guides have allowed demonstration of atomic beamsplitters [41, 42] and atom conveyors [43].

Both magnetic traps and guides rely on the interaction of the atom's magnetic dipole $\boldsymbol{\mu_m}$ with a non-uniform magnetic field $\mathbf{B}(\mathbf{r})$, for which the interaction energy is:

$$E = -\boldsymbol{\mu_m} \cdot \mathbf{B}(\mathbf{r}) = -\mu_f |\mathbf{B}(\mathbf{r})| \tag{2}$$

Where μ_f is the projection of the magnetic dipole $\boldsymbol{\mu_m}$ onto the field direction. This projection remains constant as the magnetic dipole precesses about the field vector if the magnetic field and thus the precession frequency is large enough. Quantum mechanically, this energy is given by:

$$E = \mu_b \, g \, m_f \, |\mathbf{B}| \tag{3}$$

Where μ_b is the Bohr magneton, g is the Lande g-factor, m_f is the z component of the angular momentum F, and B is the magnitude of the magnetic field. The precession of the magnetic dipole corresponds to a constant value of m_f. The force on the dipole is given by the negative gradient of this potential:

$$\mathbf{F} = -\mu_b \, g \, m_f \, \nabla |\mathbf{B}(\mathbf{r})| \tag{4}$$

Although Maxwell's equations forbid the creation of a maximum in the magnitude of the magnetic field for current free regions of space, it is possible to create a field minimum, which allows the trapping of weak-field seeking states, or those states with $gm_f > 0$ (classically this corresponds to dipoles that are anti-aligned with the magnetic field). These traps are divided into two groups based on the magnitude of the magnetic field at the location of
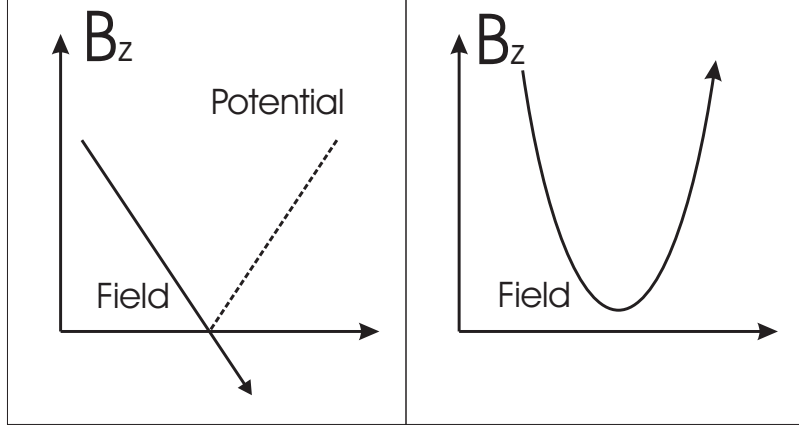
Figure 3: A plot of the two types of magnetic traps and guides. On the left, the field goes to zero at the minimum of the trap, on the right it does not. The minimum on the left is associated with a change in sign of the magnetic field. For clarity, we show only the z-component of the magnetic field.

the trap minimum B_0: Traps with $B_0 = 0$ can be constructed from very simple current geometries, such as a pair of anti-Helmholtz coils or two parallel wires. The minimum comes from a reversal in the direction of the magnetic field, causing a non-differentiable potential as seen in Fig. 3. In the vicinity of this point, where the field magnitude is very small, the precession frequency ω_l becomes slower than the rate of change of the direction of the magnetic field Φ:

$$\omega_l = \frac{|\boldsymbol{\mu_m}|\,|\mathbf{B}|}{\hbar} < \frac{d\Phi}{dt} \tag{5}$$

In this case, the dipole can no longer follow the field adiabatically and a spin flip or "Majorana flop" can occur [44]. Non-adiabatic spin flips are suppressed in the second type of trap where $B_0 > 0$. However, these traps confine much less tightly because of their smooth potential near the minimum.

It is possible to create guiding potentials for neutral atoms using current carrying wires or combinations of wires and externally applied magnetic fields. Fig. 4 shows four typical guide potentials and their corresponding trap depths. The top left guide, used for the neutral atom storage ring, consists of two parallel wires separated a distance d, carrying current I in the same direction. The magnetic field from this configuration is given by

summing field contributions of each wire:

$$\mathbf{B}(x,y) = \frac{\mu_0 I}{2\pi} \begin{pmatrix} -\frac{y}{\left(x-\frac{d}{2}\right)^2+y^2} - \frac{y}{\left(x+\frac{d}{2}\right)^2+y^2} \\ \frac{x-\frac{d}{2}}{\left(x-\frac{d}{2}\right)^2+y^2} + \frac{x+\frac{d}{2}}{\left(x+\frac{d}{2}\right)^2+y^2} \\ 0 \end{pmatrix} \tag{6}$$

Taking the magnitude of this field and multiplying with $\mu_b\, g\, m_f$ gives the guiding potential. Near the trap center, where $x/d, y/d << 1$ we can approximate this potential by:

$$\mathbf{B}(x,y) \approx \frac{4\mu_0 I}{\pi d^2} \begin{pmatrix} -y \\ x \\ 0 \end{pmatrix} \tag{7}$$

We see that the field goes to zero at the origin where the potential is cone shaped. The trap depth of this guide can be easily calculated by finding the maximum in the potential along the y-axis:

$$U_{max} = \mu_b\, g\, m_f \frac{\mu_0 I}{\pi d} \tag{8}$$

The characteristics of other guides can be obtained in the same fashion.

The scaling for these types of traps is particularly simple. For a system of characteristic size d, the field magnitude, which is proportional to the trap depth, typically scales as $1/d$, as we observe from the example given above. The field gradient, proportional to $\mathbf{F}$, typically scales as $1/d^2$, and the field curvature typically scales as $1/d^3$. We immediately see that these scaling laws favor smaller geometries and recent work in magnetic microtraps [45, 43], including the production of a BEC on a microtrap [46], has reinforced this concept. An excellent introduction to microtrap theory, design, and production is given in [47].

2.3   Laser Cooling

Much of the success of neutral atom traps has relied on the tremendous advances in the field of laser cooling made over the last 15 years. The reason for this is that trapping

Two Wires no Bias
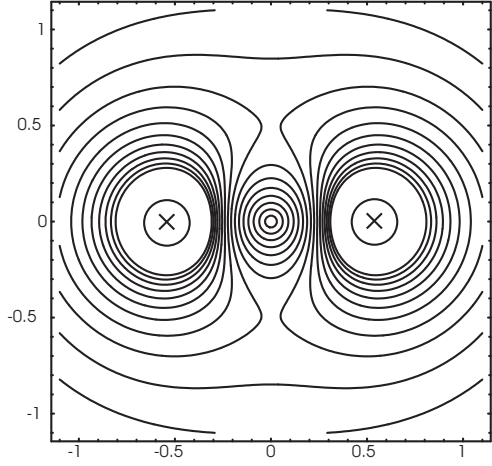
Four Wires no Bias

$$\Delta E_0 := \frac{\mu_m \mu_0}{d\pi} I$$
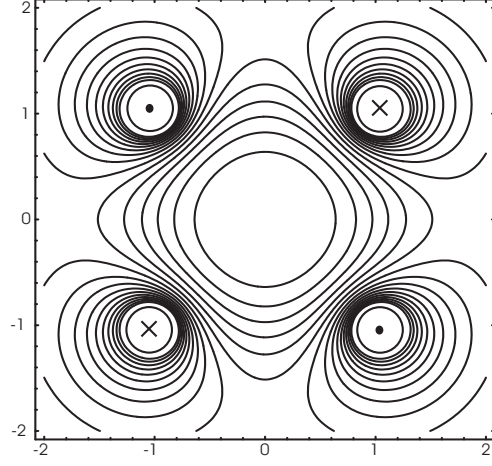
$$\Delta E = 3^{3/4} \Delta E_0$$

One Wire with Bias
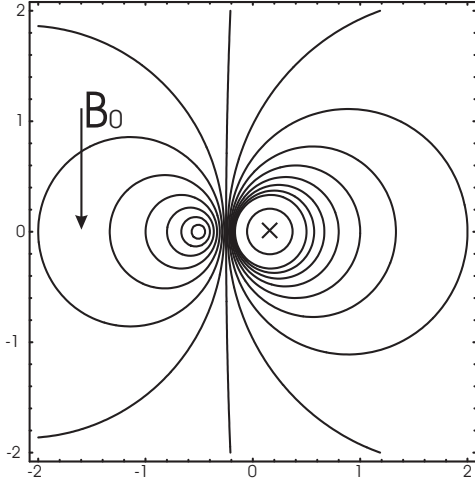
B_0

Two Wires with Bias

B_0

$$\Delta E = \Delta E_0$$
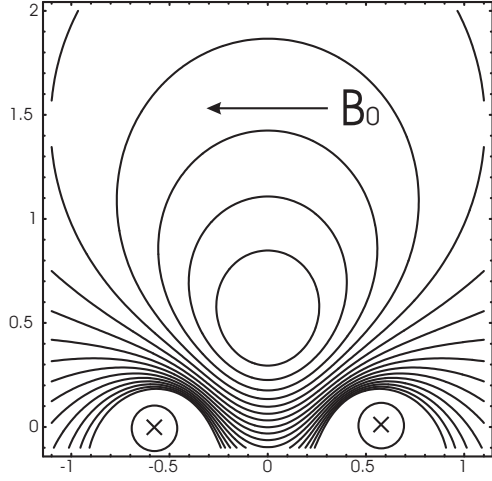
$$\Delta E = \Delta E_0$$

Figure 4: The magnetic field magnitude (which is proportional to the trapping potential) is shown for four different types of guides. Both guides on top are self contained, without externally applied bias fields. The bottom guides have an externally applied bias field, which allows them to be used as surface guides. The trap depth of each guide is given relative to the two wire guide, where each has the same characteristic spacing a, which is the distance from the guide center to a wire. Circles indicate the positions of wires, while and "X" or a "o" indicated direction of the current.

14

energies for neutral atoms are small compared to their average kinetic energy at room temperature. Typical laboratory conditions can only produce trap depths on the order of 1 mK and some, like the optical dipole traps presented later in this thesis, only have a trap depth of a few μK. It is the powerful mechanism of laser cooling that enables us to trap, guide, and manipulate neutral atoms. In this section, we will discuss the history, theoretical background and practical applications of laser cooling.

2.3.1 MOT

Perhaps the most important tool in laser cooling is the magneto-optical trap (MOT). The combination of simple construction and robust operation make the MOT a workhorse for almost all experiments involving laser cooling and trapping. Since its first demonstration with sodium atoms in 1987 [29], the MOT has trapped and cooled all of the stable isotopes of alkali atoms and some noble gases as well. Atoms in a MOT are cooled to < 1 mK, six orders of magnitude below the room temperature vapor used for loading. Below, we will introduce the MOT's theory of operation and limits on temperature, density, and atom number attainable in a MOT.

We begin with an atom having a simple transition scheme $J_g = 0 \rightarrow J_e = 1$, with three Zeeman components ($m = -1, 0, 1$) in the excited state. If we illuminate this atom with two counterpropagating laser beams of opposite circular polarization tuned slightly below the atom's resonant transition, we will produce a viscous damping force on the atom, known as optical molasses [48, 49]. This cooling force arises from the fact that the atom will preferentially scatter photons from the beam it is moving towards. Its motion doppler shifts the frequency of this beam closer to resonance so that the scattering rate is increased.

If we add an inhomogeneous magnetic field, such as that from a spherical quadrupole configuration, the resonance frequencies of each of the three Zeeman sublevels will tune with the atom's position in the field. A schematic in Fig. 5 shows how each of these energy levels are shifted. If we assume, without loss of generality, that the atom is on the right side of the field zero, the magnetic field will shift the σ_- beam closer to resonance than the σ_+ beam. This causes the atom to scatter more photons from the right, forcing it back to
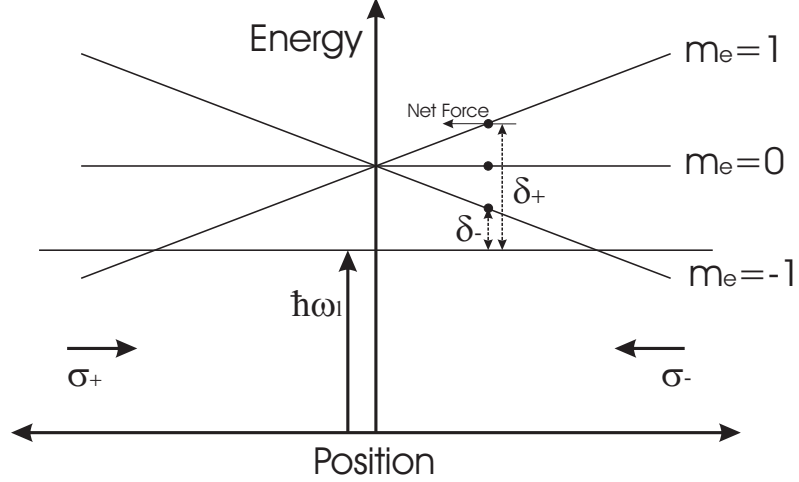
Figure 5: Magnetic level shifts and corresponding detuning for an atom in the MOT. The position of the atom is designated with a filled circle. Because the atom lies to the right of the field zero, the energy of the $m = -1$ level is shifted closer to resonance than the $m = 1$ level. This causes the atom to scatter more light from the σ_- polarized beam and be forced back to the left.

the center of the trap. The inhomogeneous magnetic field provides the spatially varying potential necessary to confine the cooled atoms.

The total force on the atoms is given by the rate at which momentum is transferred to the atom from each beam. For weak fields, this is simply the product of the momentum carried by each photon ($\hbar k$) and the scattering rate [50]:

$$\Gamma_\pm = \frac{\gamma}{2} \frac{s_0}{1 + s_0 + (2\delta_\pm/\gamma)^2} \tag{9}$$

Here γ is the linewidth of the atomic transition, $\delta_\pm$ is the difference in frequency between the laser and $m = 1$ and $m = -1$ transitions, and s_0 is the saturation parameter defined as the ratio of the laser's intensity at the location of the atom to the atom's saturation intensity I/I_{sat}. The detuning is given by the contributions from the velocity dependent doppler shift, used to cool the atoms, and the spatially dependent Zeeman shift, which traps the atoms:

$$\delta_\pm = \delta \mp \mathbf{k} \cdot \mathbf{v} \pm \beta z \tag{10}$$

16

Where δ is the detuning of the laser beam to the unperturbed atomic resonance, and $\beta z = \mu_m B' z / \hbar$ is the energy shift from the interaction of the atom's dipole and the magnetic field as seen in section 2.2. For $\delta_\pm \sim \delta$, equations 9 and 10 lead to an approximate force on the atom of:

$$F(v, z) \approx (\hbar k)(\mathbf{k} \cdot \mathbf{v} + \beta z) \frac{4 s_0 (2\delta/\gamma)}{1 + s_0 + (2\delta/\gamma)^2} = -av - bz \tag{11}$$

Where a and b are defined as the damping and spring constants respectively. For negative detunings ($\delta < 0$), this leads to the motion of a damped harmonic oscillator.

Experimentally, this scheme can be implemented in three dimensions by intersecting laser beams of the correct polarization from three linearly independent directions. This polarization is determined by the orientation of the magnetic coils. In the case of a spherical quadrupole field from two anti-Helmholtz coils, the circular polarizations of those beams on the axis of the coil should be opposite the other two. For those experiments presented in this thesis, we use ^{87}Rb, whose level structure is shown in Fig. 6. Here we can see the three typical energy scales associated with all alkalis. The fine splitting, Δ_f, is much larger than the ground state hyperfine splitting, Δ_{hf}, which in turn is much larger than the excited state hyperfine splitting, Δ'_{hf}.

In our system, light tuned $\sim$15 MHz below the $5S_{1/2} - 5P_{3/2}$ $F = 2$ to $F' = 3$ transition provides cooling while anti-Helmholtz coils generate a magnetic field gradient of 6 G/cm. Atoms excited to the $F' = 3$ can only decay to the $F = 2$ state because of selection rules. However, the small excited state hyperfine splitting gives rise to an off-resonant excitation of the $F' = 2$ state, which can decay to the $F = 1$ ground state. The large ground state hyperfine splitting prevents these atoms from being excited by the cooling light once they fall into the lower ground state. Therefore, an additional "repump" beam resonant with the $F = 1$ to $F' = 2$ excites these atoms to the excited state, so that they may decay back into the cooling cycle.

The random nature of photon scattering in a MOT leads to heating through momentum diffusion. In a steady state condition, this heating rate balances the cooling provided by
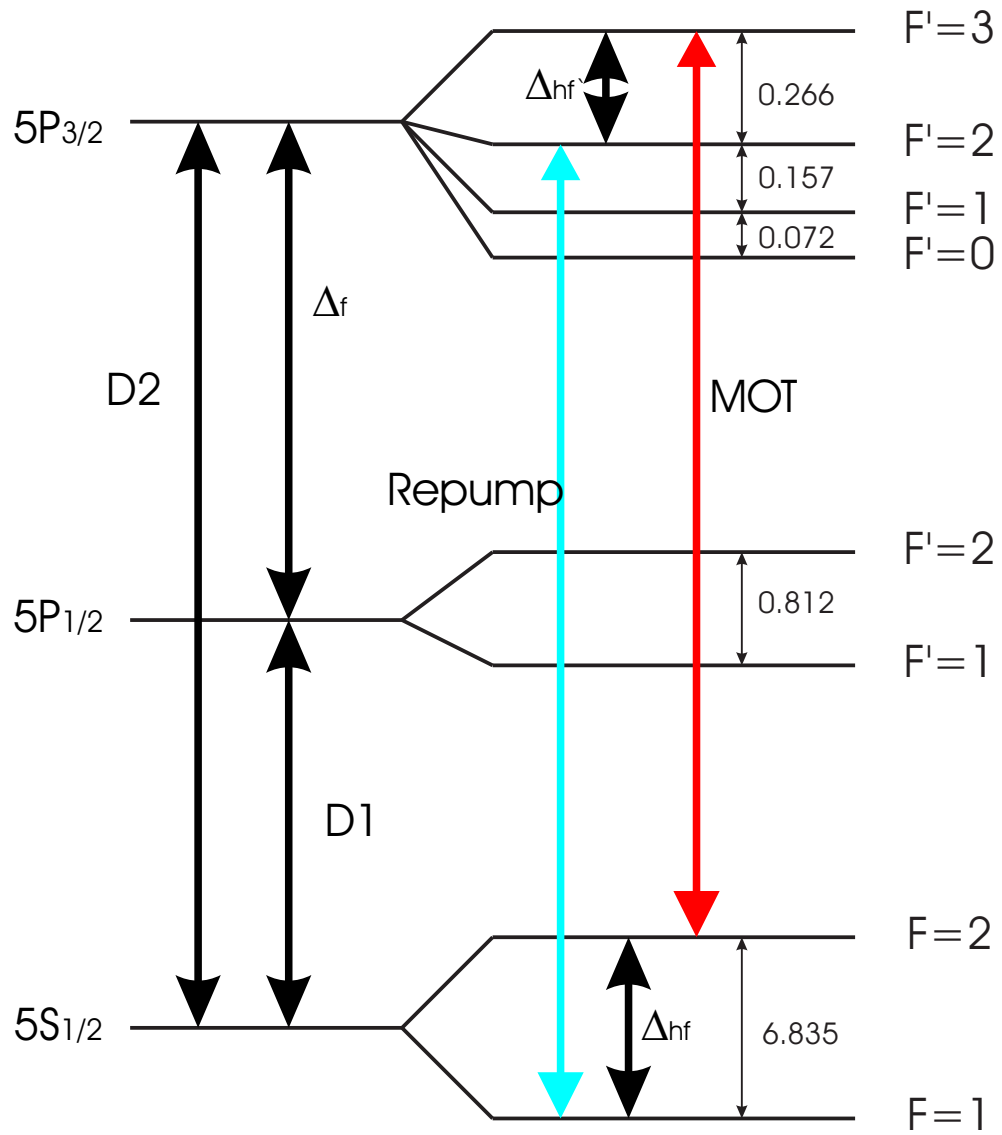
Figure 6: Level structure for ^{87}Rb as it is relevant for this thesis. The transitions coupled by the cooling (MOT) and repump light are shown. All frequencies are given in GHz.

the viscous force so that there is a finite temperature at which the atoms settle. This limit arises from the fact that as an atom slows down, the change in the laser frequency seen by the atom due to the doppler shift becomes comparable to its transition linewidth. At this point, the atoms directional preference to absorb photons diminishes and the cooling process stops. This is known as the doppler limit is $T_d \sim \hbar\gamma/(2k_b)$ [51] and corresponds to 141 μK for ^{87}Rb.

The number of atoms trapped in the MOT depends largely on the atomic source. For a vapor cell, the scaling laws with the size, intensity, and detuning of the beams have been derived in [52] and [53]. Generally, the larger the intensity and size of the beams, the more atoms will be trapped. However, experimental constraints usually limit both these factors. Given a constant power, it is generally better to make large beams, as the number scales with the fourth power of the diameter of the beam [52].

Wieman *et al* have shown that the density in a MOT is limited by reabsorption of scattered radiation [54] and state changing collisions [55] to $\sim 10^{11}/cm^3$. Reduction in the repump intensity in the final stages of trapping can be used to increase this density [56, 57]. This will be described in more detail when discussing the loading of optical dipole traps in chapter 4.

2.3.2 Sub-Doppler Cooling

Soon after the first demonstration of the MOT, it was experimentally shown that atoms could be cooled to well below the doppler limit [58]. This limit was based on the model of a two level atom, which is insufficient to explain the observed sub-doppler cooling. Real atoms have a more complex level structure, which, in the presence of polarization gradients, can be exploited to cool much more efficiently than with doppler based techniques. Here, we discuss one polarization configuration, known as σ_+-σ_- (read: sigma plus, sigma minus), that is used to cool atoms below the doppler limit in the experiments presented in this thesis.

As the name suggests, σ_+-σ_- cooling is done with two counterpropagating beams of opposite circular polarization (just as those used in the MOT). The resulting electric field

vector for this configuration is:

$$E = \sqrt{2}E_0 e^{-i\omega t} \begin{pmatrix} cos(kz) \\ -sin(kz) \end{pmatrix} + c.c. \tag{12}$$

We see that this field is everywhere linearly polarized, but the polarization vector rotates along the z-axis. The σ_+-σ_- cooling derives from the fact that as the atom moves along this axis, the rapidly rotating polarization vector selectively populates the ground state magnetic sublevels. The shift in population causes the atom to preferentially absorb light from the direction in which it is travelling, therefore slowing its motion. Although this mechanism seems similar to Doppler cooling, it is entirely different. Here, the preferential absorption derives from the motion in the polarization gradient, which is much more sensitive to velocity than that caused by the doppler shift. It has been shown that this cooling leads to a final temperature of $\sim 10T_r$ or a few μK, where T_r is the recoil energy. Since the atom must posses multiple ground state sublevels, σ_+-σ_- cooling is only possible with atoms having $J_g = 1$ or higher.

Sub-doppler cooling is a key step in transferring atoms from the MOT to the ring. It is easily implemented in a MOT, where the σ_+-σ_- configuration is already in place. We perform sub-doppler cooling after the MOT is loaded by simultaneously lowering the detuning and intensity of the cooling beams, and reducing the magnetic field gradient.

2.4   Storage Ring Concept

The basic concept of our storage ring design is simple. Two concentric loops of wire carry current in the same direction. This corresponds to the linear potential of a two-wire guide wrapped into a circular geometry (the trapping potential for a two-wire guide was given previously in 2.2). Atoms are coupled into this guide via a second two-wire guide that straddles a MOT above the ring (see Fig. 7). Sub-doppler cooling allows the modest potentials created by current in these wires to confine and guide the atoms. There are two rings described in this thesis. The first generation ring uses a steady state transfer mechanism, and the second generation ring uses a pulsed transfer mechanism. The details
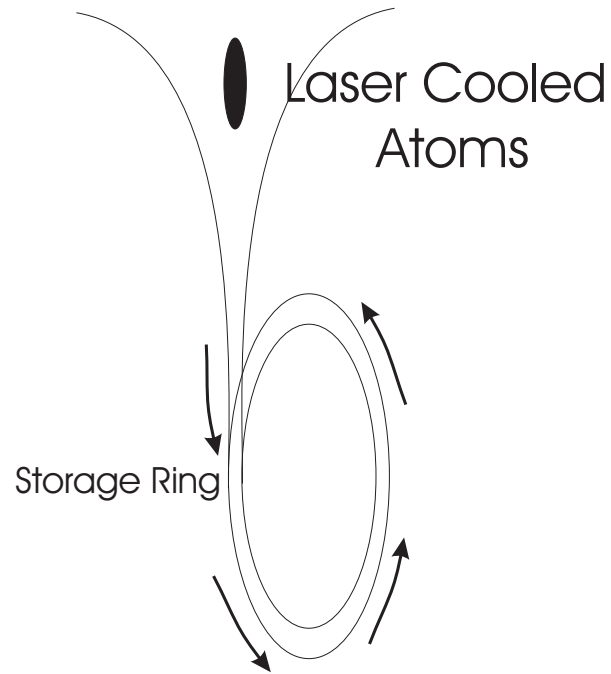
Figure 7: The basic concept of our storage ring design.

of their design and construction are given in the next chapter.

CHAPTER III

STORAGE RING EXPERIMENT

This chapter is based on the experiment described in:

J.A. Sauer, M.D. Barrett, M.S. Chapman. "Storage Ring for Neutral Atoms." *Physical Review Letters*, **87**(27):270401,2001

3.1   Introduction

The storage ring requires several experimental systems for its implementation. We must produce a laser system capable of addressing the transitions in ^{87}Rb for making a MOT. The ring itself needs to be designed and constructed. We have to devise a detection system for monitoring and extracting data from the atoms while orbiting in the ring. Finally, we have to operate the ring inside a vacuum chamber to prevent background gas from interfering with the cooling and guiding of the atoms.

The details of the experimental apparatuses and results of the neutral-atom storage ring are presented in this chapter. Section 3.2 describes the technical details of the experiment, including the MOT laser system, the design and construction of the ring, the vacuum chamber, and imaging techniques. In section 3.3 we show data collected from the first generation ring, and the limitations of this design. Finally, section 3.4 describes the second generation ring and its success.

3.2   Technical Details of Ring Experiment

3.2.1   MOT Laser System

Rubidium is an experimentally attractive atom for laser cooling experiments because its strong optical transitions are easily accessible by inexpensive semiconductor diode lasers. Their combination of small size, robust operation, low cost, and high power output makes them ideal for use in any laboratory where Rb is trapped and cooled. In this section we

describe the diode laser system used to produce our MOT. There are three diode lasers in the MOT system: an extended cavity stabilized "master" laser, an injection locked "slave" laser, and a free-running "repump" laser. This system is a simplification of the setup described in [59] and based on the design in [60, 61].

There are several laser requirements necessary to successfully produce a MOT. The frequency of the laser has to be stabilized to the correct atomic transition. Furthermore, the linewidth of the laser must be much narrower than the excited state hyperfine splitting so that only preferred transitions are excited. The laser must also be able to produce enough power so that the intensity is three to five times larger than the saturation intensity of the atom.

Below we describe a system which meets the above requirements. In section 3.2.1.1, we detail the frequency and temperature stabilization of the diode lasers. This is followed by a description of the master-slave injection locking and frequency tunability in section 3.2.1.2. Finally, section 3.2.1.3 describes the free-running repump laser. This laser system is used both in the storage ring experiment and the cavity QED experiment.

3.2.1.1 Stabilization

A diode lasers' output frequency is very sensitive to changes in operating current and temperature. For stable operation, these parameters must be held constant to within ~ 1 mK and ~ 1 μA respectively. Our laser diodes (now Sharp GH0781JA2C) are temperature stabilized to ~ 1mK with a single stage thermo-electric cooler (TEC) and temperature control circuit described in [62]. A plexiglass housing encloses the laser to provide passive temperature stability against air currents. Two of the lasers are free-running, meaning that they do not have an external feedback cavity, and must therefore be cooled to a temperature which is below the dew point in the laboratory to achieve the desired wavelength. To prevent condensation, a desiccant is placed in the plexiglass housings of these lasers. An in-house current controller, based on the design in [63], provides current for these lasers [1]. The modulation input on this controller allows frequency control of the laser at a rate of ~ 300

23

kHz and the RF input allows application of sidebands at < 10MHz.

A diffraction grating with 1800 lines/mm forms an extended cavity for the master diode laser [60, 61]. The angle of this grating is coarsely set with a mirror mount and the z-position of the laser's collimation lens is adjusted to minimize the threshold current in this extended cavity configuration. Fine adjustment of the length of the extended cavity is accomplished with a piezo-electric transducer (PZT) (Thorlabs model AE0203D04) that is driven by a high voltage controller (Thorlabs model MDT691 Piezo Driver).

Long term stability of the master laser is achieved by actively locking the frequency to the saturated absorption (SA) spectrum [60, 64] of ^{87}Rb using two different frequency modulation (FM) [65, p.1031] techniques. The first technique, desribed in detail in [59], applies an RF sideband to the master laser directly and was used for the majority of the experiments in this thesis. Here we describe only the details of the second technique, implemented just recently. As shown in Fig. 11, 1 mW of light from the master laser is split into a pump and probe beam. The pump beam is passed through a tuneable acousto-optic modulator (AOM), which shifts and modulates the frequency of the light by:

$$\Delta\omega = \omega_{rf} + \omega_s \sin\left(\omega_m t\right) \tag{13}$$

Here, ω_{rf} is the center frequency of the AOM (110 MHz), ω_s is the amplitude of modulation (8 MHz produces the largest locking signal), and ω_m is the frequency of modulation. We select ω_m to be ~ 500 kHz, so that the slope of the locking signal is maximized. The unmodulated probe beam then counter-propagates with the pump through a Rb vapor cell and is detected by a Thorlabs PDA55 optical detector. The signal from the PDA55 is demodulated in a mixer at ω_m, and filtered at 30 kHz with a low pass 6 dB/Oct filter. The peaks will appear at 110/2 MHz above the probe frequency because only the pump is shifted by the AOM (see Fig. 9). The FM signal obtained in this fashion is larger and offers a more robust lock than the first method because the probe laser does not have residual

---

[1]We have made two modifications to this design to allow for more stable operation and higher current output. A 47Ω resistor is placed in parallel with the 100μH inductor just below the VP0106 to prevent oscillations at high output current, while a second 50Ω Vishay resistor added in parallel to the first increases the maximum current available from the device to 300 mA.
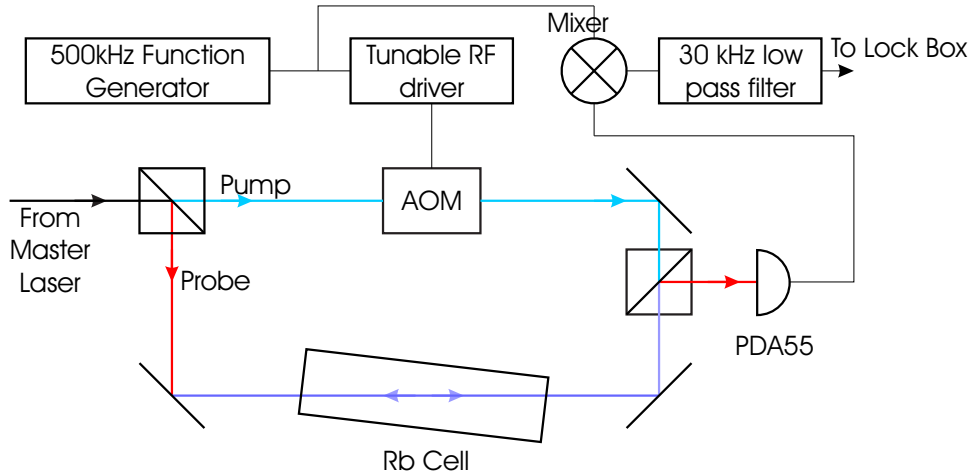
Figure 8: A simplified schematic of the second saturated absorption FM technique. The blue represents the pump beam, while the red is the probe. Note the tilt of the Rb cell, which prevents internal reflections from interfering with the absorption spectrum.

amplitude modulation that changes the shape of the signal. Furthermore, the modulation is not applied to the master laser, eliminating the RF sidebands generated by the first technique.

Both saturated absorption techniques produce an error signal that is proportional to the frequency difference between the laser and the desired lock point for small frequency excursions. We feedback on this error signal using a proportional-integral (PI) controller. The P component is fed into the master's current modulation input, while the I component is fed to the PZT driver. The low bandwidth, but great dynamic range, of the PZT control responds best to the integrated signal, while the higher bandwidth, but smaller tuning range, of the current modulation is more appropriate for the proportional signal. Together, these two feedback signals can lock the master laser to any transition in the SA spectrum for > 12 hours.

3.2.1.2   Injection Locking

To achieve frequency tunability and higher power output, light from the master laser is double-passed through a tuneable AOM and used to injection lock ([64, p.1129-1170]) a free running "slave" diode laser. The free-running slave can output higher power than the
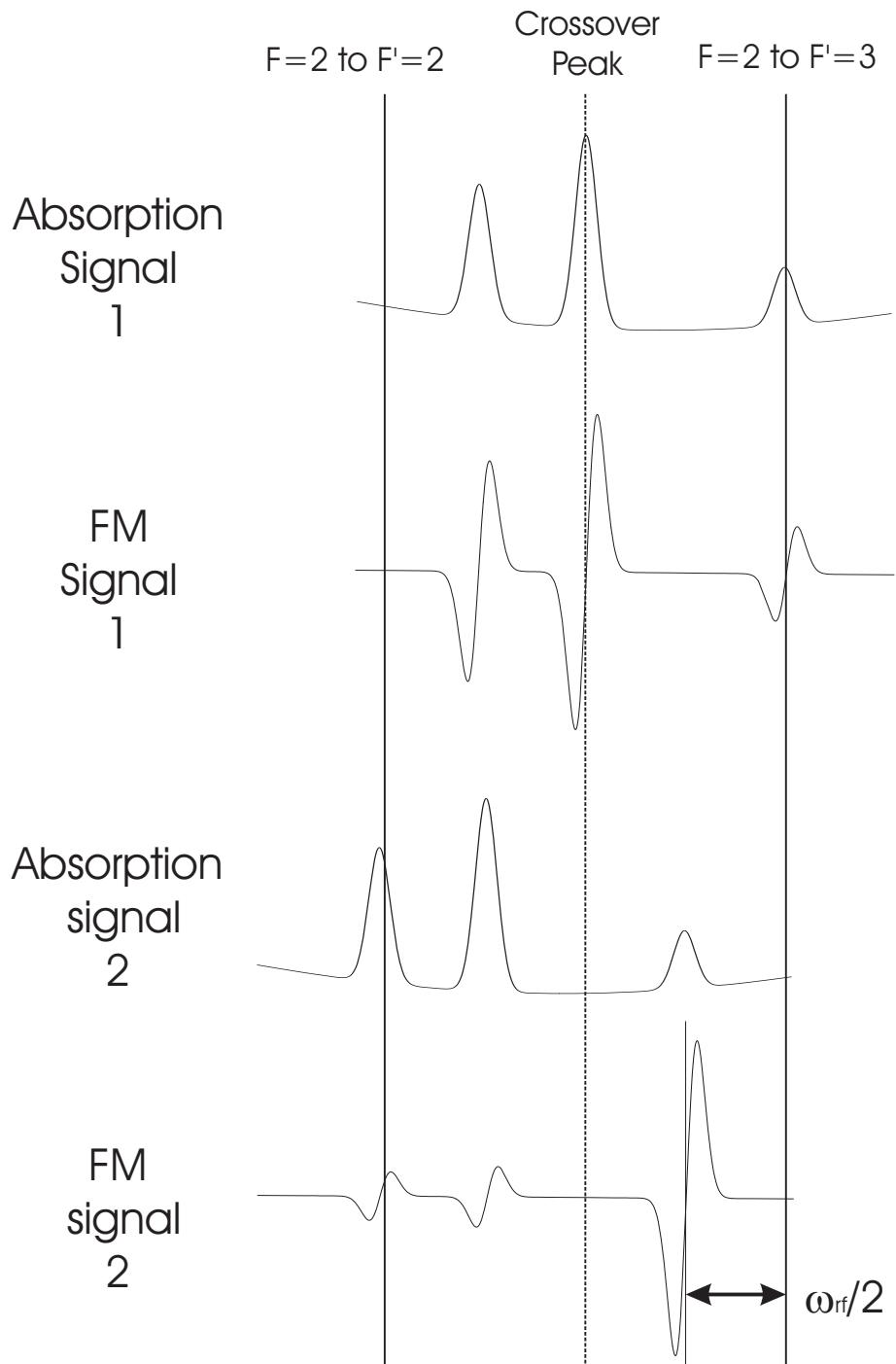
Figure 9: A schematic of the old and new SA signals. The two top signals are typical of the standard SA setup. The new SA signals shown on the bottom are shifted by half the center frequency of the AOM. With the second technique, the modulation frequency can be adjusted to selectively increase the size of a peak.
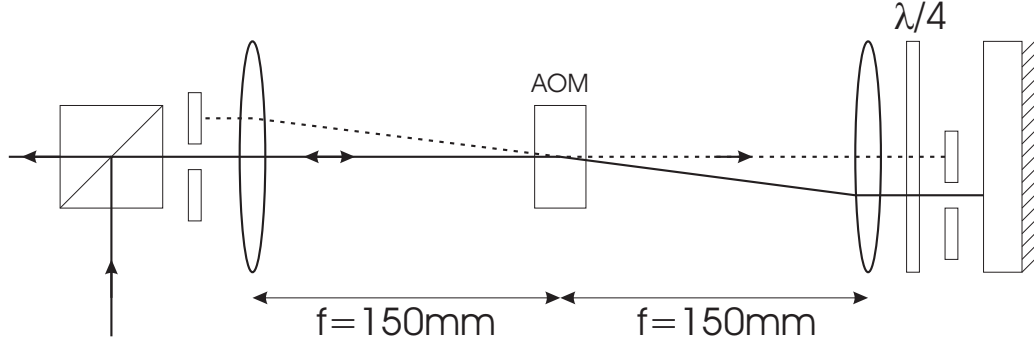
Figure 10: A double-passed AOM. Apertures block the 0-order beam outside the lenses. It is critical that the AOM be located exactly at the focus of the lens.

master and this power is unaffected by the efficiency curve of the tuning AOM. Double-passing minimizes deflection of the diffracted beam when correctly aligned (see Fig. 10). This AOM can be tuned over 60 MHz which, when double-passed, leads to a frequency tunability of 10 MHz above the $5S_{1/2}$ $F = 2$ to $5P_{3/2}$ $F' = 3$ transition in ^{87}Rb to 110 MHz below it in the final experiment. Care must be taken when aligning the double-pass setup to avoid beam-steering effects while tuning the AOM. Beam steering in an injection lock setup will change the mode matching properties and prevent the slave from properly following the master laser.

The most critical aspect of this alignment is the placement of the two telescope lenses on either side of the AOM. These lenses are best aligned initially without the AOM. Then one places the AOM near the focus of the lenses and dithers the frequency over the tunable range with an appropriate AOM RF driver. The position of the AOM is correct when the pointing of the double-passed beam does not fluctuate as the frequency is dithered. This process does not eliminate the intensity modulation of the double-passed light due to the efficiency curve of the AOM crystal. To avoid injection problems while scanning the frequency, it is best to adjust the angle and power in the AOM such that the intensity of the double-passed light is equal at both extremes of the tuning range.

The slave laser's temperature can be tuned such that it outputs 120 mW while following the master laser. Light from the slave passes through an optical isolator and a final
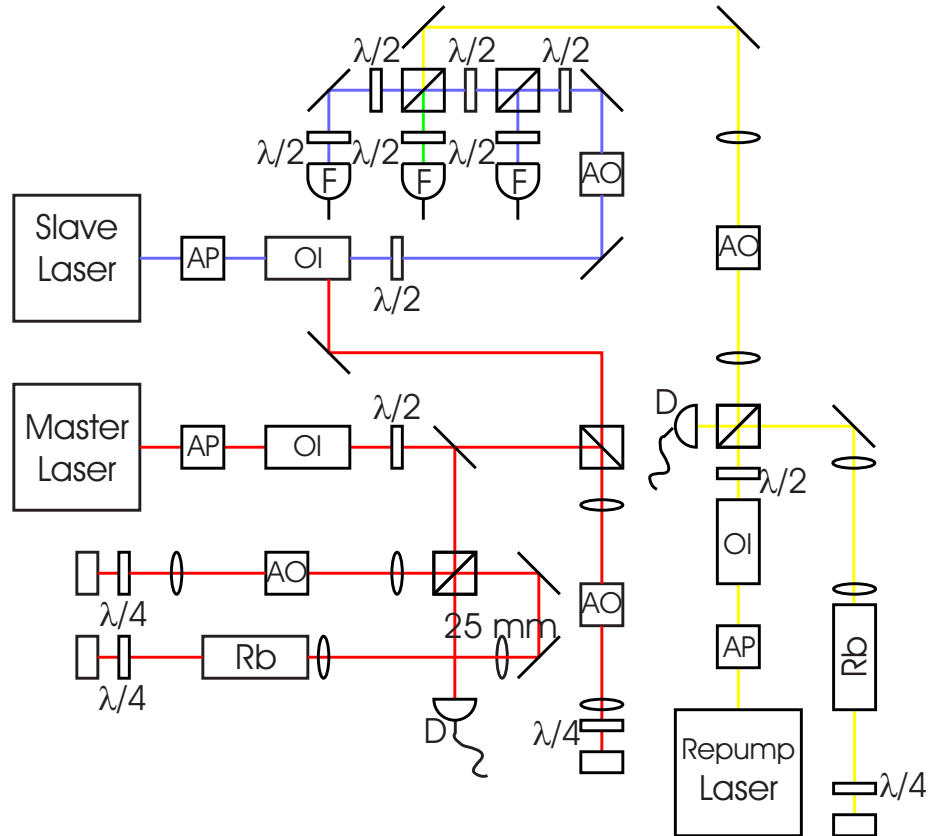
Figure 11: A simplified schematic of the MOT laser system. F-Single mode polarization maintaining fiber, AP-Anamorphic Prism, OI-Optical Isolator, AO- Acousto-optic modulator, D-Thorlabs PDA55 optical detector, Rb- Rubidium vapor cell, $\lambda/2$- Half waveplate, $\lambda/4$- Quarter waveplate. RED: master, BLUE: slave, YELLOW: repump. Every lens in this schematic has a focal length of 150 mm unless otherwise noted .

AOM used to control the intensity of the MOT light. We then couple 18 mW into each of three single-mode polarization maintaining (SMPM) optical fibers, which represents a mode-coupling efficiency of 75%. It is very important that the polarization of the input light exactly match the polarization axis of the fiber. Otherwise, the MOT will fluctuate on a timescale of seconds to minutes, adversely affecting experimental results. This is accomplished by placing half-waveplates in front of each fiber to align the light's polarization with the fiber axis. To align the waveplates, we place a Glan-Thompson prism at the fiber's output and adjust it for minimum transmission. Then we monitor the fluctuations in this transmission as we bend, squeeze, and roll the fiber between our fingers. The half-waveplate is correctly adjusted when the fluctuations are minimized. If the polarization is very far off, it might require an iterative adjustment of the Glan-Thompson to attain the minimum transmission. This highly effective process, also used in [66] prevents the polarization from slowly changing as the fibers are stressed and relaxed.

3.2.1.3 Repump Laser

The third laser is a free running diode laser locked to the $F = 1$ to $F' = 2$ transition. Without an external cavity, this laser's linewidth is much larger than the linewidth of the master or slave laser (20 MHz vs. $\sim$1 MHz), but this does not affect the performance of the MOT. The repump laser is tuned using temperature and current, and locked using a saturated absorption FM technique with PI control on the current modulation. Our repump at Georgia Tech has been "on transition" for over 4 years, surviving multiple power outages and a 10 foot translation of the optics table across the room. Furthermore, the free running repump is tuneable over all transitions in the D2 line of ^{87}Rb and ^{85}Rb and is not susceptible to even the strongest vibrations on the table due to its lack of external cavity.

3.2.2 Vacuum Chamber

We initially considered several different vacuum chamber designs, including a glass chamber which incorporated a large, external, water-cooled ring coil. In that chamber, we envisioned creating the MOT between the ring wires which would easily allow transfer of atoms into the storage ring. However, we halted progress on this design after it was accidentally destroyed

during the construction process. In the end, we decided on a more conventional multi-port chamber and a miniature wire guide.

We designed a chamber with large 4" diameter windows for flexible imaging of the atoms while in the ring. The aluminum substrate, on which the ring was constructed, was supported by 2 small feet at its base. We ran the current carrying wires through a UHV electrical feed-through to our electronic current controls on the outside of the chamber. The Rb source was located in a flexible bellows which connected via an elbow flange to the main chamber. When open, an an in-line vacuum valve provided direct line of sight from the top of the elbow to the location of the MOT (see Fig. 12) . Slight warming of the bellows and elbow decreased the loading time in the MOT and allowed us to iterate the experiment every 2-3 seconds.

We used 12 turns of 0.25" refrigerator tubing, wrapped in kapton insulation tape in an anti-Helmholz configuration to produce the field gradient necessary for the MOT. Water runs through these coils to remove heat generated by Ohmic losses. The diameter of each coil was 150 mm and they were separated by 160 mm. A large 15 kW power supply provided the current for the coils, while an integrated gate bipolar transistor (IGBT) allowed us to switch the current off in $<10\mu$s. At a nominal current of 50 A produces a field gradient of ~ 6 G/cm.

3.2.3 Construction of Storage Ring

We now turn our attention to the design and construction of the ring itself. A theoretical discussion of magnetic guides has previously been given in section 2.2. In particular, we derived the potential for a self-contained two-wire guide and saw that for two parallel current carrying wires, there is a minimum in the guiding potential located halfway between both wires. We chose this configuration for our storage ring because of its simplicity and adaptability to a planar geometry. For the first attempt at the storage ring, we designed a geometry that could be loaded in a steady-state configuration with constant currents in the support wires. A schematic and picture of this first construction is shown in Fig. 13. The scaling laws we derived in section 2.2 would suggest building the smallest geometry
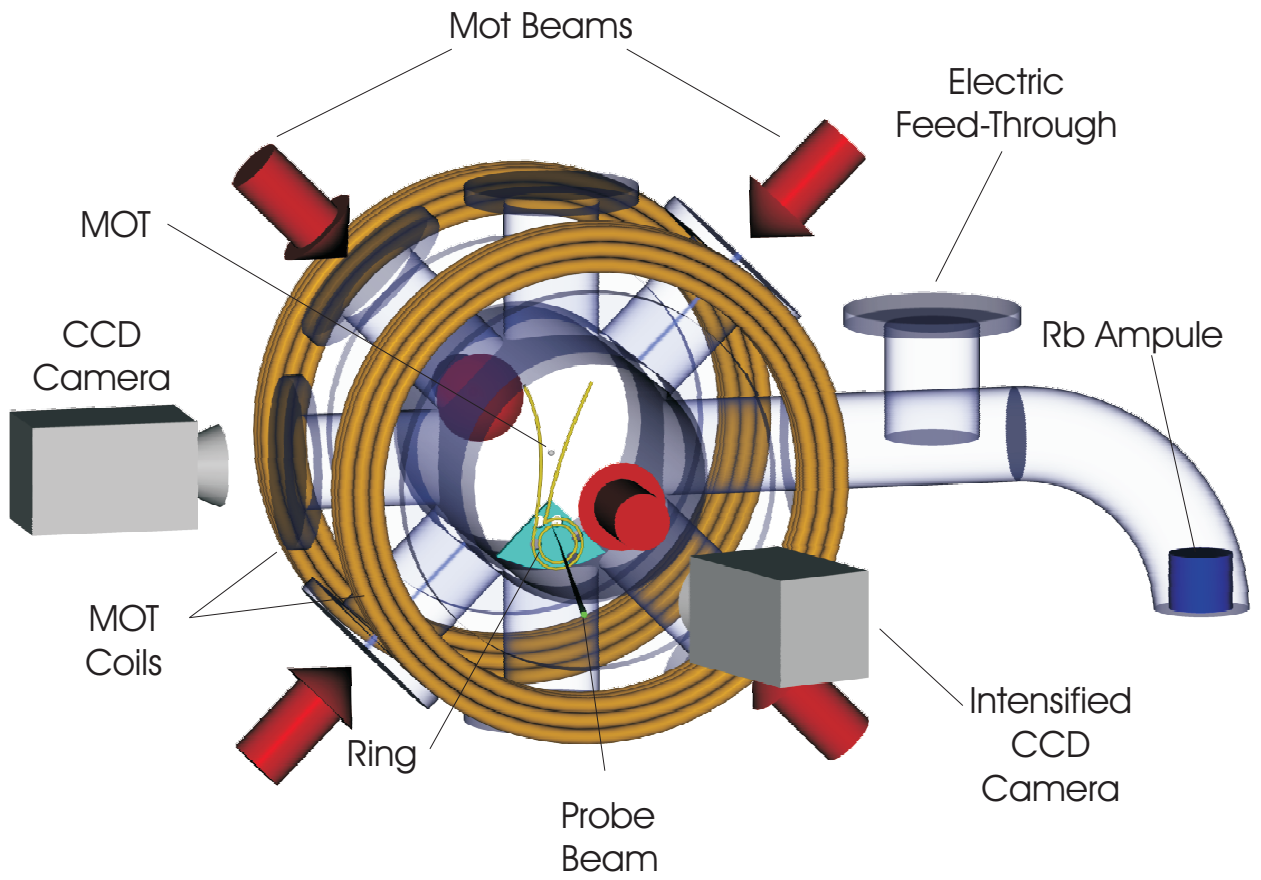
Figure 12: A simplified schematic of the storage ring experiment is shown.
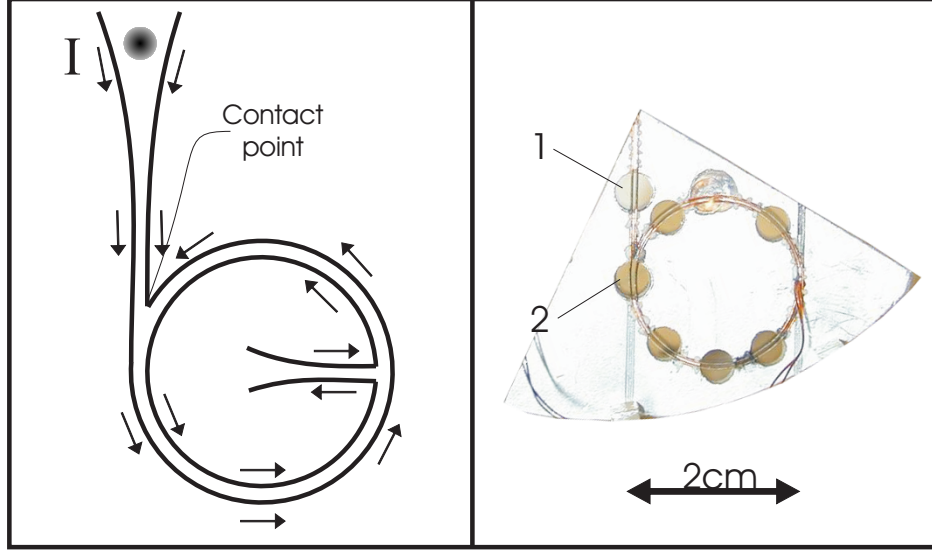
Figure 13: (left) The original ring design had a steady-state potential. The MOT formed between the wires and was channelled down to the ring area. Note the contact point of the ring with ground which allowed current to flow from both directions towards a single point. (right) A picture of the actual ring shows the construction technique that was used. The holes in the substrate were used for imaging of the atoms in the ring.

possible. However, the current necessary to produce an adequate guiding field at a finite distance from the MOT places technical constraints on the size of the system. We chose wires with a diameter of 240 μm that could handle a constant 3 A in vacuum and 300 ms bursts of up to 8 A. At this burst current, the wires would provide a guide depth of 0.53 mK with a separation of 4 mm at the location of the MOT. In the ring, where the wires are separated by only 840 μm, there is a field gradient of 1800 G/cm, a mean trap frequency of 590 Hz, and a trap depth of 2.5 mK for the $F = 1$, $m_F = -1$ ground state of ^{87}Rb. The use of the term "mean trap frequency" is justified because the guiding potential is not harmonic and the oscillation frequency depends on the energy.

We selected a 3 mm aluminum substrate for the construction of the ring. Aluminum is a good choice because it is light, easy to machine, non-magnetic, and works well in a UHV environment. Additionally, aluminum has a high heat capacity, which provides an excellent
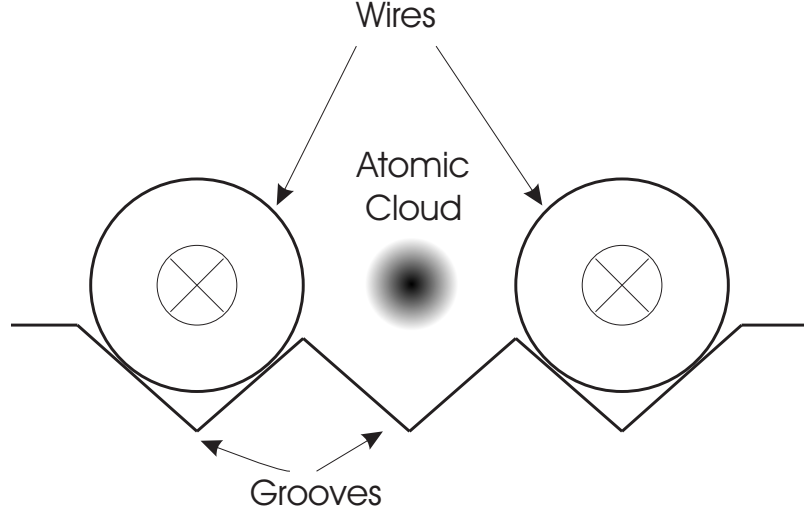
Figure 14: A cross section of the storage ring. The outer grooves support the ring wires, while the center groove is a free channel for atom guiding.

heat sink for the heat generated in the ring wires. A milling machine and metal lathe were used to scratch 3 parallel grooves in the substrate along the wire paths. The wires sit in the outside grooves, while the atoms travel down the center groove (see Fig. 14). The copper wires have a small sheath of high temperature insulation (Poly-imide) to prevent current from shorting to the aluminum plate. Several holes were drilled through the aluminum to allow for observation of atoms while inside the ring.

The top portion of the ring consists of free standing wires that we bent into position during alignment inside the vacuum chamber. The magnetic force between parallel wires of length l with a separation of d which both carry a current I is attractive and has a magnitude of:

$$\frac{i^2 l \mu_0}{2\pi d} \tag{14}$$

Even at the smallest separation of the free standing wires, and a maximum current of 8A, this force is only ~ 0.001N. We thus expected no disturbance in the ring structure from magnetic forces.

To construct the ring, wires are placed in the appropriate grooves and fastened at several locations with tiny self-made clamps. Small dots of Torr-Seal(tm), a low vapor

pressure epoxy, were used to permanently attach the wires to the ring. This epoxy is indeed quite strong, although its maximum temperature is only 120 C, which limits the bakeout temperature.

After the ring was constructed, we use graphite-based paint to coat the portion of the wires that extended to the MOT. This reduces MOT light reflections that can perturb the atoms in the MOT. This was later shown to have a negligible effect on the MOT and was thus not repeated in the second generation of the storage ring.

Of particular importance is the "contact point" displayed in Fig. 13. The steady state loading design required an apparent singularity in the current flow at this point. We circumvented this problem by removing a small section of the insulation from the copper wire and allowing current to flow into the aluminum substrate.

3.2.4   Imaging

A CCD camera recorded florescent images of the atoms while in the MOT and guide area. For this imaging, the MOT light was shifted on resonance for 1 ms while the camera's shutter was electronically activated. This camera did not allow a reset of the shutter timing, so we had to trigger on the camera's video signal to time the whole experiment! The wires were also illuminated by the probe light, so it was necessary to subtract a background containing these illuminated wires from each image of the cloud. To eliminate fluctuations in MOT intensity from this process, a new background was taken after each iteration of the experiment.

Imaging atoms in the ring was more complicated. We focused resonant light through the ring wires at one of several holes drilled through the aluminum plate (See Fig. 13). This beam also contained light from the repump laser. We recall from Eq. 9 that an atom can scatter a maximum of $\gamma/2$ photons per second. Since each photon carries a momentum of h/λ this produces a lateral acceleration of:

$$a_{light} = \frac{\gamma h}{2\lambda m_{Rb}} \tag{15}$$

This translates to an impressive $1.1 \cdot 10^5$ m/s^2 or over 11,000 times g! If a single probe beam were used, this tremendous acceleration would remove atoms from the probing region before
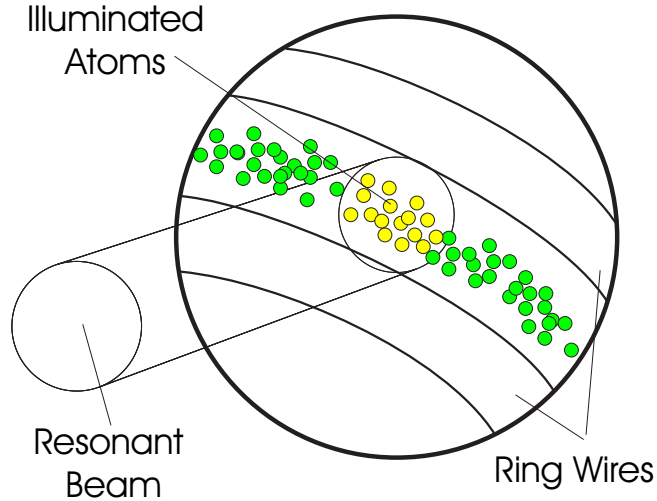
Figure 15: The imaging inside the ring required an additional probe laser beam that was focused between the wires.

they could be properly imaged. Therefore we retro-reflect the laser beam back through the wires to increase the probe time. Since the light is incident from both sides, there will be no net acceleration. However, there will be a momentum diffusion of the atomic cloud leading to an increase in rms size given by [67].

$$\sqrt{\frac{\gamma}{6}} \frac{ht^{\frac{3}{2}}}{\lambda m_{Rb}} \qquad (16)$$

Here t is the probe time ($\sim 500 \mu s$ for atoms in the ring). This leads to a increase in size of $150\mu m$ which is 4 times smaller than the active region of the probe. We used an Andor intensified CCD camera (Andor model DV 434 FI) to image the atoms in the ring. The Andor provided excellent dynamic range, which was critical for alignment and detection of the initially weak atomic signal.

3.3 *First Generation Data*

3.3.1 Observing a MOT Between the Wires

Producing a MOT between closely spaced wires is tricky. Possible reflections and shadows from the wires can reduce the atom number and MOT size considerably. Additionally, there are random fluctuations in the MOT light intensity and polarization that somehow seem

amplified when in the vicinity of wires. It is possible, nonetheless, to find a position for the MOT between the wires that is relatively stable and allows reproducible data to be taken.

After maximizing parameters, we were able to produce a MOT of about $\sim 6 \times 10^6$ atoms after 2 s of loading. The MOT is made by 3 retro-reflected laser beams, each having an intensity of 12 mW/cm^2 and a $1/e^2$ diameter of 1 cm. The trap lasers are tuned 17 MHz below the $5S_{1/2} - 5P_{3/2}$ $F = 2$ to $F' = 3$ transition, while the anti-Helmholtz coils generate a magnetic field gradient of 6 G/cm. An additional laser beam tuned to the $F = 1$ to $F' = 2$ transition with an intensity of 4 mW/cm^2 repumps the atoms decaying into the $F = 1$ state. Refer to Fig. 12 for a schematic of the chamber.

To image the atomic cloud, the MOT light is shifted on resonance for 1 ms while the camera's electronic shutter is open. We calibrate the camera with a photodetector by collecting light from the fluorescing MOT and compared this with the number of counts recorded by the CCD array in an area surrounding the atomic cloud. Only the light due to the MOT, and not from the wires, counted towards our calibration. The number of atoms in the MOT (N) can be estimated by dividing optical power collected by the photodetector (P_d), by the power radiated per atom and the collection efficiency. This gives us:

$$N = \frac{P_d 8 l^2 \lambda (1 + s_0 + (\frac{2\delta}{\gamma})^2)}{d^2 h c s_0 \gamma} \tag{17}$$

Here λ is the wavelength of resonant light (780.247 nm), γ is the resonant scattering rate ($2\pi \cdot 6$ MHz), d is the diameter of the imaging system, l is the distance from the lens to the MOT, and s_0 is ratio I/I_0 of the six beam light intensity to the saturation intensity of our atom ($I_0 = 1.5$ mW/cm^2). Fig 16 shows a typical MOT image between the two guide wires.

3.3.2 Sub-doppler cooling

A brief description of the σ_+-σ_- sub-doppler cooling used in this experiment was given in section 2.3.2. The most efficient transfer of atoms to the guide occurs when they are the coldest. While the MOT itself was quite tricky to produce between the guide wires, we were able to perform sub-doppler cooling of the atomic cloud quite easily. We believe this
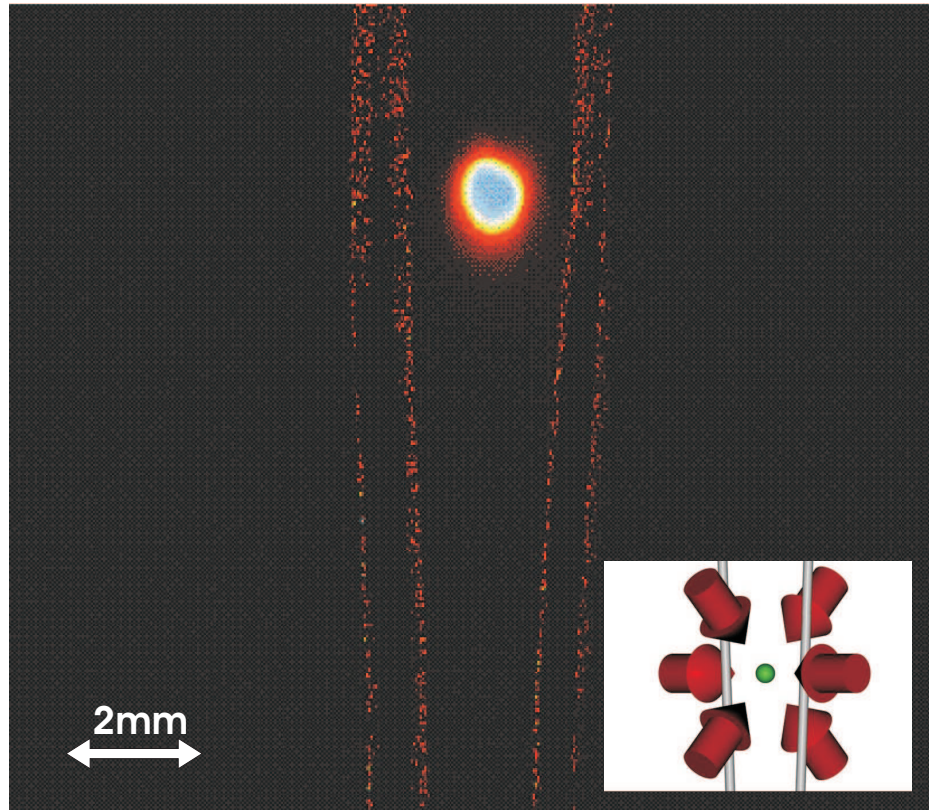
Figure 16: A fluorescent image of 6 million ^{87}Rb atoms between the guide wires is shown. Although the background of bright wires has been subtracted from this image, the outline of the wires is clearly visible. (inlay): The MOT beam configuration is shown with the guide wires. The wires make an angle of 45° with the laser beams so that the shadows from the wires do not overlap the MOT

is because the sub-doppler cooling time is much faster than the fluctuations and loading time of the MOT.

To cool the atoms well below their doppler temperature, we shut the MOT coils off very rapidly using the IGBT at the start of the sub-doppler cooling period (which we designate as t=0). The detuning is then linearly ramped to 100 MHz below resonance from $t = 0$ ms to $t = 3$ ms. We also ramp off the MOT-light from $t = 2$ ms to $t = 3$ ms. Good sub-doppler cooling requires low magnetic field at the location of the atomic cloud. We constructed three orthogonal pairs of Helmholz coils and nulled the field to first order by ensuring that the MOT did not move when the field gradient was ramped up and down. The sub-doppler cooling is optimized by minimizing the temperature using a ballistic expansion technique that will be described in section 3.3.5.

3.3.3 First Atomic Guiding

Injection of current into the guide wires during the final stages of sub-doppler cooling produced a dramatic change in the expansion of the atomic cloud. Fig. 17 depicts a typical loading sequence into the magnetic guide. Here, we see compression of the cloud in the horizontal direction due to narrowing of the guide wires as the atoms fall. The guiding potential provided by our 2-wire configuration was given in Fig. 4. We impose this potential onto the atomic cloud by rapidly increasing the current in the guide wires to 8A over a period of 5-7ms using a computer controlled DC power supply (EMI, EXX 15-20). Clearly the position of the MOT is important for efficient coupling into the atomic guide. We found that the best coupling into the guide occurred when the MOT was slightly off-center. This was probably due to a small imbalance in the light intensity of the MOT beams which imparted a non-zero center of mass velocity to the cloud during the final stages of sub-doppler cooling.

3.3.4 Guide Loading Efficiency

Given a random distribution of atoms over the three magnetic sublevels of the $F = 1$ manifold, one expects a theoretical maximum of 1/3 of the atoms to be trapped in the weak-field seeking state $m_F = -1$. Ultimately about 1/6 of the atoms could be coupled
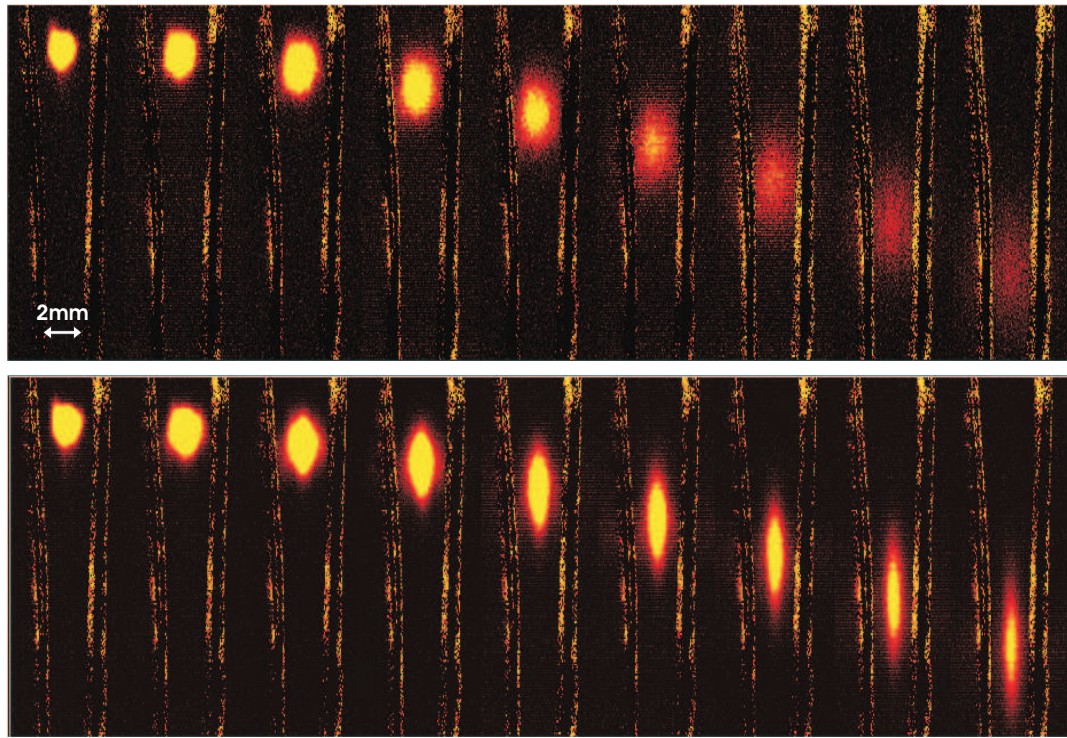
Figure 17: (top) An image series spaced at 2 ms intevals shows a cloud of 6 million ^{87}Rb atoms falling under gravity as it undergoes ballistic expansion. Here, the guiding wires play no role in shaping the cloud. (Bottom) The current in the guide wires has been turned on, which shapes and guides the cloud of atoms. Note the narrowing of the RMS size of the cloud as it falls to the bottom
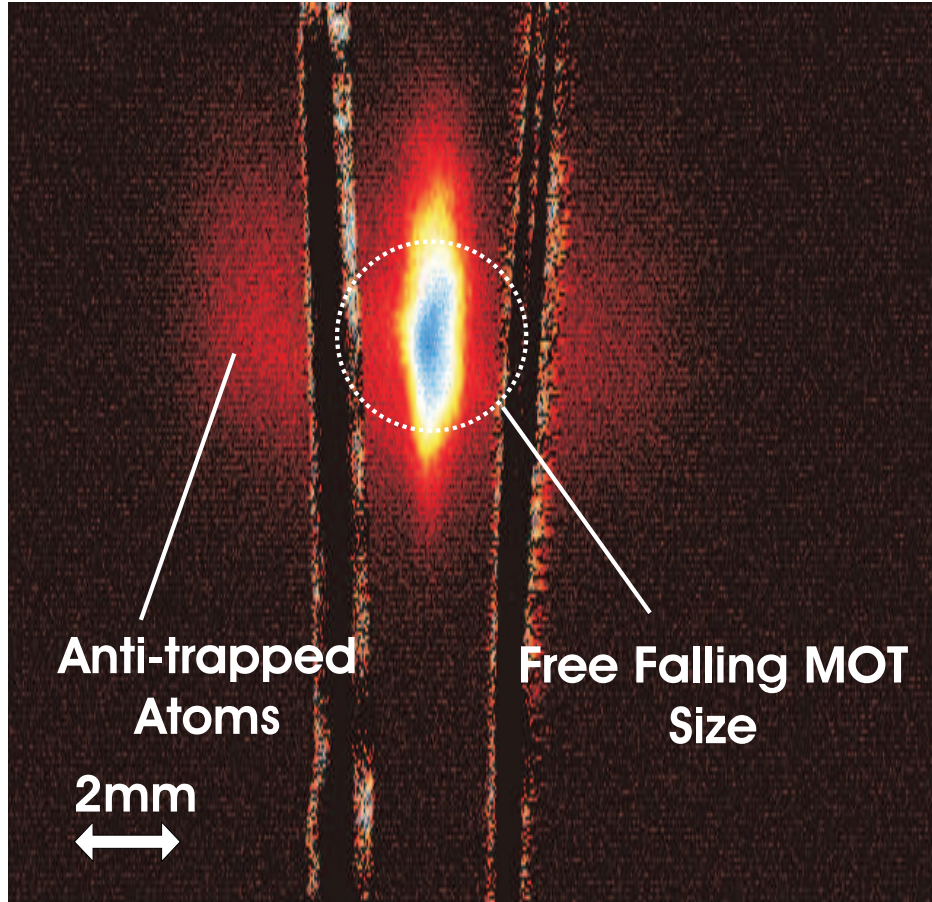
Figure 18: An image of the guided atoms shows strong seekers fleeing the trap. For comparison, we also include the size of the free-falling MOT.

into the guide. This was measured in the upper imaging area as well as below on the aluminum substrate. Fig. 18 shows an image of the atoms after being compressed into the trap. One can see the atoms in the strong-field seeking states being ejected from the trap outside the wires. Those atoms in the $m = 0$ state are unaffected by the magnetic force and behave just like the free-falling atoms. In order to correctly count the number of atoms transferred into the guide, the $m = 0$ atoms must be subtracted from the total signal. Practically, this is done by subtracting $1/3$ of the atoms counted during free-expansion with the wires off from the total signal with the wires on. A graph of these quantities versus time is shown in Fig. 19. In principle, one could use optical pumping to transfer all atoms to the trapped state, which should increase the coupling into the guide threefold. However, this was not necessary for observation of loading efficiency.
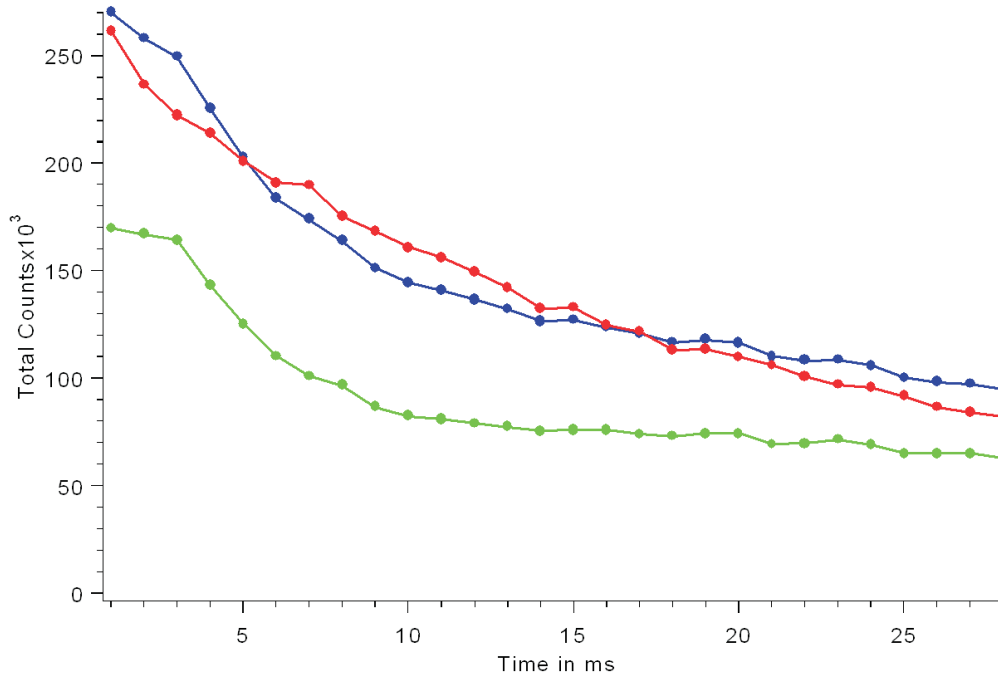
Figure 19: Vertically integrating the atom's fluorescent signal shows the coupling into the guide. The top curve (blue) shows guiding with the wires on, while the middle curve (red) shows no guiding. The bottom curve (green) is calculated by subtracting 1/3 of the free atoms from the top curve. This accounts for the atoms in the m=0 state.

In principle, one could use optical pumping to transfer all atoms to the trapped state, which would increase the coupling into the guide threefold. However, this was not necessary for observation of loading efficiency.

3.3.5 Temperature Measurements in the Guide

A common technique in laser cooling uses ballistic expansion of the cloud to determine the atomic temperature [58, 68]. The expansion of a thermal cloud with an initial gaussian density profile results in a new gaussian profile of width [58]:

$$\sigma^2 = \sigma_0^2 + \frac{k_b T}{m} t^2 \tag{18}$$

Where σ_0 is the initial size of the atomic cloud and t is the expansion time. We calculated the temperature of atoms in the guide by first binning the atomic signal in the horizontal
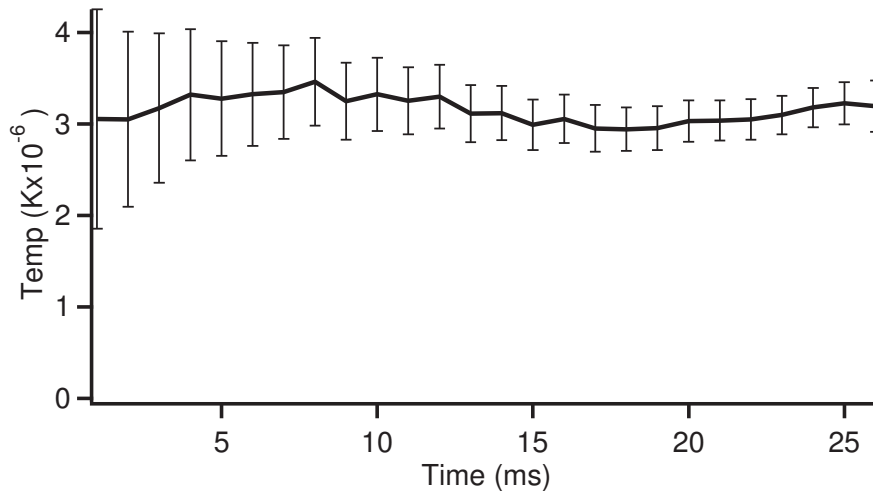
Figure 20: We plot the vertical temperature of the atomic cloud during coupling into the guide. The temperature of $\sim 3\mu K$ agrees well with the measured MOT temperature. The error bars indicate the uncertainty in the gaussian fit.

direction between the wires and then fitting a gaussian distribution to this binned sum:

$$D(z) = A_{x,y,z} \int_b^a \int_{-\infty}^{\infty} \frac{1}{\sigma_x \sigma_y \sigma_z (2\pi)^{\frac{3}{2}}} e^{\frac{-x^2}{2\sigma_x^2} + \frac{-y^2}{2\sigma_y^2} + \frac{-z^2}{2\sigma_z^2}} \, dx dy \qquad (19)$$

$$D(z) = B_z \frac{1}{\sigma_z \sqrt{2\pi}} e^{\frac{-z^2}{2\sigma_z^2}} \qquad (20)$$

This distribution is also gaussian with the same width in the z direction. Here, we neglect the small vertical component of force from the slightly angled wires. A plot of the measured longitudinal temperature is given in Fig. 20. We shall henceforth refer to a transverse and longitudinal (radial and azimuthal once in the ring) temperature separately because the 2-dimensional potential and the low density after expansion in the guide reduce collisions among the atoms so that they do not thermalize.

3.3.6 Observation of Atoms on the Substrate and Failure of the First Generation Ring

We used the second imaging technique discussed in section 3.2.4 to detect the atoms over the aluminum substrate. As expected, the atomic signal appeared while imaging through hole #1 of Fig. 13. The atomic profile expected in the guide is the product of the integrated

2D density ϱ_0 with a gaussian distribution:

$$\rho(z) = \varrho_0 \frac{1}{\sqrt{2\pi}\sigma_z} e^{\frac{-(z - z_0)^2}{2\sigma_z^2}} \tag{21}$$

However, σ_z is time dependant and given by:

$$\sigma_z = \sqrt{\sigma_0^2 + (vt)^2} \approx vt \tag{22}$$

Where v is the relative vertical rms velocity of the atomic cloud. σ_0 can be neglected for the relevant time scales. Furthermore the whole cloud is falling under gravity past a stationary point. This can be accounted for by making the transformation $z \rightarrow -gt^2/2$ which gives us:

$$\rho(z) = \varrho_0 \frac{1}{\sqrt{2\pi}vt} e^{\frac{-(z_0 - \frac{gt^2}{2})^2}{2(vt)^2}} \tag{23}$$

Thus we expect to observe a skewed gaussian-like curve from which we can extract atom number and temperature for comparison with the upper imaging area. The temperature is calculated using Eq. 18 and the measured value of v. Atom number is estimated by integrating the total fluorescence signal and multiplying by the ratio of the step size to the probe length. We calibrate the Andor intensified CCD camera with the MOT using the same technique as mentioned above.

Fig. 21 shows that this does indeed fit the experimental data quite well. This data was taken by summing all the fluorescent counts over a $500\mu m \times 500\mu m$ "active" region on the image. Each data point represents a different image taken successively at 0.5 ms intervals. The temperature of this cloud is 3.4 ± 0.2 μK, while the atom number is $6.3 \pm 0.7 \times 10^6$.

Unfortunately, we failed to observed any significant fluorescence signal from atoms in the ring. This meant that while the guide was indeed transporting atoms from the MOT onto the aluminum substrate, there was little or no coupling of these atoms into the storage ring.

3.4   Second Generation Ring: The Nevatron

Our steady state ring configuration was unable to couple atoms into the ring. We were aware that there are difficulties associated with the steady state operation of the optical
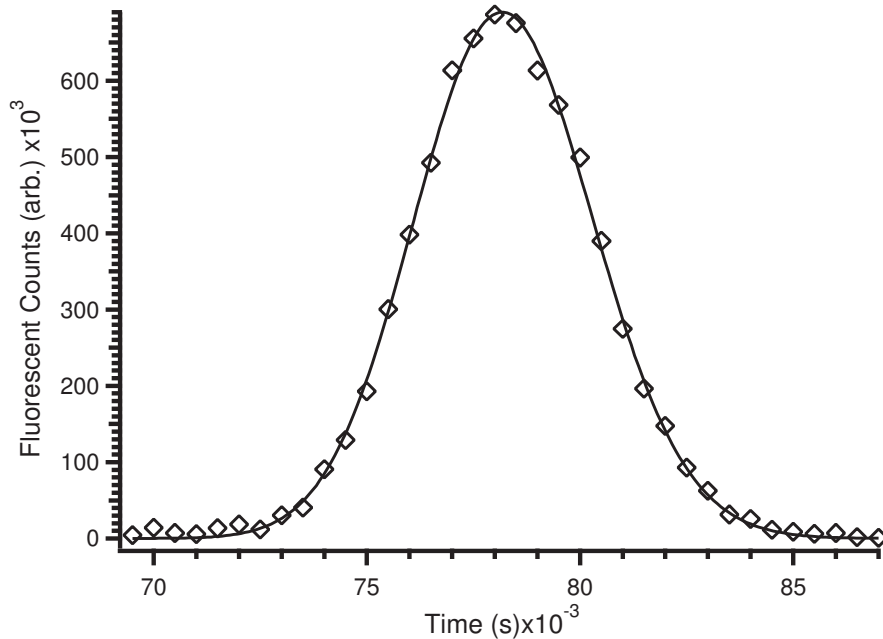
Figure 21: A plot of the density profile of the atomic cloud is displayed along with the theoretical fitting curve. This profile was constructed by summing the fluorescent counts in an active region versus time.

analog of our design, a three-port beamsplitter. The main problem with loading conservative potentials in a steady state operation is that this increases the phase space density inside the trap and would thus violate Louiville's theorem. One way around around this obstacle is to change to a time-varying potential, which is no longer conservative. In the new design, the guide and the ring would be separate entities, connecting in an "overlap" region. We proposed to "switch tracks" in the guiding system, while the atoms traverse this overlap. In the next few sections, we discuss the construction of this new ring, its loading and orbits, cloud shaping, a dual loading technique, and finally the trap lifetime.

3.4.1 Construction of a New Ring

We constructed the second ring similarly to the first. The aluminum substrate was made thinner and had a raised lip to allow for the guide wires to run along the top of the ring wires (see Fig. 22). Also, the substrate was shaped asymmetrically, which allowed for better imaging and a straighter trajectory from the MOT into the ring. The new ring had no "contact point" because the currents in the guide and ring were separate structures.
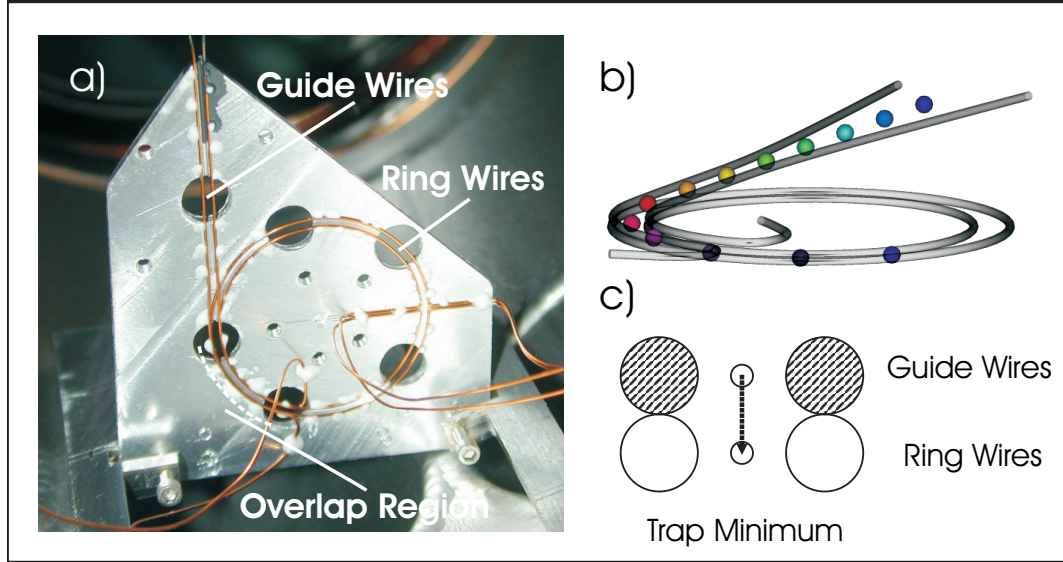
Figure 22: a): A photograph of the second generation ring shows the overlap area and separate guide and ring structures. Note the right section of the ring where the current feeds in and out. b): A rendered version of the ring shows the atomic guiding path as it enters the ring. c): Shifting the current from the guide wires to the ring wires lowers the atomic cloud into the ring in the overlap region.

This point had failed several times on the first generation ring, causing us to repeatedly break vacuum and make adjustments.

Additionally, we changed to a new atomic source for this experiment. On the suggestion of Prof. Phil First we placed an unbroken vial of Rb in the vacuum chamber during the bake-out process. After baking, we closed the valve to the source and crushed the glass vial, releasing the Rb into the source section of the chamber. Next we slowly opened the valve to release the trapped gases to our external pumping station. This technique allowed us to bake the source section of the chamber as well and ultimately achieve a pressure of $< 10^{-10}$ at the location of the pump. The new source did not change the size of the MOT or its temperature.

3.4.2 Transfer into the Ring and Atomic Orbits

We load the new guide in exactly the same fashion as the old one, with one exception: Because the atomic cloud must cross over a section of the ring, we first only allow current to flow in the guide wires. Once in the guide, the atoms fall 4 cm under gravity to the 15
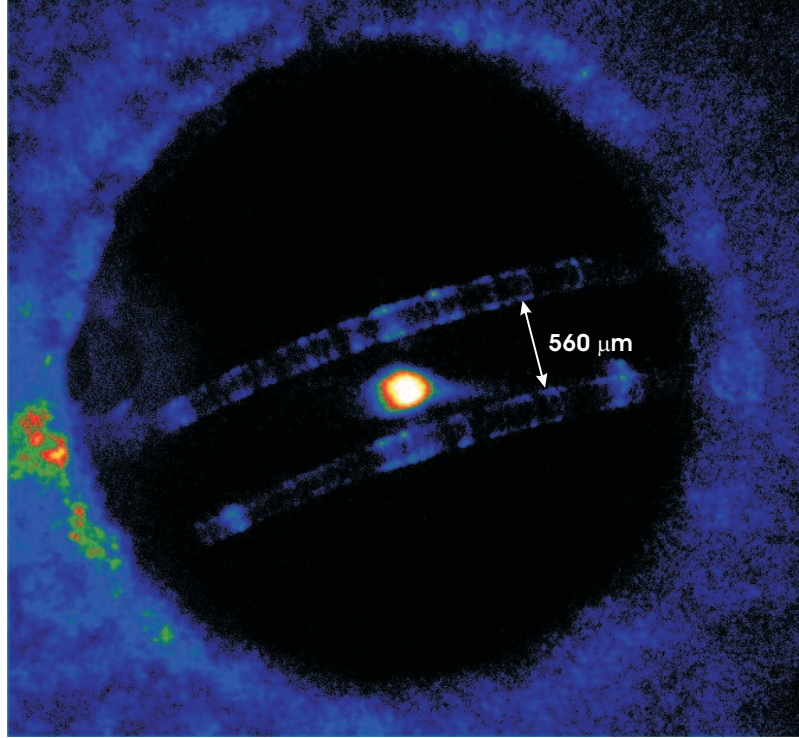
Figure 23: A fluorescence image of neutral ^{87}Rb atoms in the storage ring. This image was taken with an ICCD camera exposed for 1ms. The outline of the ring wires is visible in this image.

mm overlap with the ring. To transfer the atoms from the guide to the ring, we linearly ramp the current in the guide off while simultaneously increasing the current in the ring to its final value. This process transfers the trap center from the guide to the ring.

The transfer efficiency to the ring is estimated to be $> 90\%$ measured by comparing the atom number in the guide and at a different point in the ring. Optimal transfer is achieved for equal maximum currents in the guide and ring and a transfer time of 16 ms. For longer transfer times, the cloud traverses the entire overlap region before transferring completely to the guide—for shorter times, we measure losses from the cloud, possibly due to heating.

One of the first images of atoms that have successfully completed an orbit in the ring is shown in Fig. 23. The corresponding atomic orbit is mapped out in Fig. 24. This data is collected by summing the atomic fluorescence between the wires at the top port on the ring. Every data point represents an iteration of the experiment, spaced 1 ms apart at a probe time of 1 ms. Each peak represents a complete revolution of the atomic cloud in the storage
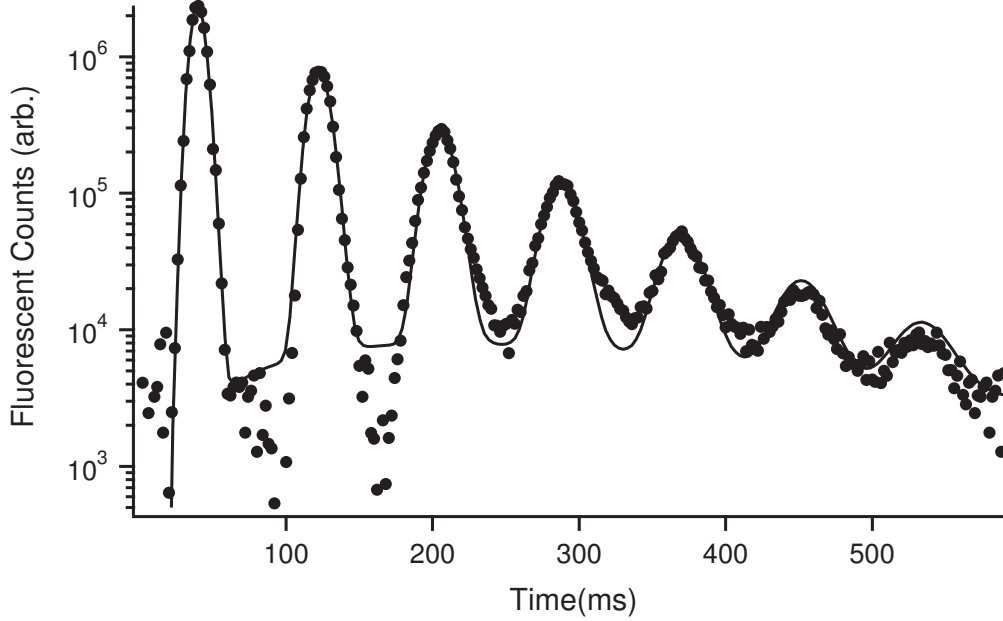
Figure 24: 7 complete revolutions of the atoms in the storage ring can be seen as individual peaks on this graph. The data points represent atomic fluorescence versus time, while the curve is a theoretical model of the expanding atomic cloud.

ring, and 7 complete revolutions of the ring are clearly distinguished. The measured orbit time of 81 ms corresponds to an average velocity of 85 cm/s, which is consistent with a 4 cm free-fall. We model this data by incorporating a loss term: $e^{-\gamma t}$ into Eq. 23 to account for the decreasing atom number and extending this formula to include multiple orbits, while removing the acceleration term:

$$\rho_n(z) = e^{-\gamma t} \rho_0 \frac{1}{2\pi vt} e^{\dfrac{-(z_0 + v(nt_r - t))^2}{2(vt)^2}} \tag{24}$$

$$\rho(z) = \sum_{n=0}^{\infty} \rho_n \tag{25}$$

Here the nth term in the sum corresponds to a new orbit of the atomic cloud in the storage ring and t_r is the orbit time. The peaks fit reasonably well to this simple model. From this fit, the $1/e$ lifetime of the ring is determined to be 180 ms, and the azimuthal temperature is measured to be 3.4(3) μK, only slightly hotter than the temperature measured immediately after loading the guide. The number of atoms in the first peak is ~ 1 million.

The lifetime of the atoms in the ring depended on the ring current. The graphs in Fig.

47

25 show that as the current in the ring in increased from 3 to 6 A, the lifetime also increases fro 144 ms to 159 ms. Because of the heating at large currents, we were unable to test the ring at currents greater than 8 A. Increasing the pulsed current in the ring causes heating of the wires that adversely affects MOT formation and loading into the ring. At a current of 8 A, a 60 s cooling period must be introduced between each iteration to remove any heating effects on the storage ring while at 3 A, the experiment can be run without a cooling cycle.

3.4.3 Cloud Shaping

Cold pulsed atom extraction from the ring, as well as applications in cold collisions require narrow relative velocity distributions. To this end, we explored altering the azimuthal distribution of atoms in the ring by selectively removing portions of the cloud with a resonant beam. As shown in Eq. 15, the acceleration due to the scattering of resonant photons can be $1.1 \cdot 10^5$ m/s^2, which is large enough to remove the atoms from the storage ring. We use the resonant imaging beam to selectively alter the azimuthal velocity distribution of orbiting atoms. The original azimuthal velocity distribution has a width $\Delta v \sim 2$ cm/s corresponding to a speed ratio $v/\Delta v \sim 50$ in the ring. Because of the free expansion of the atomic cloud along the guide direction, the initial velocity distribution is mapped onto the azimuthal spatial distribution of the atoms in the ring. Hence the velocity distribution can be modified by selective temporal or spatial removal of portions of the cloud. Two such modifications are shown in Fig. 26. In both cases, the velocity distribution has been modified in the previous orbit (not shown) and traces show the evolution for subsequent orbits. In the bottom trace, only the central 40% of the FWHM has been preserved, corresponding to an increase of the speed ratio to 125. In the top trace, the central 40% of the FWHM has been removed, leaving a double-peaked distribution. In both cases, the subsequent evolution and broadening of the peaks occur at the expected rate, which is given by Eq. 24.

3.4.4 A Dual-Loading Technique

A long standing challenge in the field of atomic-motional manipulation has been the production of a continuous degenerate or near degenerate atomic beam. The ring geometry offers
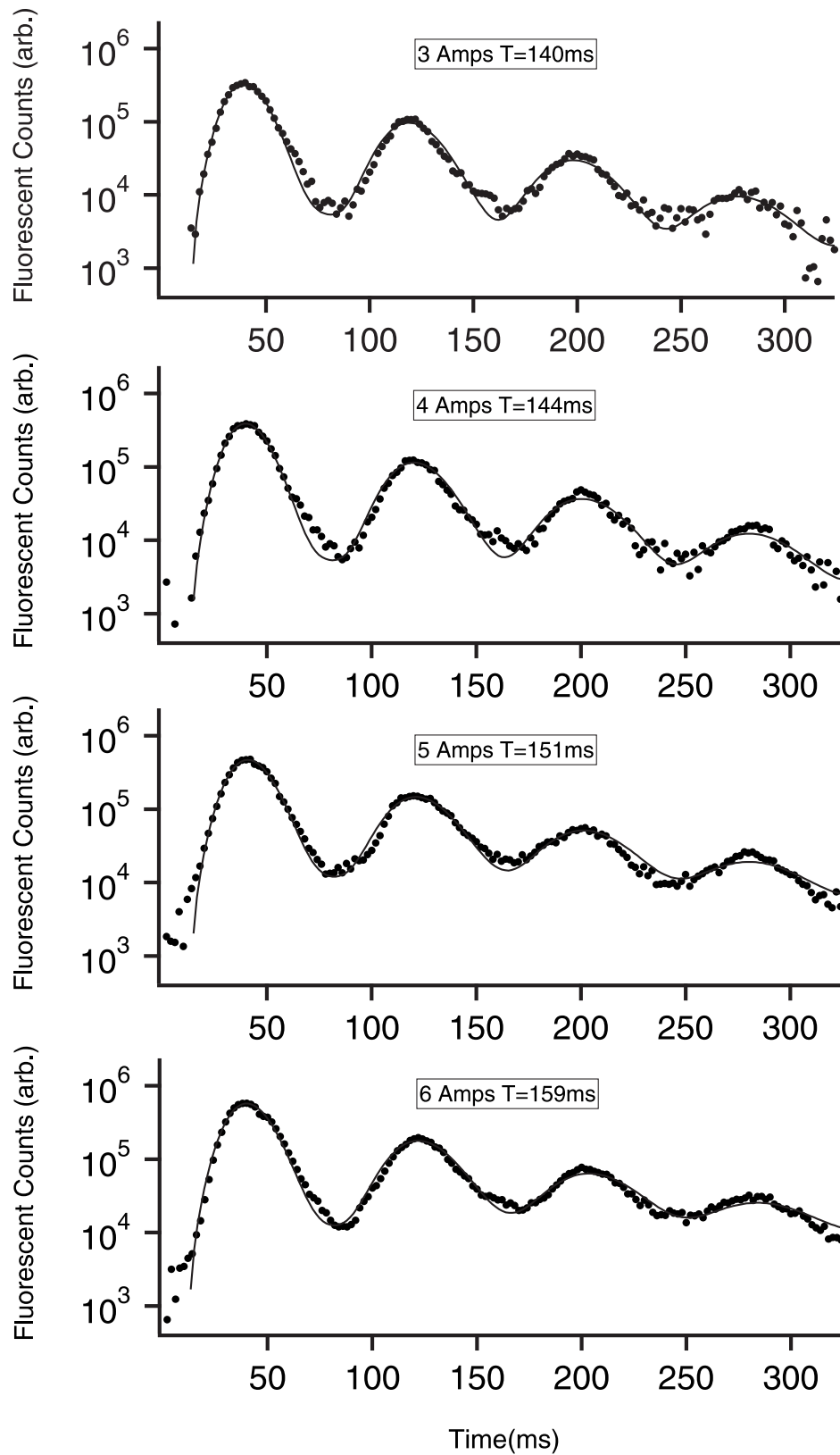
Figure 25: Four time series show the atomic cloud orbiting in the storage ring under different ring currents. We include the calculated lifetime with each current setting.
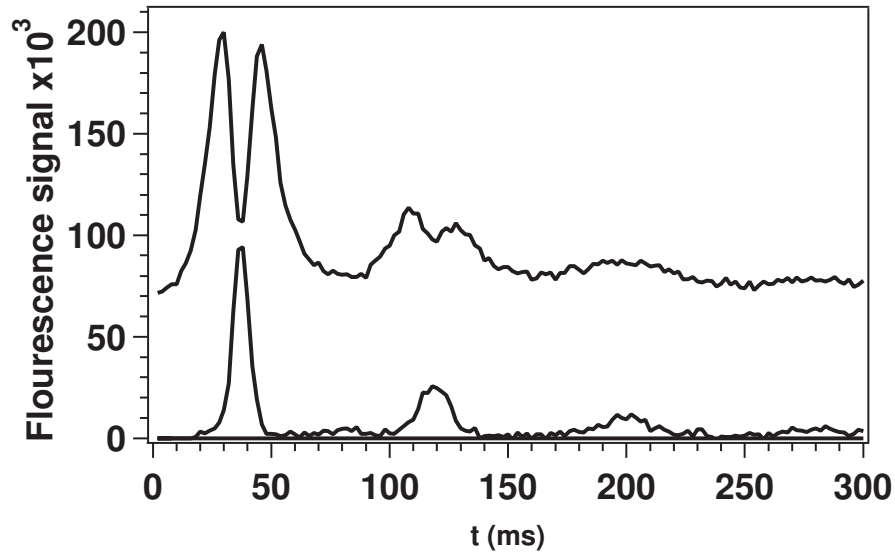
Figure 26: Deterministic pulse shaping. The upper graph corresponds to a cloud that has had its central portion removed. The lower graph shows a cloud with only a central portion. The two graphs have been offset by 70,000 counts for clarity.

the unique opportunity for multiple or even continuous loading in this respect, although cooling of the loaded atoms inside the ring would be necessary to increase the phase-space density. Cold, intense atomic beams could be generated by out-coupling the stored atoms at any desired rate (by employing laser induced Raman transitions to an un-trapped magnetic state for example). Those atoms that are not successfully out-coupled would be efficiently "recycled" in the ring for later use. We have taken the first steps toward this goal by demonstrating a dual-loading technique in our storage ring.

The original design of the storage ring allowed for steady state operation. However, we saw that this mechanism was unable to couple atoms from the guide into the ring. Although the new design incorporates a time-dependant potential, it is possible to couple a second cloud of atoms into the ring that orbit 180 degrees out of phase with the first. We achieve this by first coupling a single cloud into the storage ring, as described previously. Next, the MOT is reformed between the guide wires while the first cloud orbits in the ring. The current in the guide wires is then increased to an appropriate "capture" current (8 A) and a second cloud is transferred to the guide. As the second cloud falls, the first cloud must pass through the overlap region. The current in the guide is reduced to a minimum holding

50
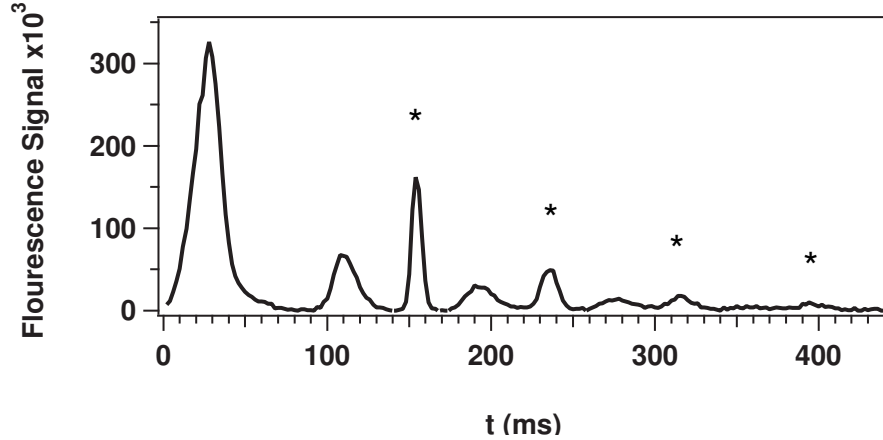
Figure 27: Dual loading of the storage ring. The clouds marked with a "*" are from the second atomic cloud. The two clouds are 180 degrees out of phase with a spacing of only 40.5ms

current of 3 A while the current in the ring is left at maximum current. The first cloud then proceeds past the overlap region, while remaining in the ring. After this, the current in the ring is reduced to a holding current of 3 A so the second cloud can move into the overlap region. Once inside the overlap, the guide current is extinguished while the ring current is increased to its maximum value of 8 A. This somewhat complicated process is necessary to ensure that neither section is perturbed too strongly by the magnetic field of the other.

After the second loading, there are two distinct atomic clouds orbiting 180 degrees out of phase with one another. (see Fig. 27). We observe that each cloud has the same lifetime and that their phase relationship is constant. Furthermore, the coupling of the second cloud into the ring does not reduce the number of atoms in the first cloud by more than 7%. However, due to the ring lifetime, we are unable to increase the total number of atoms in the ring using this technique. In this case, the loading time of the MOT takes so long, that the first cloud endures significant losses by the time the second is loaded.

3.4.5   Trap Lifetime

As mentioned previously in section 3.4.2, we measure a maximum 1/e lifetime of the atoms in the ring to be 180 ms. The lifetime is a natural figure of merit in this experiment, determining directly the number of orbits as well as the possibility for increasing the atomic density. Consequently, we have investigated the limits on our lifetime due to several effects,

including background gas collisions, non-adiabatic spin flips, and ergodic mixing.

Collisions with the background gas will ultimately limit the lifetime of any magnetic trap because the kinetic energies of these particles are on the order of 10^5 times larger than the magnetic trap depths. However, for sufficiently low background pressures, this lifetime can be made very long (several minutes in some cases). In calculating the loss rate due to background gas, we must keep in mind that this may be a very inaccurate. Materials near the storage ring, such as the Kapton insulation on the ring wires, could produce significant local outgasing that would raise the local pressure at the ring even though the total pressure might not change by much.

Nevertheless, we can calculate the theoretical pressure in the center of the chamber given the pressure measured at the ion pump, the pumping speed, and the conductance from the pump to the chamber [69]. The throughput to the ion pump is given by the product of the pressure at the pump and the pumping speed:

$$T_1 = P_1 S \tag{26}$$

While the throughput out of the chamber is given by the product of the conductance from the chamber to the pump and the differential pressure:

$$T_2 = (P_2 - P_1)C \tag{27}$$

In the worst case scenario (i.e. the only source of background gas is the chamber itself) we set these two throughputs equal to obtain:

$$P_2 = P_1 \frac{S + C}{C} \tag{28}$$

The conductance from our chamber to our pump can be obtained directly from the manufacturer of the vacuum parts (MDC) C=34 L/s. At our 75 L/s ion pump, we measure a pressure of $5 \cdot 10^{-10}$ Torr. This gives us a theoretical pressure of $1.6 \cdot 10^{-9}$ Torr at the location of the ring. The vacuum limited lifetime, generally given by $\tau \sim (10^{-8}/P)$ (where P is in Torr, see p. 128 of [50]), would be $\sim$ 6s. This is a factor of 35 longer than our measured lifetime of 180 ms of atoms in the storage ring. We therefore do not believe that collisions with the background gas are limiting our lifetime.

We next consider non-adiabatic spin flips or Majorana transitions [44] as a loss mechanism. As mentioned previously in section 2.2 atoms passing too close to the zero magnetic field point can make a non-adiabatic transition to an untrapped state and flee the magnetic guide. At the center of our guide, the magnetic field can be approximated by:

$$B_{center} = \frac{\mu_o I}{\pi a^2} \begin{pmatrix} y \\ x \end{pmatrix} \tag{29}$$

Where a is the separation between wires and I is the current in each wire. Thus an atom with mass m and velocity v passing within a distance d from the center of the trap can undergo a spin flip if the rate of change of the direction of the magnetic field (v/d) is greater than the Larmor frequency:

$$\frac{v}{d} > \omega_l = \frac{\mu_m \mid B \mid}{\hbar} = \frac{\mu_m d \mu_0 I}{a^2 \pi \hbar} \tag{30}$$

We find that atoms will be lost inside a cylinder of radius:

$$d = \sqrt{\frac{v a^2 \pi \hbar}{\mu_0 \mu_m I}} \tag{31}$$

This result follows the derivation presented in [32], which is done for a 3D trap. It also agrees with that presented in [70] in the 2D case. For the storage ring, this radius is 0.6μm. The flux of atoms through this cylinder is given by the cross sectional area of the cylinder times the density, times the average velocity. This average velocity can be obtained from the virial theorem, which states that $mv^2 = \mu_m B = \mu_m r B'$ where r is the radial cloud size and B' is the field gradient. Using the transverse temperature and cloud size in the ring, we calculate the lifetime due to Majorana transitions to be 300 ms. However, since both the velocity and the density increase with increasing current, we would expect this loss rate to increase as we increase the current in the ring. Fig. 25 shows exactly the opposite behavior. This suggests that the dominant loss rate in the trap is not due to such transitions. It is worth pointing out that suppression of these transitions can be avoided completely by adding a single wire along the axis of the storage ring. This wire would produce an azimuthal field that would prevent the B field from going to zero at the center of the guide.
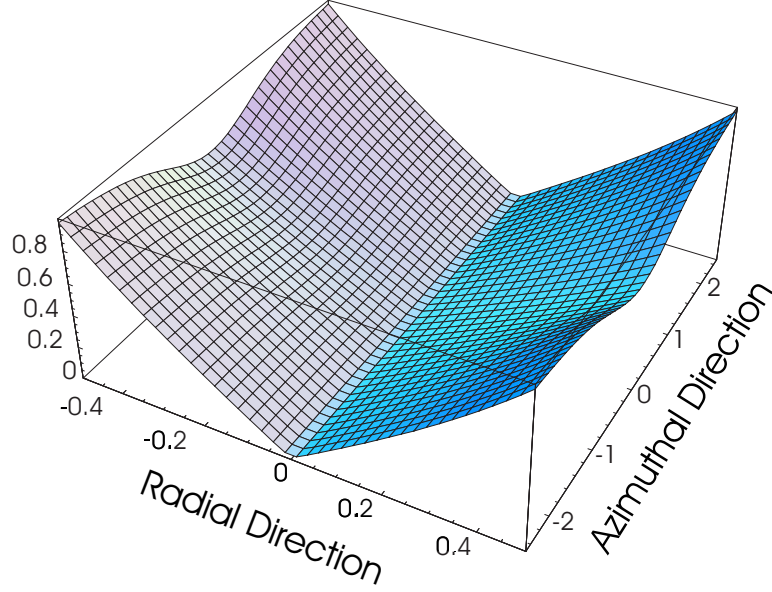
Figure 28: A plot of the magnetic guiding potential for the "bump" in the ring where the current is fed in and out. The length is normalized to the wire spacing, while the potential is normalized to the maximum trap depth.

A final effect that could lead to trap loss is ergodic mixing of longitudinal and transverse motion due to irregularities in the construction of the ring. The most obvious irregularity in the magnetic field occurs at the far right side where current is fed in and out horizontally. Fig. 28 shows a plot of the potential over the suspect area. We estimate this "bump" in the potential modulates the trap depth at 20% over 250 μm. The 4 cm drop from the MOT area imparts 4 mK of kinetic energy to the atomic cloud, while the trap depth in the ring is only 2.5 mK. Thus transfer of only 15% of azimuthal to transverse energy while traversing this bump would be enough to eject an atom from the trap in 2 revolutions. Also, we expect the lifetime to increase with current because this increases the trap depth, but does not change the geometry of the imperfection, nor the kinetic energy from the fall. This agrees well with the observations of Fig. 25.

3.5 Summary of Storage Ring Experiment

We have demonstrated a magnetic storage ring for neutral atoms, together with an efficient loading method. We learned that the steady state design used in the first generation experiment simply did not couple atoms into the ring. The new loading method involves a time-dependant potential that shifts the trap minimum from the guide to the ring. With this loading method, we can efficiently couple one million neutral atoms into the ring and observe numerous subsequent revolutions. Extensions of this work to ring-based atom interferometry and cold-beam generation hold much promise for the future.

We have also demonstrated that the ring can be multiply loaded by coupling a second atomic cloud into the ring 180 degrees out of phase with the first. Although the technique we used for this demonstration is limited to separated pulses, it is also possible to design potentials that allow continuous loading. These would have to include a time dependent state transfer (for example with a raman pulse to a trapped magnetic sublevel). Such potentials are necessarily 'bumpy' (otherwise it would be possible to increase phase space density, which would violate Louiville's theorem), however the additional entropy could be removed by subsequent laser cooling or evaporative cooling in the ring.

The azimuthal velocity distribution of the atoms in the ring has been manipulated by pulses of resonant light. The original azimuthal velocity distribution has a width $\Delta v \sim 2$ cm/s corresponding to a speed ratio $v/\Delta v \sim 50$ in the ring. After manipulation, this speed ratio has been increased to 125. This ratio is important for cold beam generation because it signifies a reduction in the relative velocity between particles.

Even with the 180 ms lifetime in the ring, it is noteworthy that the total guided distance is $\sim$0.5 m and if this system was used in a ring interferometer configuration, the enclosed area would be $\sim$2000 mm^2, 100-fold larger than the most sensitive atomic gyroscope demonstrated to-date [9]. Furthermore, with straightforward modifications to the ring discussed above, together with improved vacuum conditions, it should be possible to increase these values by another 100-fold (corresponding to a ring lifetime 20 s), yielding an intrinsic sensitivity 10^4 larger than in [9]. Of course maintaining atomic coherence over

these time scales is a significant technical challenge, and would most certainly require guiding in a single transverse mode. However, the ring geometry offers important advantages over single mode linear magnetic guides. In particular, by using complete revolutions of the ring for the interfering counterpropagating trajectories, we can ensure that each interfering amplitude acquires the same dynamical phase from the guiding potential (to the extent than the ring current and dimension remain constant), which will be important to cancel out effects of inevitable irregularities in the guiding potentials. This advantage, together with the recent demonstrations of fast, compact techniques for making atomic Bose condensates in optical [34] and magnetic microtraps [46] makes the prospects of single-mode guided atom interferometry quite promising.

3.5.1 Future Applications and Modifications

There are several areas of improvement for the ring experiment that could increase the lifetime and offer the possibility of coherent atom interferometry. A micro-fabricated ring with many smooth current sections could prevent the observed losses from our "bump" where the current is fed in and out. Also, single mode guiding would be made possible by transferring a BEC to the ring.

Bigger is not necessarily better and in the case of magnetic trapping and guiding it is most decidedly worse. The scaling of magnetic field gradients as described in section 2.2 points to smaller guiding geometries. Traps with wires that are lithographically etched onto the surface of semiconductor chips have been demonstrated [45, 43, 46]. These small guides need much less current than their larger counterparts to produce the same field gradients, and the heat generated by these currents is readily absorbed by the chip. The combination of lower vacuum emissions, steeper field gradients, and smoother guiding potentials could immediately increase the trapping lifetime of a storage ring.

Introduction of a BEC into a ring, either on a surface trap [46] or with an optical dipole trap [34] would greatly enhance the performance of a ring interferometer. One of the challenges facing all guided atom interferometers today is to find an intense single-mode source of atoms. Although it has been shown that multi-mode guiding is possible [26], it is

far less sensitive and the interfering fringes must be made to overlap at a common point, which places strict limits on the design geometry.

CHAPTER IV

QUANTUM COMPUTING WITH NEUTRAL
ATOM-CAVITY QED

The research presented in Part II of this thesis focuses on developing neutral atom cavity QED systems capable of storing and coherently manipulating quantum information coded in long lived ground states of neutral atoms. This requires the successful integration of two leading quantum information technologies—atom based quantum memories and cavity QED based entanglement generation and manipulation. Our configuration employs movable laser traps for individual atoms that will permit us to store a chain of individually addressable atoms and to manipulate these atoms in arbitrary combinations using the quantum field of the optical cavity. Here, we discuss the theoretical background and tools necessary to implement this configuration. First we give an introduction to quantum computing in section 4.1. Next, we look at aspects of cavity QED relevant to our experiment in section 4.2. We conclude with section 4.3, which includes theory behind optical dipole traps and motional manipulation of atoms in these traps. For information on the laser cooling used in this experiment, the reader is referred to the detailed discussion in chapter two.

4.1   Introduction

In order to appreciate and understand the power of quantum computing, it is illustrative to first compare classical and quantum information. Classical information is stored in discernable classical states of a system, such as the beads of an abacus, marks on a piece of paper, or the electronic state of a semi-conductor device. For calculation purposes, complex structures of information are divided into *bits* and processed more or less individually[1]1 in a classical computer. A *bit* is the smallest indivisible unit of classical information and

---

[1]Although most computers can process more than a single bit simultaneously (i.e. 32 or 64 bit systems), this parallel processing is limited by the architecture of the system and the physical resources scale linearly with the bitwidth.

represents the amount of information stored in a system that is in one of two possible configurations, which we shall refer to as $|\mathbf{0}\rangle$ and $|\mathbf{1}\rangle$. Quantum mechanical two-level systems, on the other hand, can be in a superposition of both the states $|\mathbf{0}\rangle$ and $|\mathbf{1}\rangle$ at the same time. More generally, the state of a two-level quantum system, known as a *qubit* is given by:

$$|\Psi\rangle = \alpha|\mathbf{0}\rangle + \beta|\mathbf{1}\rangle \tag{32}$$

where α and β are complex amplitude components. Such systems can be physically realized, for example, by the quantum state of a spin $1/2$ system, such as an electron, or two hyperfine ground states of a neutral atom. The state of two independent qubits can be represented by:

$$|\Psi\rangle_{1,2} = (\alpha_1|\mathbf{0}\rangle_1 + \beta_1|\mathbf{1}\rangle_1) \otimes (\alpha_2|\mathbf{0}\rangle_2 + \beta_2|\mathbf{1}\rangle_2) \tag{33}$$

However, this is not the most general state for 2 two-level systems. Quantum mechanics allows for entanglement of quantum systems, where the total system state is no longer given by the product of the individual states [71, 72]. Quantum systems that are entangled with one another cannot be considered as individual– their existence is only defined together with the other constituents of the total entangled state. An example of an entangled state is given by the (non-normalized) Bell state or EPR pair:

$$|\Psi\rangle_{1,2} = |\mathbf{0}\rangle_1 \otimes |\mathbf{0}\rangle_2 + |\mathbf{1}\rangle_1 \otimes |\mathbf{1}\rangle_2 \tag{34}$$

This state cannot be written as the product of any two individual states, and is thus entangled. For brevity, we shall write the product of two quantum states $|\mathbf{A}\rangle_1 \otimes |\mathbf{B}\rangle_2$ as $|\mathbf{AB}\rangle$, where the order determines which qubit is referred to. The general state of n qubits can be written as:

$$|\Psi\rangle_n = \sum_{i=1}^{2^n} c_i |i_b\rangle \tag{35}$$

59

Where i_b is the n-digit binary representation of the number i (for $n = 3$ $i_b = 5$ would correspond to $|101\rangle$), and the c_is are complex coefficients. Here, we begin to understand the power of quantum computation. A system of n qubits can store 2^n different bit values simultaneously because of the superposition principle. This exponential increase in storage offers a tremendous advantage over classical systems. For example, a system of only 300 qubits could simultaneously store more numbers than there are atoms in the entire universe! This increase in storage relies on the fact that we can create and manipulate entangled states of the system. Without entanglement, a quantum system can store no more information than its classical counterpart.

The enhancement in computational power of a quantum computer derives from the fact that a single manipulation (also called a *quantum logic gate*) performed on part of the total system can effect all 2^n stored values simultaneously, allowing massive numbers of calculations to be performed in parallel. However, putting this massive parallelism to good use is not as straightforward as it may seem. Any measurement of the whole system will project the state $|\Psi\rangle_n$ onto a single state, which contains only n bits of information. Furthermore, this projection is probabilistic in nature, with the probability proportional to the square of the amplitude of the measured state. In order to take advantage of a quantum computer, special algorithms must be developed that delay measurement until the end of a calculation, at which point the amplitude of the solution state is made much larger than all others. To date, there exist only a few quantum algorithms which can take advantage of the massive parallelism offered by quantum mechanics. In 1994, Shor developed the most famous of these algorithms [13] for taking discrete logarithms, a corollary of which provides for an exponential increase in the speed of number factorization. Since most of today's encryption relies on the presumed mathematical difficulty of factoring large numbers, the successful demonstration of a quantum computer would have a huge impact on data encryption and national security. Another algorithm, developed by Grover [14], allows for quick searching in an unordered database. Although it offers only a polynomial speedup over classical methods, this algorithm can be used to reduce the computation time of many tasks that require large amounts of conventional computing resources, such as

the traveling salesman problem and the telephone book lookup problem. This technique can also be used to break other, non-factorization based encryption more efficiently than classical computation.

Physical realization of a quantum computer is principally limited by *decoherence*, or loss of coherence in the complex amplitudes of $|\Psi\rangle_n$ [73]. Decoherence can occur during the individual quantum logic gates or simply while storing the quantum information during the calculation. Regardless of the decoherence mechanism, it is the ratio of the decoherence time (T_{dec}) to the gate operation time (T_{gate}) that sets the limit on the performance of any real quantum computer. Currently, there are groups pursuing the creation of a quantum computer in many different fields, including neutral atoms, cavity QED, trapped ions, quantum dots, super-conducting quantum interference devices (SQUIDS), and bulk nuclear magnetic resonance (NMR). Despite these endeavors, the state of the art in creation and manipulation of quantum information remains primitive. To date, only a few groups have succeeded in demonstrating a single gate operation [74, 75, 76]. This difficulty reflects one of the fundamental challenges in quantum computing—simultaneous attainment of reliable quantum information storage and controllable interactions. Many of the proposed schemes offer strong interactions and easy accessibility to the quantum information (quantum dots, SQUIDS) but are poor storers of quantum information due to decoherence. Others can store quantum information for long periods of time (neutral atoms, NMR) but have relatively weak interactions with other systems. This problem is fundamental in nature because the same mechanism that allows us to interact with a system to perform quantum gates will inevitably also allow the environment to interact with this system and cause decoherence.

An attractive solution to this problem lies in storing the quantum information in neutral atoms (a fine quantum memory) and using the spatially dependent interaction of a highly-coupled cavity mode to manipulate the states of these atoms. This interaction can be manipulated by controlling the cavity light field and thus promises a viable solution to the decoherence problem. Furthermore, the cavity can read out the quantum states of atoms in the form of "flying qubits" or photons, which are excellent transporters of quantum information and allow optical networking together with other quantum information systems.
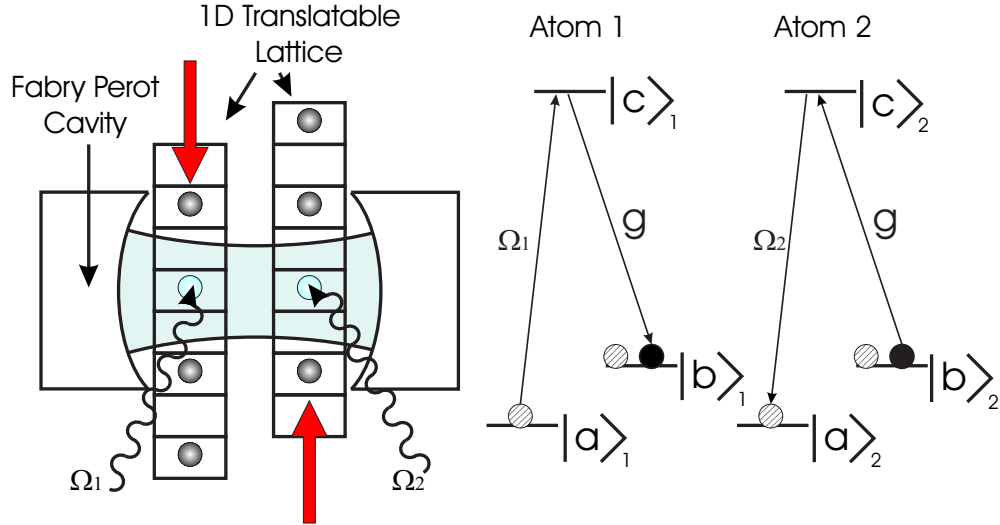
Figure 29: (Left): A schematic of our proposed quantum computing scheme. Atoms are trapped in an optical lattice and interact via the cavity mode. The two atoms in the mode are shown in light blue. (Right): An example of adiabatic state transfer from atom 1 to atom 2 via the optical cavity.

There have been spectacular recent successes in cavity QED research, including real-time observation [77, 78, 79] and trapping [80, 81, 82, 83] of single atoms inside the cavity, real-time feedback control on a single atom [84], and deterministic generation of single photons[85, 86]. Progress towards reliable quantum information manipulation in these cavity QED systems is principally limited by the inability of the system to provide adequate control over atomic motional degrees of freedom.

Our proposal [87] to overcome this limitation is to employ additional optical trapping fields perpendicular to the cavity mode for motional control of the atoms. The experimental concept, shown in Fig. 29 (Left), utilizes the long-lived hyperfine ground states of a neutral atom (^{87}Rb) to provide the required two-state qubit. The atoms are held in a dual translatable lattice potential provided by optical dipole traps running perpendicular to the cavity mode. Entanglement between two atoms is created by moving them into the cavity mode and implementing one of many possible theoretical entanglement proposals [88, 89, 90]. It is then possible to engineer any desired quantum gate using only this two-atom entanglement process. After the calculation has been performed, the quantum states of the atoms can be
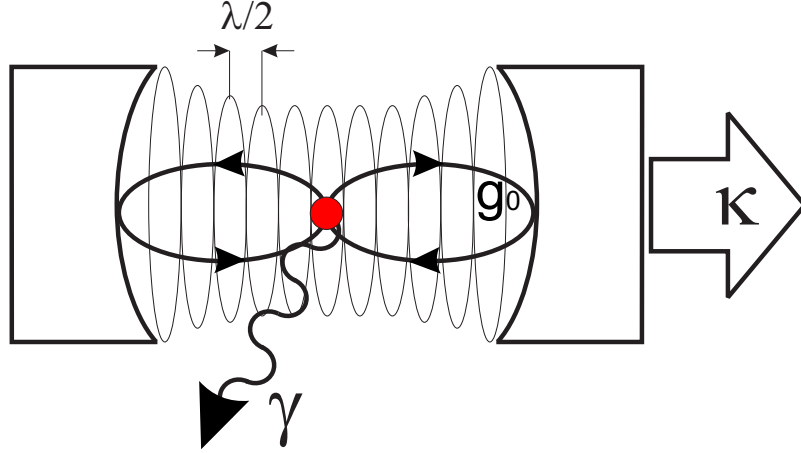
Figure 30: A schematic of an atom inside at optical cavity. The atom-cavity coupling rate (g_0) as well as the the cavity (κ) and the atomic (γ) decay rates are shown.

transferred to a cavity photon and measured in the output transmission from the cavity.

4.2   Cavity QED

At the heart of any cavity QED experiment is obviously the cavity. In our proposed quantum computer, the cavity enables us to entangle intra-cavity atoms and coherently exchange information between light and matter. In this section we shall derive some basic properties of cavity QED and give an example of how the cavity in our system might be used to coherently transfer a quantum state between two atoms.

We begin with a single atom coupled to the TEM_{00} mode of an optical cavity, as shown in Fig. 30. The coherent atom-field coupling rate is given by the product of the atomic dipole matric element p and the single photon electric field E.

$$g_0 = p \cdot E \tag{36}$$

We can calculate E by considering the integral of the energy density inside the resonator due to a single photon $\hbar\omega$:

$$\hbar\omega = \int \left(\frac{\varepsilon_0}{2}|\mathbf{E}|^2 + \frac{1}{2\mu_0}|\mathbf{B}|^2\right)dV = \int \varepsilon_0|\mathbf{E}|^2 dV = 2\varepsilon_0 E_0^2 V_m \tag{37}$$

63

Where E_0 is the magnitude of the electric field and V_m is the mode volume of the TEM$_{00}$ mode. Thus we obtain:

$$g_0 = p\sqrt{\frac{\hbar\omega}{2\varepsilon_0 V_m}} \tag{38}$$

An experimentally useful formula for g_0 can be found by replacing p using $\gamma = \frac{p^2}{3\pi\varepsilon_0\hbar\lambda^3}$ and substituting for the gaussian mode volume $V_m = \pi w_o^2 l/4$:

$$g_0 = \sqrt{\frac{3c\lambda^2\gamma}{2\pi^2 w_0^2 l}} \tag{39}$$

where λ is the wavelength of the atomic transition, w_0 is the $1/e^2$ intensity waist of the mode, l is the length of the cavity, and γ is the atomic decay rate. If we assume a symmetric cavity ($r_1 = r_2$) and that the radius of curvature of the mirrors is much larger than the length of the cavity (which is typically the case for strongly coupled systems) then we can approximate the expression for the cavity radius:

$$r = \frac{l}{2} + \frac{l^2\lambda}{4\pi w_0^2} \approx \frac{l^2\lambda}{4\pi w_0^2} \tag{40}$$

which further simplifies the expression for g_0 to:

$$g_0 = \sqrt{\frac{3c\lambda\gamma}{\pi\sqrt{2r l^3}}} \tag{41}$$

In general, g is dependent on the position of the atom inside the cavity with $g = g_0 E(\mathbf{r})/E_0$. In order to maintain a constant coupling rate, this position must be controlled very precisely. In particular, the position along the cavity axis must be controlled to within much better than $\lambda/2$, which is the node-spacing of the intra-cavity standing wave. We shall discuss the positioning of atoms in our experiment later in section 4.3.

In order to achieve coherent dynamics at the single photon level, the atom-cavity coupling (g) should be much faster than the spontaneous emission rate of the atom (γ) and the field decay rate of the cavity (κ). This condition is known as the strong coupling regime and

is achieved by using a small, extremely low loss cavity. While strong coupling is technically challenging, this limit has been achieved in ~ 10 labs over the past 15 years or so in both the microwave and optical domains (see [91, 92, 93, 94, 95] for recent overviews).

There are two dimensionless parameters that allow us to characterize an atom-cavity system. The first is the critical atom number $N_0 = \kappa\gamma/g_0^2$. This tells us how many atoms we must insert into the cavity to significantly change the atom-cavity response. A critical atom number below 1 means that the cavity's response is sensitive to single atoms. The inverse of the critical atom number is called the single atom cooperativity $C_1 = g_0^2/\kappa\gamma$. Similarly, we define the critical photon number[2] $n_0 = \gamma^2/8g_0^2$, which the number of intra-cavity photons producing an intensity inside the cavity equal to the saturation intensity of the atom.

Before discussing the atom-cavity theory, we should define some other quantities that help us better understand the cavity system. The longitudinal mode spacing is referred to as the *free spectral range* (FSR) of the cavity:

$$\text{FSR} = \frac{c}{2l} \tag{42}$$

For cavities with a very high reflectivity, like those used in our experiment, the cavity *finesse* is given by:

$$F = \frac{2\pi}{\text{Losses}} \tag{43}$$

where the "losses" are the total losses due to absorption and transmission of both mirrors combined (i.e. if each mirror transmitted 15 ppm and absorbed or scattered 5 ppm, the losses would be 40 ppm). The cavity decay rate, also called its half-width-half-max (HWHM) *linewidth* is related to the free spectral range by:

$$\kappa = \frac{\text{FSR}}{2F} \tag{44}$$

---

[2]This is sometimes defined in the literature as $n_0 = \gamma^2 b/4g_0^2$, where b is a geometrical factor corresponding to the electric field mode in the cavity. For the TEM_{00} mode considered here, $b = 8/3$.

For a symmetric cavity, with losses only due to transmission, we can write:

$$\kappa = \frac{cT}{4\pi l} \tag{45}$$

where T is the transmission of each mirror. With these definitions, we can understand how the strong coupling requirement affects the cavity selection process. Since γ is fixed, we must choose an r and l to make g_0 much larger than γ. Because of the weak scaling with r and difficulties with polishing mirrors with small r, which shall be discussed in more detail in Ch. 5, this is most often done by chosing a small l. Since $\kappa \propto 1/l$ we reduce the only free parameter left (T) until $g_0 >> \kappa$. As an example, let us take mirrors of curvature 10 cm. To achieve $g_0 >> \gamma$, we must choose $l << 500$ μm, so we chose, for example, $l = 50$ μm. This means that we must have $T \approx 8$ ppm. Thus, we require a mirror that can reflect 99.9992% of the light! The technology to produce these mirrors has existed for only the past ten years or so. A more detailed discussion about these mirrors will be presented in Ch. 5.

4.2.1 Ideal Atom-Cavity–Quantum Theory

If we can neglect the atomic and cavity decay rates, we can describe a single, stationary two-level atom inside a resonant cavity in the interaction picture by the Jaynes-Cummings Hamiltonian [96]:

$$H = \hbar\omega\hat{a}^\dagger\hat{a} + \frac{\hbar\omega}{2}\hat{\sigma}_z + \hbar g_0(\hat{a}\hat{\sigma}^\dagger + \hat{a}^\dagger\hat{\sigma}) \tag{46}$$

Where $(\hat{a}^\dagger, \hat{a})$ are the field creation and annihilation operators, $(\hat{\sigma}^\dagger, \hat{\sigma})$ are the atomic raising and lowering operators, and $\hat{\sigma}_z$ is the atomic inversion operator. Because the atom and the cavity are resonant, they both have frequency ω. This Hamiltonian has eigenstates:

$$|E_{\pm,n}\rangle = \frac{1}{\sqrt{2}}(|g, n\rangle \pm |e, n-1\rangle) \tag{47}$$

where g, e are the atomic ground and excited states, and n indicates the level of field excitation. The energy eigenvalues of these states correspond to:
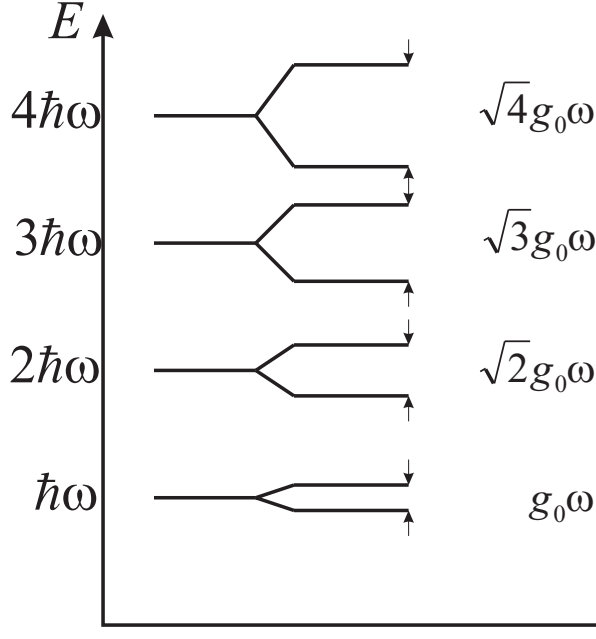
Figure 31: The Jaynes-Cummings ladder of eigenenergies in the ideal atom cavity system.

$$E_{\pm,n} = n\hbar\omega \pm \sqrt{n}\hbar g_0 \tag{48}$$

These eigenstates build what is known as the Jaynes-Cummings *ladder*, pictured in Fig. 31. Note that the eigenenergies are anharmonic and differ from the semiclassical predicted values of $E_{\pm,n} = n\hbar\omega \pm n\hbar g_0$. However, for $n = 1$ the two theories predict the same result and this anharmonicity is not observable.

In any real system with detuning between the atom and cavity resonance, the atom and cavity decay rates contribute to dissipation which can be described in the electric dipole and rotating wave approximations by a density matrix and master equation [97]:

$$\dot{\rho} = -\frac{i}{\hbar}\left[\hat{H}_0, \rho\right] + \frac{\gamma}{2}(2\hat{\sigma}\rho\hat{\sigma}^\dagger - \hat{\sigma}^\dagger\hat{\sigma}\rho - \rho\hat{\sigma}^\dagger\hat{\sigma}) + \kappa(2\hat{a}\rho\hat{a}^\dagger - \hat{a}^\dagger\hat{a}\rho - \rho\hat{a}^\dagger\hat{a}) \tag{49}$$

where

$$H_0 = \hbar\Delta_c\hat{a}^\dagger\hat{a} + \hbar\Delta_a\hat{\sigma}^\dagger\hat{\sigma} + \hbar g_0[\hat{a}\hat{\sigma}^\dagger + \hat{a}^\dagger\hat{\sigma}] + A(\hat{a} + \hat{a}^\dagger) \tag{50}$$

Here, A is an electric field driving the cavity (probe field) with frequency ω_p, Δ_c is the cavity-probe detuning $(\omega_c - \omega_p)$ and Δ_a is the atom-probe detuning $(\omega_a - \omega_p)$. A numerical
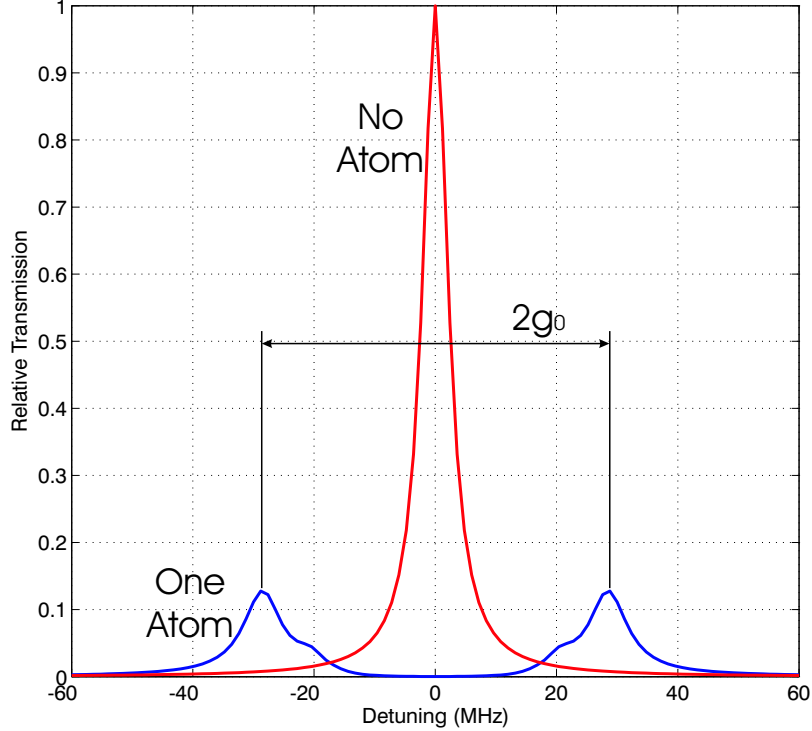
Figure 32: Relative cavity transmission versus atom-field detuning (Δ_a) for no atoms and one atom in the cavity. Here, the atom and cavity are resonant, the cavity drive strength is equivalent to 1 intra-cavity photon, and the cavity parameters are $[g_0, \kappa, \gamma] = 2\pi \times [27, 2.4, 6]$ MHz, identical to those used in the experiment. The atom splits the transmission peak into two, separated by twice the atom-cavity coupling g_0.

solution to this equation is shown in Fig. 32. Here we have plotted the relative cavity transmission for an empty cavity and a cavity with one atom. As the atom enters the cavity, it splits the transmission peak in two, separated by $2g_0$. If a single atom falls through the cavity with a resonant cavity probe, the drop in transmission will enable us to detect it. In order to observe this splitting, the atom-cavity must be strongly coupled. In Ch. 5 we present data showing a drop in the cavity transmission due to a single atom optically transported into the cavity.

4.2.2 Atom-Cavity, Semiclassical Treatment

In addition to single atom transits in the cavity, we also observe coupling of many atoms simultaneously into the cavity. In this case, a semi-classical approximation can be made, which consists of factoring the joint operators ($\langle \hat{a} \hat{\sigma}^\dagger \rangle \rightarrow \langle \hat{a} \rangle \langle \hat{\sigma}^\dagger \rangle$). In this case, we observe optical bistability [98], described by the following relationship between the output x and

input y field amplitudes of the cavity [99]:

$$Y = X \left[\left(1 + \frac{2C}{1 + \delta^2 + x^2} \right) + i \left(\phi - \frac{2C\delta}{1 + \delta^2 + x^2} \right) \right] \tag{51}$$

Here, $\delta = 2\Delta_c/\gamma, \phi = \Delta_c/\kappa, \,, C = NC_1$ is the N-atom cooperativity, and we have normalized the field amplitudes X, Y by the square root of the critical photon number $\sqrt{n_0}$. This equation predicts two stable output intensities for a single input intensity for certain (large) values of C.

4.3 Dipole Force Traps

A major limitation in many cavity QED systems is the inability to effectively manipulate the motion of neutral atoms inside the cavity. Since the electric, magnetic, and electromagnetic interactions with neutral atoms are so weak, it is indeed a challenge to accurately position them to very high precision within the mode of an optical cavity. One possibility for high precision confinement is offered by a translatable standing wave optical dipole force trap. This section describes the history and theory behind these traps and how they can be used for precision positional manipulation.

The first optical trap for neutral atoms was developed in 1986 by Chu *et al* [100], who exploited this force to confine atoms collected from an optical molasses. Since then, optical dipole force traps have found applications in many areas of research in ultracold atomic physics. Of particular interest to our research is the demonstration of deterministic delivery of a single atom trapped in an optical lattice [101].

Optical dipole force traps are based on the dispersive interaction between the electric field component of light $\mathbf{E}$ and the induced electric dipole of an atom $\mathbf{p}$. The energy of this interaction is proportional to the intensity of the light and if the light is tuned below the atomic resonance, it produces an attractive potential. A single focused laser beam offers the simplest example of a dipole trap because the atoms are attracted to the highest point of intensity, located at the focus. Because the light couples the atom's ground and excited states, some photons will be scattered by the atom. However, if the laser's frequency is far

away from the atomic resonance, the scattering rate can be substantially lowered, producing an essentially conservative trap.

One application of dipole force traps is in sub-micrometer positioning of atoms as demonstrated in [101]. Two counterpropagating laser beams can trap atoms at the anti-nodes of their standing wave potential. In this case, the atoms are localized to the individual wells of the lattice, which are spaced by $\lambda/2$, where λ is the wavelength of the trapping light. By shifting the frequency of one laser beam, these wells travel along the optical axis with a velocity proportional to the frequency shift. Controlling the frequency shift allows positioning of neutral atoms along the optical axis to within less than half an optical wavelength.

4.3.1 Trap Depth and Scattering Rate

An electric field $\mathbf{E}$ oscillating at ω will induce an electric dipole $\mathbf{p}$ in a neutral atom. The interaction energy is given by [102]:

$$U = -\frac{1}{2}\langle \mathbf{p} \cdot \mathbf{E} \rangle = -\frac{1}{2\varepsilon_0 c}\text{Re}(\alpha)I \tag{52}$$

Here $\alpha(\omega)$ is the complex polarizability of the atom and I is the intensity of the electric field. The factor of $1/2$ comes from the fact that this is an induced dipole and not a permanent one. The force on the dipole is given by the negative gradient of this potential and is thus conservative.

The power absorbed by the dipole and and re-emitted as radiation is:

$$P_{rad} = \langle \dot{\mathbf{p}} \cdot \mathbf{E} \rangle = \frac{\omega}{\varepsilon_0 c}\text{Im}(\alpha)I \tag{53}$$

The radiation term comes from the imaginary part of the polarizability, which describes the component of the dipole oscillation that is out of phase with the applied electric field. We know that this radiation is emitted as photons from the atom, each having an energy of $\hbar\omega$. This allows us to calculate the photon scattering rate from Eq. 53:

$$\Gamma_{sca} = \frac{P_{rad}}{\hbar\omega} = \frac{1}{\hbar\varepsilon_0 c}\text{Im}(\alpha)I \tag{54}$$

We have in Eq. 52 and 54 the two essential results for this derivation. However, they are expressed in terms of the atomic polarizability, which is frequency dependent. We can reexpress α using the simple Lorentzian model of a classic oscillator where an electron with mass m_e and charge e is bound to a nucleus of infinite mass by an ideal spring. This system has a resonance frequency ω_0 and is driven by an electric field oscillating at ω. The equation of motion for this system is:

$$\ddot{x} + \Gamma_\omega \dot{x} + \omega_a^2 x = -\frac{eE(t)}{m_e} \tag{55}$$

Since the driving force is periodic, we make the Ansatz $x = Ae^{Bt}$, which leads to the following result for α:

$$\alpha = \frac{e^2}{m_e} \frac{1}{\omega_0^2 - \omega^2 - i\omega\Gamma_\omega} \tag{56}$$

where

$$\Gamma_\omega = \frac{e^2 \omega^2}{6\pi\varepsilon_0 m_e c^3} \tag{57}$$

is the classical damping rate of an accelerated charge. (p. 665 of [103]). Substituting Eq. 57 into Eq. 56 gives us:

$$\alpha = 6\pi\varepsilon_0 c^3 \frac{\Gamma/\omega^2}{\omega_a^2 - \omega^2 - i(\omega^3/\omega_0^2)} \tag{58}$$

where we define Γ to be the damping rate for $\omega = \omega_0$. In the limit of low saturation, which is the case for all dipole force traps in this experiment, this classical expression agrees with that calculated in a semi-classical approach [102]. Substituting the result for α into Eq. 52 and Eq. 54 gives us useful expressions for the energy and scattering rate:

$$U = -\frac{3\pi c^2}{2\omega_0^3} \left(\frac{\Gamma}{\omega_0 - \omega} + \frac{\Gamma}{\omega_0 + \omega} \right) I(\mathbf{r}) \tag{59}$$

and

$$\Gamma_{sca} = \frac{3\pi c^2}{2\hbar\omega_0^3} \left(\frac{\omega}{\omega_0}\right)^3 \left(\frac{\Gamma}{\omega_0 - \omega} + \frac{\Gamma}{\omega_0 + \omega}\right)^2 I(\mathbf{r}) \qquad (60)$$

In our experiment, the difference between the frequency of the trapping laser and the atom's frequency $\Delta = \omega_0 - \omega$ is much larger than the linewidth of the atomic transition Γ but much smaller than ω. In this type of optical dipole trap (known as a far off-resonant trap (FORT)) we may neglect the second term in the parentheses in Eqs. 59 and 60:

$$U = -\frac{3\pi c^2}{2\omega_0^3} \left(\frac{\Gamma}{\Delta}\right) I(\mathbf{r}) \qquad (61)$$

$$\Gamma_{sca} = \frac{3\pi c^2}{2\hbar\omega_0^3} \left(\frac{\Gamma}{\Delta}\right)^2 I(\mathbf{r}) \qquad (62)$$

where $\Delta = \omega_0 - \omega$ is the detuning of the light with respect to the atomic resonance. These two quantities are related by:

$$\Gamma_{sca} = \frac{\Gamma}{\Delta}\frac{U}{\hbar} \qquad (63)$$

We see that for a given trap depth, larger detunings lead to the smallest scattering rates. This is important because the scattering rate presents a fundamental source of heating, as we shall see in Ch. 5. Also, for applications in quantum computing, the information stored in an atom will be lost if it scatters a photon.

We have considered the case that the atom has only two states. Real atoms have multiple levels that are simultaneously coupled by the light. Furthermore, the polarization of this light effects these coupling rates. In general we must sum over all contributing levels, taking into account the different oscillator strengths of each level. Fortunately, for the case of an alkali atom and linearly polarized light, the multiple level structure results in a simple modification [102] of the detunings of Eqs. 61 and 62:

$$U = -\frac{\Gamma\pi c^2}{2\omega_0^3} \left(\frac{2}{\Delta_2} + \frac{1}{\Delta_1}\right) I(\mathbf{r}) \qquad (64)$$

$$\Gamma_\omega = \frac{\Gamma^2 \pi c^2}{2\hbar\omega_0^3} \left(\frac{2}{\Delta_2^2} + \frac{1}{\Delta_1^2} \right) I(\mathbf{r}) \qquad (65)$$

where Δ_2 and Δ_1 are the relative detunings between the light and the D2 and D1 transitions in the atom (in Rb $\lambda_{D2} = 780$ nm, $\lambda_{D1} = 794$ nm).

These equations give us the trap depth U and scattering rate Γ_ω of an alkali atom in a linearly polarized FORT.

4.3.2 Atomic Positioning using Dipole Force Traps

The superposition of two plane waves of identical amplitude and polarization but traveling in opposite directions and with different frequencies $\omega_1 = \omega + \Delta\omega/2$ and $\omega_2 = \omega - \Delta\omega/2$ is given by:

$$\begin{aligned}
\mathbf{E} = \mathbf{E}_1 + \mathbf{E}_2 &= A\boldsymbol{\varepsilon}e^{i(kz-\omega t-\Delta\omega t/2)} + A\boldsymbol{\varepsilon}e^{i(-kz-\omega t+\Delta\omega t/2)} \\
&= A\boldsymbol{\varepsilon}e^{-i\omega t}\left(e^{(kz-\Delta\omega t/2)} + e^{-(kz-\Delta\omega/2)}\right) \\
&= 2A\boldsymbol{\varepsilon}e^{-i\omega t}cos(kz - \Delta\omega t/2) \qquad (66)
\end{aligned}$$

Where A is the complex amplitude of the field, $\boldsymbol{\varepsilon}$ is the unit polarization vector, and $k = 2\pi/\lambda$. It is understood that we take the real part of this expression to find the electric field. There are two important features of equation 66 that are relevant to our experiment. First, the amplitude of the resultant electric field is twice that of the component fields. This means that the intensity and the trap depth will be four times greater than with a single traveling wave. Second, the last term represents a standing wave that translates or "walks" along the z axis with velocity $v = \Delta\omega\lambda/(4\pi)$.

For the laser beams used in this experiment, which are described by a transverse gaussian profile, the derivation is exactly the same, with the transverse spatial information contained in the complex amplitude A. The time averaged intensity of a single traveling wave gaussian beam is:

$$I = \frac{2P}{\pi w(z)^2}e^{\frac{-2r^2}{w(z)^2}} \qquad (67)$$
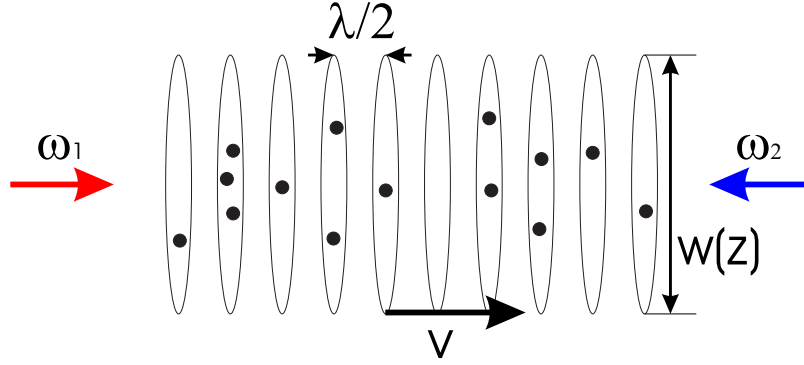
Figure 33: A schematic of the potential wells formed by two counterpropagating beams. The dark circles represent trapped atoms in the wells of the optical potential. The velocity is shown for $\omega_1 > \omega_2$.

where P is the power of the beam and $w(z)$ is its waist. For two counterpropagating beams, we have:

$$I = \frac{8P}{\pi w(z)^2} e^{\frac{-2r^2}{w(z)^2}} cos^2(kz - \Delta\omega t/2) \tag{68}$$

Combining this with equation 64 gives the trapping potential for the atoms:

$$U(r, z, t) = U_0 \frac{w_0^2}{w(z)^2} e^{\frac{-2r^2}{w(z)^2}} \cos^2(kz - \Delta\omega t/2). \tag{69}$$

Where U_0 is the trap depth at the focus ($z = 0$). This potential produces pancake shaped wells, which are $\sim \lambda/2$ thick and have a diameter of $\sim w(z)$ (see Fig. 33).

74

CHAPTER V

CAVITY QED EXPERIMENT

This chapter is based on the experiment described in:

J.A. Sauer, K.M. Fortier, M.S. Chang, C.D. Hamley, and M.S. Chapman. "Cavity QED with optically transported atoms." *Physical Review A*, **69**(27):051804,2004

5.1 Introduction

As a first step towards reaching a system capable of quantum information processing, we have constructed a cavity QED experiment featuring precise positioning of atoms within the cavity. This experiment shares only the MOT laser system, previously described in Ch. 3. Ultimately we decided on the experimental setup shown in Fig. 34. Here, a single vertical optical lattice would overlap with the MOT and the cavity mode. After loading the lattice, we translate the atoms into the cavity and monitor their arrival on the cavity transmission.

5.2 Experimental Apparatus

In this section, we discuss the experimental apparatus of the cavity QED experiment. This experiment shares a common MOT laser system with the storage ring experiment previously described in chapter 2. We first briefly introduce the different lasers used to make the optical lattice, deferring a detailed description of each system until chapter six. This is followed by a discussion of lattice control, alignment, and atomic positioning. We then shift our focus to the cavity, where we will discuss its construction and control. Finally an overview of the probing and detection systems is given.

5.2.1 FORT Lasers and Lattice Control

Three different laser systems were used at various times in the cavity QED experiment to form dipole force traps. A free running laser diode at 783.5 nm and 784.7 nm produced

MOT

Optical Lattice

Detector
Or Heterodyne Setup

Probe Beam

Cavity Mirrors

PZT
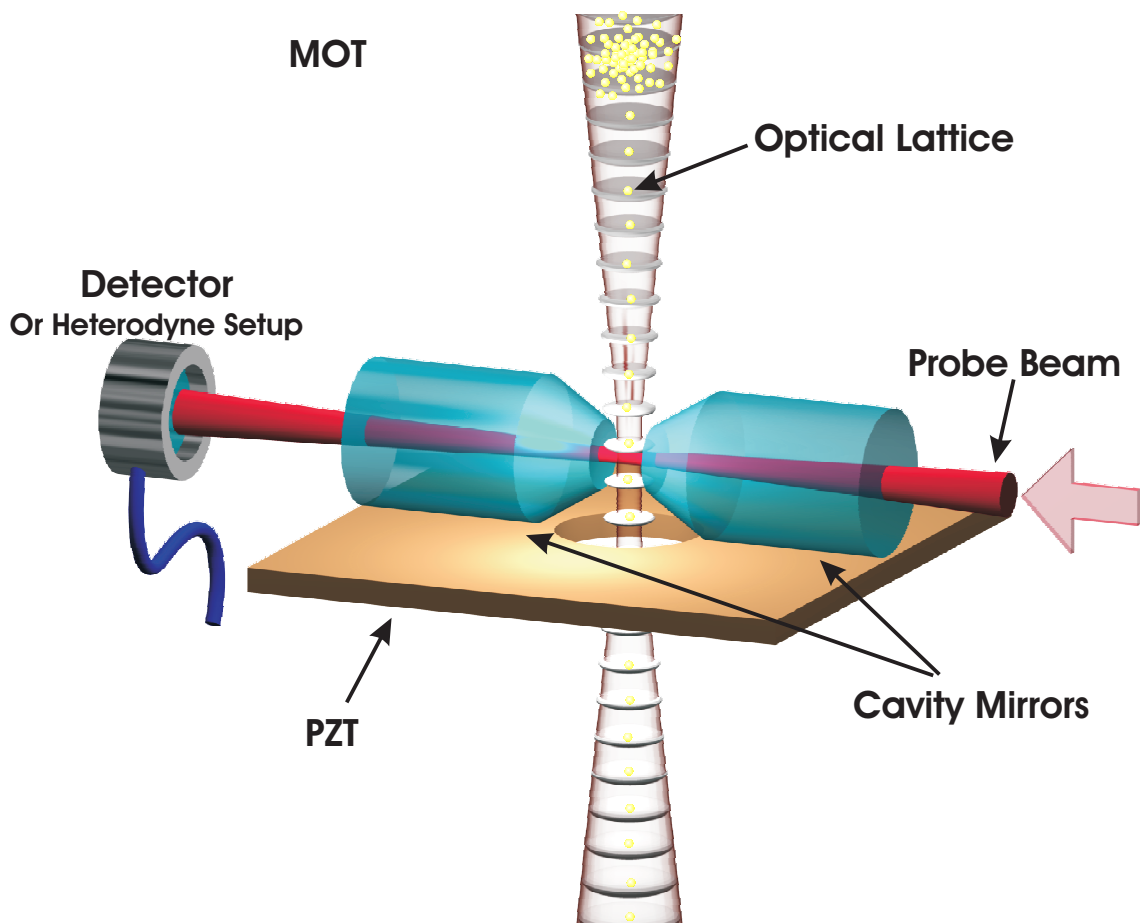
Figure 34: A simplified schematic of the QED experiment. Two counterpropagating laser beams form an optical lattice. Atoms are transported via this lattice into the high-finesse mode of an optical cavity, by shifting the frequency of one laser beam. The atom-cavity system is analyzed with a resonant probe beam that is detected in a heterodyning setup.

the first observable FORT in the cavity chamber. Later we moved to a more powerful Ti:Sapphire at 850 nm pumped by an argon-ion and a solid state Verdi, both from Coherent. Most recently we have employed two tapered amplifier systems, seeded by a single extended-cavity diode laser. We defer a detailed description of each system until Ch. 6, where we also discuss their performance in motional manipulation.

In order to create a controllable standing wave, the lattice beams require a phase coherent frequency shift. Two HP signal generators linked via their 10 MHz reference provide phase coherent radio frequency (RF) signals at frequencies ω_1 and ω_2. The frequency ω_1 remains at 80 MHz while ω_2 is modulated about 80 MHz via an external DC-coupled frequency control. The RF signals are then amplified and used to drive two identical AOMs. This modulation, controlled via Labview and our computer system, can produce a frequency difference of 10 MHz that can be modulated at 100 kHz. Since the RF frequency is added to the optical frequency in the AOMs, the difference optical frequency in the lattice is simply the applied modulation.

The accuracy of the phase coherent frequency shift is measured by mixing the two RF signals and recording the beat note. We observe that for frequency deviations less than 500 kHz this technique allows lossless atomic positioning, but for larger frequencies the voltage noise from the computer causes a fast jitter of this frequency that can lead to loss of atoms, as observed in [104].

5.2.2 FORT Loading and Alignment

A FORT can be loaded from a MOT simply by switching on FORT light after performing sub-doppler cooling. The dipole potential then confines those atoms with sufficiently small kinetic energy in the overlap region between the FORT and MOT. However, optimization of the loading number and temperature requires special loading parameters and precise alignment. In this experiment, the low FORT beam power produces a relatively shallow optical potential (on the order of $\sim 100~\mu$K). Also, the relatively small FORT beam waist of 30 μm further reduces the coupling efficiency of atoms into the FORT.

Alignment of the FORT beam with respect to the MOT is made much simpler if the

FORT wavelength is close enough to the atomic resonant wavelength, such that both can propagate in the same single mode optical fiber. The resonant light will perturb the MOT when correctly overlapped, allowing real-time feedback of FORT position by observing the MOT on a CCD camera. Once aligned, the FORT will usually trap an observable number of atoms simply by abruptly switching the MOT light off while the FORT light is left on, even if no special loading or cooling procedure is used.

A very detailed description of the loading dynamics in dipole force traps can be found in [105]; here we give the details of our transfer process. Initially the FORT light is off, and the MOT is loaded from the background vapor. At time $t = 0$ we lower the repump light intensity to 3 μW/cm^2, while turning on the FORT beam. The detuning of the trapping light is shifted from 15 MHz to 100 MHz below resonance 20 ms later. At $t = 59$ ms, the repump light is shuttered off, which pumps the atoms entirely into the $F = 1$ state[1]. Finally at 60 ms, the MOT beams are ramped off over 1 ms, then shuttered and the magnetic field is turned off. This transfers a portion of the atoms in the MOT to the FORT.

Great care must be taken to align the FORT lattice beams with one another as this is an interferometrically sensitive process. Along with extremely rigid mirror mounts and lens holders, the overlap of the lattice beams in all three dimensions (including along the optical axis) is necessary for secure atomic transportation. A rough alignment of the system can be made by maximizing the number of atoms trapped in the lattice. However, this process is only useful if the lattice is either vertical or the MOT is not located at the foci of the lattice beams. Otherwise, atoms trapped in the lattice will overlap with atoms trapped in one of the traveling wave potentials. The second alignment is done by translating the atoms back and forth over a large distance and observing losses throughout this process. Optimum alignment is achieved when these losses are minimized. It is possible that during this process, the number of atoms coupled into the FORT is decreased because the alignment with the MOT is no longer optimal. However, this is not a serious concern because our

---

[1]This technique differs from the sub-doppler cooling process described in 3.3.2. In particular, the temperatures reached with this technique are actually higher ($15 - 20$ μK), which loads fewer atoms into the FORT than the first technique. However this is the only way we can make the transfer and still pump the atoms into the $F = 1$ state. If this is not done, we observe a decrease in maximum lifetime to < 1 s, possibly due to ground-excited state collisions.

ultimate goal is to transport single atoms.

We note that because our cavity defines the correct position of our FORT beams, we must instead align the MOT with the FORT. This is usually done in a straight forward manner by moving the MOT coils, which translates the atomic cloud by moving the B-field zero. However, this process can move the center of the MOT away from the location zeroed by the trim cois. This can lead to a perturbation of the sub-doppler cooling. In this case, simply monitoring the FORT signal is not sufficient, as the number of atoms loaded is affected by both the position and the cooling of the cloud. We find therefore that one must iterate the alignment process several times, minimizing the temperature each time, to achieve maximum loading into the FORT.

5.2.3 Cavity Construction

There are several design considerations that enter into the selection of the cavity parameters r, l, and T. As is often the case in experimental physics, we must make a compromise in our selection of these parameters because of various constraints of the system. We would like the cavity to be in the strong coupling regime, which is characterized by an atom-cavity coupling rate g_0 that is much greater than the loss mechanisms from the cavity (κ) and the atom (γ). Recall from Ch. 4 that $g_0 \propto l^{-3/4} r^{-1/4}$ for cavities with radius much greater than their length. We can increase g_0 by making the cavity shorter or by choosing mirrors of a smaller radius of curvature. However, the scaling with the radius is weak, and the currently available selection of radii is limited for the highly polished mirrors used in our experiment. Furthermore, it is much more difficult to clean the mirrors with a small radius. For this reason, we choose a mirror radius of 10 cm, which is easy to clean and allows strong coupling for lengths of $\sim 100~\mu$m. The length ($l = 75~\mu$m) was chosen to be as small as possible while still allowing transmission of a 30 μm FORT beam. The transmission of the mirrors only affects κ and not g_0. We chose mirrors with the lowest available transmission of $T = 8$ ppm to decrease $\kappa \propto T$ and maximize the single atom cooperativity parameter $C_1 = g_0^2/\kappa\gamma$.

With this selection, we expect cavity parameters:

$$\kappa = 2\pi \cdot 2.5 \cdot 10^6 \text{ rad/s}$$

$$F = 400,000$$

$$g_0 = 2\pi \cdot 27 \cdot 10^6 \text{ rad/s}$$

$$C_1 = 48$$

$$N_0 = 0.01$$

$$\text{(70)}$$

These values of C_1 and N_0 easily allow observation of single atoms with single intra-cavity photons. This value of κ also places less of a demand on the linewidth of the laser used to excite the cavity, because the ECDLs in our lab typically have a linewidth of 1 MHz.

5.2.3.1 Mirrors and Cleaning

The mirrors used in this experiment were manufactured by REO in Boulder, CO and are similar to those described in [106]. They are fabricated on a 7.75 mm diameter BK-7 glass substrate, which is super-polished into plano-concave form with a surface sphericity of much better than $\lambda/10$ at 780 nm and a surface microroughness less than 0.1 nm [106]. An ion-beam sputtering process produces a mirror transmission of 6-8 ppm over a $\sim$30 nm range in wavelength.

The substrate diameter is machined down to 3 mm by REO at $45°$ leaving a 1 mm diameter surface as shown in Fig. 35. This allows for closer positioning of the mirrors around the expanding FORT laser beam. It also allows greater optical access for other beams in the cavity (i.e. Raman beams, repumps beams, diagnostic beams).

Christina Hood gives an excellent and in-depth discussion on the technical aspects of these mirrors and their cleaning in her doctoral thesis [97]. However, cleaning these small mirrors is found to be an exceptionally difficult task [107], often resulting in damage of the expensive coating. Here we detail the particulars of our cleaning process, which has been moderately successful.

As mentioned in [97], there are two mirror requirements for constructing a high-finesse
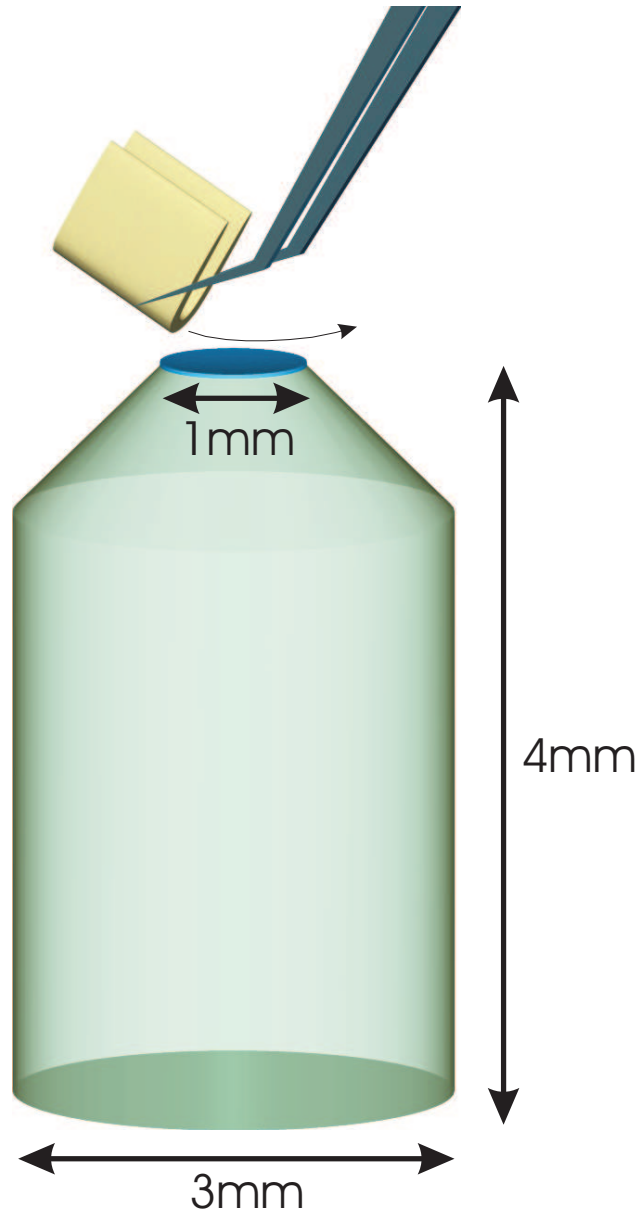
Figure 35: Cleaning of the mirror surface. Tweezers hold a folded piece of lens cleaning paper, folded into a "U" pattern. The swipe must contact the mirror inside and smoothly follow the radius of curvature for proper cleaning.

optical cavity: The mirrors must be free of defects and they must be clean. Unfortunately they can arrive from REO with either or both of these requirements unfulfilled. We inspect the mirrors with a dark-field microscope at a magnification of 500x. They are deemed clean and unblemished when no observable features are present at this magnification. Although the mirrored surface is 1 mm in diameter, it is sufficient to inspect only the central 250 μm, because even a hard aperture at this diameter would lead to negligible phase shift and loss in the cavity [64]. However, we inspect the central 500 μm to allow room for positioning and alignment of the mirrors. We also arrange a CCD camera to view the mirror surface as we clean it. This allows a more accurate positioning of the cleaning tissue and a first order observation of debris on the surface.

There are a set of mirror cleaning tools used in our laboratory, which are kept clean and are not used for any other tasks. The set consists of a large bag of lens cleaning tissue (Thorlabs), methanol with water content < 0.01%, powderless and lint-free gloves, a fine pair of tweezers, and a rubber mirror holder that has a small hole which grips the substrate and holds it upright during the cleaning process. Cleaning is done in a "clean" hood, which is constructed of plexiglass and has forced, filtered air introduced at the top. Each cleaning tissue is cut into 8 pieces. The gloves are selected to be as tight fitting as possible, while still allowing for free movement. The rubber is used to hold the mirror and also to move it between the camera and the microscope. This is invaluable as the number of swipes required to clean a single mirror can be between 10 and 100.

To clean a mirror, we fold a small piece of lens tissue several times until its thickness matches about 80% of the mirror's diameter. The "U" made from the last crease in the tissue is used to swipe the mirror. After the tissue is inserted into the tweezers, a drop of methanol is applied to the tip. While viewing the surface of the mirror on the video screen, we bring the tissue to contact the mirror just inside the edge and swipe along the surface with light to medium pressure matching the curvature of the mirror. This swipe must be done in one fluid motion and if any doubt exists, it's always better to swipe with less pressure and more methanol to avoid damaging the mirror. As mentioned above, the first inspection can occur on the video screen. If there are any glass pieces, tissue debris,

or other large particles on the surface of the mirror they can be seen with the CCD camera if properly lit. If no debris is observable, inspection with the microscope can proceed.

The mirrors can be scratched by glass fragments on the edge of the substrate. It is therefore very important that each tissue be used only ONE TIME to swipe the mirror. Even the lens tissue can scratch the surface if there is not enough methanol. However, too much methanol will simply leave residue on the surface of the mirror, which must be removed. A scratch is evident through its asymmetry (it is not a gaussian spot) and its size (hopefully very small). Some streaks appear to be scratches, so it is important not to discard a mirror until the scratch has been verified. Mirrors with smaller radii of curvature (5 cm, 2.5 cm) are exceptionally hard to clean due to the extreme concavity. Sometimes it is possible to angle the tissue to slightly prevent micro-droplets from scattering around and landing on this surface.

We typically find that given ten mirrors from REO, three cannot be used because of surface defects from the factory, three will be scratched by us during the cleaning process, two will be clean but have some blemish or defect we can live with (i.e. outside a central radius) and two will be flawless. The latter two are typically chosen for the cavity, while the other two are made into a test cavity, or set aside for future use.

5.2.3.2 Cavity Alignment and Construction

A schematic of the cavity alignment and construction is shown in Fig. 36. After we clean the mirrors, they are placed in a V-mount and secured by a 0-80 set screw with a rubber tip. Each V-mount is fastened to a 5-axis translation stage that can translate the mirrors in three dimensions and tilt in two (rotation about the cavity's symmetry axis is superfluous). On one translational axis of the stage, we place a PZT stack for micropositioning of the cavity mirror during a trial run. We shall refer to this axis, which is parallel to the cavity's optical axis, as $\mathbf{z}$. A laser beam waist $w_0 = 22$ μm, matching the cavity's waist, is focused in the alignment area and the far cavity mirror is translated until this beam is centered on the mirror. If the mirror is translated in the $\mathbf{x}$ or $\mathbf{y}$ directions, the beam can be centered by noting when the laser scatters on the edge of the mirrored surface. Then the mirror
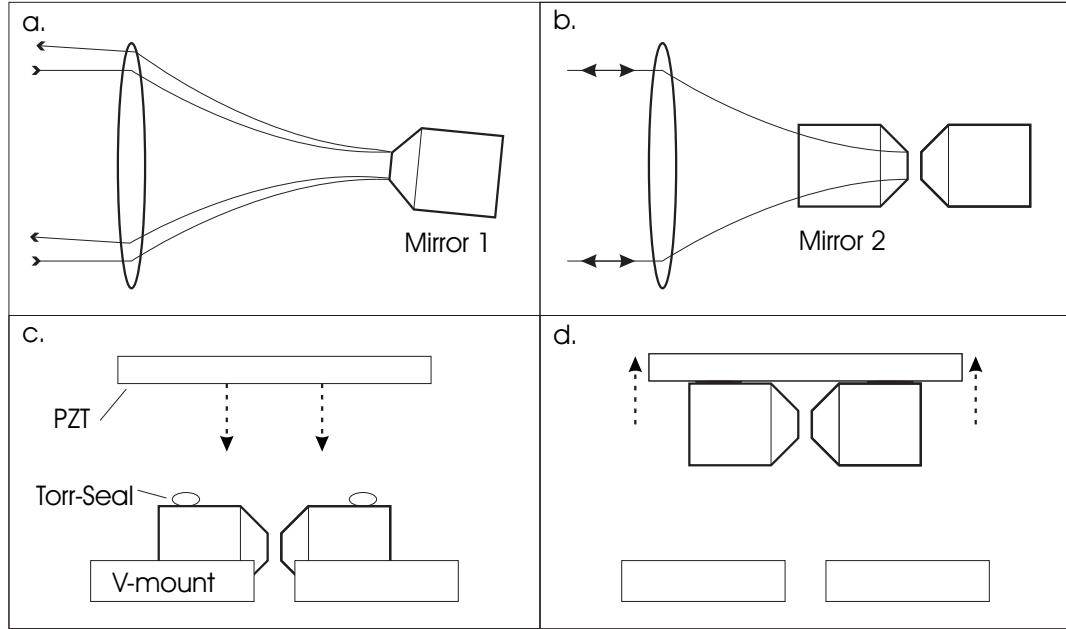
Figure 36: A schematic of the cavity alignment and construction process. a.) The first mirror is positioned such that the back-reflected beam travels along the same path. b.) The second mirror is positioned in the same fashion, and the length is set between mirrors. c.) Torr-Seal is applied to both mirrors while secured in the V-mounts and the PZT is lowered until it contacts the adhesive. d.) After the drying process, the set screws on the V-mounts are released and the finished cavity is lifted away from the jig.

is tilted until the reflected beam travels exactly back upon itself. Since this process also translates the mirror, we must iterate angular alignment and positioning to achieve proper placement. Positioning along the z-axis can be achieved by monitoring the spot size of the reflected beam. If the z position is not correct, this size will be different than that of the incoming beam.

The near mirror is aligned in an identical fashion. Here we must be careful not to allow the two to touch as they could become scratched or dirty. Once the second mirror is properly aligned, we set the length of the cavity by observing the separation on a 100x microscope. This microscope is first calibrated and then positioned so we can adjust the length with the translation stage in real time. After the length is set, we check the mirror alignment one final time before gluing the cavity together. As this point we can make a preliminary test of our cavity by applying a scanning voltage to the PZT stack on the translation stage. If the cavity is aligned correctly, and isolated from vibrations (done by hanging a breadboard
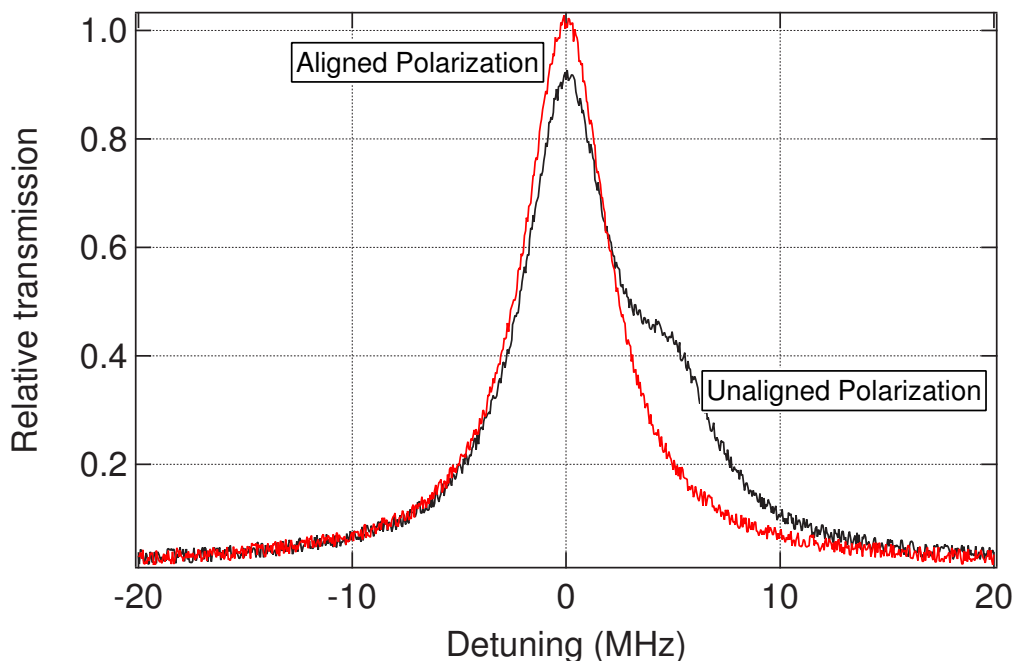
Figure 37: Transmission through cavity. Birefringence is observed if the polarization of the light is not aligned with the fast or slow cavity axis.

with bungee cords from the ceiling) we will observe cavity modes in the transmission of the cavity. A good cavity alignment corresponds to the dominance of the TEM_{00} mode over all others.

A trace of the cavity transmission is shown in Fig. 37. This image shows transmission of light through the cavity TEM_{00} as the length of the cavity is changed. The asymmetry of the transmission is caused by a slight birefringence of the cavity, which shifts the resonance frequency depending on polarization. In the experiment, we use only linearly polarized light rotate to either the fast or slow axis in the cavity. This eliminates the observed asymmetry from the cavity transmission. The birefringence is probably induced by the stress placed on the mirrors in the mounting process.

After testing, small drops of Torr-Seal low vapor pressure epoxy are applied to the top side of each mirror. We apply only as much epoxy as needed to avoid stress induced birefringence [97] of the cavity. A third translation stage holds a rectangular PZT above the cavity. This PZT is 13 mm x 13 mm x 1.3 mm, and made of lead zirconate titanate (5600 Navy V from Channel Industries). We lower the PZT until it contacts the epoxy, but
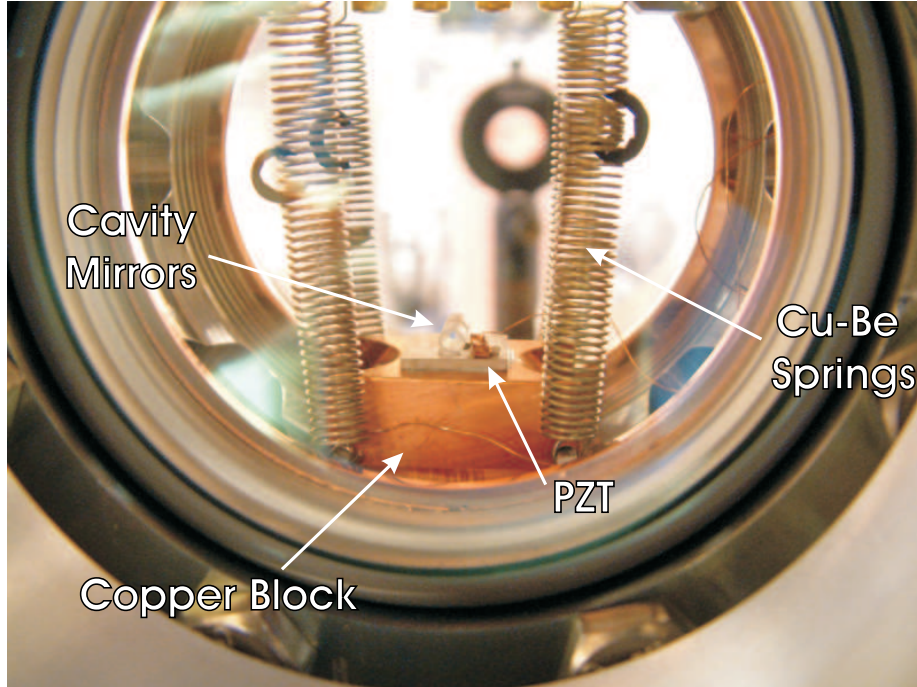
Figure 38: An image of the cavity mount inside the vacuum chamber.

not the mirrors. The epoxy is allowed to dry for a period of at least 4 hours after which we remove the set screws and hoist the new cavity from its V-mounts.

Prior to gluing of the cavity mirrors, we solder a very thin wire to the top of the PZT for voltage control. We use a very small amount of flux-free silver solder to avoid vacuum problems. The cavity is then adhered to a copper mount (Fig. 38) with electrically conductive UHV epoxy (Epotek H21D). This mount is suspended with 4 Cu-Be springs from the top of the cavity vacuum chamber. Cu-Be (98% Cu and 2% Be, ire diameter: 0.017", turns / inch: 20, Spring diameter: 0.255") is non-magnetic and offers the same elasticity of copper with a much higher strength, making it an ideal spring material. In a first iteration, we used slightly magnetic stainless steel (302 ANSI), which affected the MOT and shook the cavity mount when the MOT coils were turned on and off.

Good mechanical isolation requires a combination of a low-frequency suspension system for the mount and a rigid cavity structure with high-frequency mechanical resonances. The first order resonance frequency of a suspension system with a mass m and spring constant k is given by:
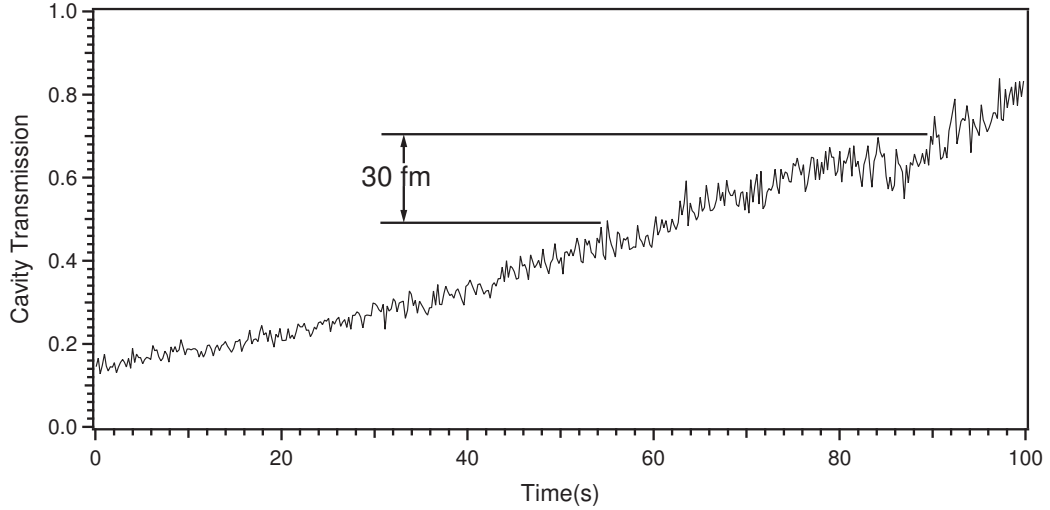
Figure 39: Passive cavity stability is shown in transmission over 100 s. The cavity length drifts less than 1 fm/s!

$$\omega_{res} = \sqrt{\frac{k}{m}} \tag{71}$$

However, the limiting factor in creating many cavity suspension systems is not the mass or spring constants, but the available space. As larger masses are combined with weaker springs, the extension of the springs requires a large distance. A simple calculation shows that this frequency is determined only by the extension distance of the springs:

$$\omega_{res} = \sqrt{\frac{g}{\Delta l}} \tag{72}$$

Thus the 2 cm extension in our cavity mount gives us a mechanical resonance of $\omega_{res} = 2\pi \cdot 3.5$ Hz.

To the best of our knowledge, our passive cavity stability is unmatched in performance among high-finesse micro-cavities. Fig. 39 shows a plot of cavity transmission versus time. For this data, the cavity is tuned on resonance with our stable voltage source (see Sec. 5.2.4.2 but no feedback is applied to the system. We excite the cavity with only 100 pW to avoid thermal self-locking [108, 109, 110] of the cavity, a process that would skew the results of this measurement.

5.2.4 Cavity Length Control

We must actively lock the cavity length for long term stability and also to avoid thermal fluctuations when the FORT laser beam is passed through. Many cavity QED experiments employ either a "chop-lock" technique [78, 111] or a dual beam reference cavity technique [84, 83] for this task. In a chop-lock, a strong locking signal is alternated with a weak probe beam, locking the cavity during the chop phase and allowing it to drift freely during the probe phase. The quality of this lock is determined by the duration of the probe phase. As observed in Fig. 39, our cavity could be unlocked over a very long time of 10 s or more, if unperturbed. However, when the FORT laser is shone through the two mirrors, absorption of this beam leads to strong thermal fluctuations that prohibit such long unlocking phases. Nevertheless, we can still perform experiments of duration 100-200 ms without significant cavity drift by using a modified chop-lock technique.

Alternatively, one can lock the cavity using a second beam of light that is any integer number of FSR's detuned from the resonance frequency [83, 84]. This light need not effect the atoms if it is made weak enough and at a large detuning. The frequency of this second beam must be stabilized to the resonant light by using an additional reference cavity. This is used by other groups and we are currently developing this technique for future experiments. However, the complexity of such a lock was unnecessary for the experiments in this thesis.

We present the technical details of our locking system over the next few pages, along with performance data and design considerations. Section 5.2.4.1 introduces expressions for cavity transmission as a function of length and shows the ultra-high sensitivity of our cavity. We then discuss length control via a PZT and the voltage stability required in an electronic control circuit. In section 5.2.4.2, the electronic control system is detailed with particular attention paid to the battery box and its transfer function. Finally we discuss how the lock is engaged, and report on the performance of the locking system in section 5.2.4.3.

The transmission through an optical cavity is given by [112]:

$$\frac{I_{trans}}{I_{inc}} = \frac{1}{1 + (2F/\pi)^2 \sin^2(\pi\omega/FSR)} \tag{73}$$

Here $F=2\pi/$losses is the finesse of the cavity, I_{trans} and I_{inc} are the transmitted and incident intensities, and $FSR=c/2l$ is the free spectral range of the cavity. When locking the cavity, we are interested in regions close to resonance where the argument of the sine is small. Thus we may approximate:

$$\frac{I_{trans}}{I_{inc}} = \frac{1}{1 + \frac{(\omega-\omega_0)^2}{\kappa^2}} \tag{74}$$

One can easily verify that κ is the half-width-half-max (HWHM) linewidth of the cavity and ω_0 is a resonance frequency. Here, κ is given by $\frac{FSR}{2F}$. For a single cavity mode, we may express the resonance frequency in terms of the cavity length as

$$\omega_0 = ck = \frac{c2\pi}{\lambda} = \frac{c\pi n}{l} \tag{75}$$

Where n is the longitudinal order of the cavity mode. Thus for a small change in length Δl of the cavity, the corresponding change in frequency $\Delta\omega_0$ is:

$$\Delta\omega_0 = \frac{-\Delta l}{l}\omega_0 \tag{76}$$

Inserting this into equation 74 gives the cavity transmission as a function of length:

$$\frac{I_{trans}}{I_{inc}} = \frac{1}{1 + (\frac{\omega_0\Delta l}{\kappa l})^2} \tag{77}$$

Where Δl is the length deviation from the resonance length l_0, corresponding to the resonance frequency ω_0 Alternatively, we may express the linewidth of the cavity in terms of a length adjustment. This gives us the "length" of the cavity's linewidth:

$$\Delta l_\kappa = \kappa\frac{\Delta l}{\Delta\omega_0} = \frac{1}{2\pi}\frac{\lambda}{4F} \tag{78}$$

If we wish to stabilize the length of our cavity to less than 1/10th of its linewidth, we must stabilize the mirror separation to $\sim 7 \cdot 10^{-15}$ m!

We actively lock the cavity on resonance by directly monitoring the cavity transmission and adjusting the voltage across the cavity PZT to stabilize this transmission. The fractional change in the transverse length mode of a PZT is given by [113]:

$$\Delta l = \frac{d_{31}l}{t}V \tag{79}$$

Where d_{31} is the piezo electric constant of our crystal ($225 \cdot 10^{-12}$ m/V), l is the length of the active area of the PZT (for us this corresponds to 5 mm, the gluing separation between the mirrors), t is the thickness of the PZT given above, and V is the applied voltage. This gives a calculated $\lambda/2$ voltage of $\sim$450 V at 780 nm. However, we measure this value to be 1250 V possibly due to adhering of the PZT to the copper block. The measured $\lambda/2$ voltage translates to a voltage stability requirement of 23 μV to maintain the cavity on resonance. Since we must be able to tune the length over $\lambda/2$ to bring the cavity on resonance, this means our cavity electronics must have eight digits of precision. We will discuss this device in the next section.

5.2.4.2   Control Electronics

A schematic of the control setup is shown in Fig. 40. The basic idea is that we detect the cavity transmission peak and apply a DC-offset such that the zero point corresponds to the side of this peak. An error signal is derived, manipulated, and returned to the PZT via control electronics. This "side-locking" technique is more simple than an FM technique like the Pound-Drever-Hall method [114, 115], but leads to a offset in the cavity resonance frequency.

Light from the cavity is detected in a heterodyne setup described in section 5.2.5. An RF spectrum analyzer then detects the beat note introduced by heterodyning with zero span at a bandwidth of 100 kHz. The video-out signal from the spectrum analyzer is split and sent to the data collection computer and an SRS pre-amp where it is amplified 10 dB and filtered with a 12 dB/Oct low pass filter at 10 kHz. A DC-offset adjusts the output of the pre-amp such that the zero crossing occurs on the side of the cavity transmission peak. This produces an appropriate error signal for side-locking the cavity.
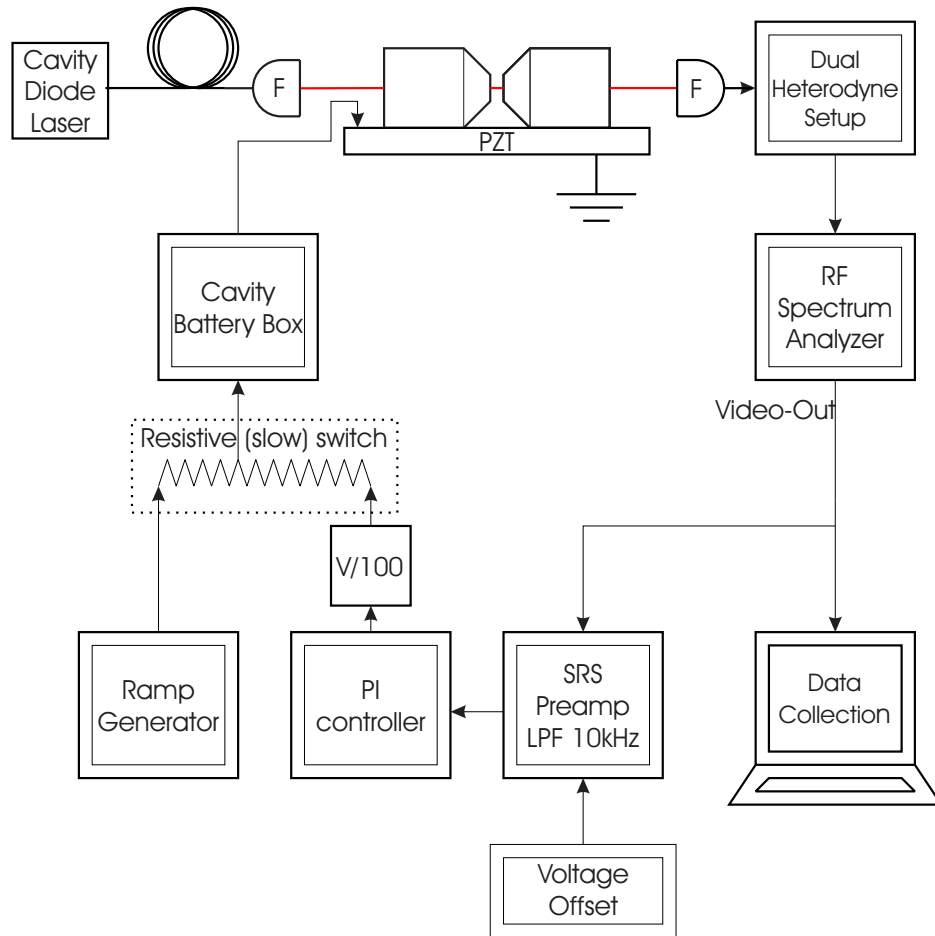
Figure 40: Simplified version of the cavity locking electronics setup. F-SMPM optical fiber.
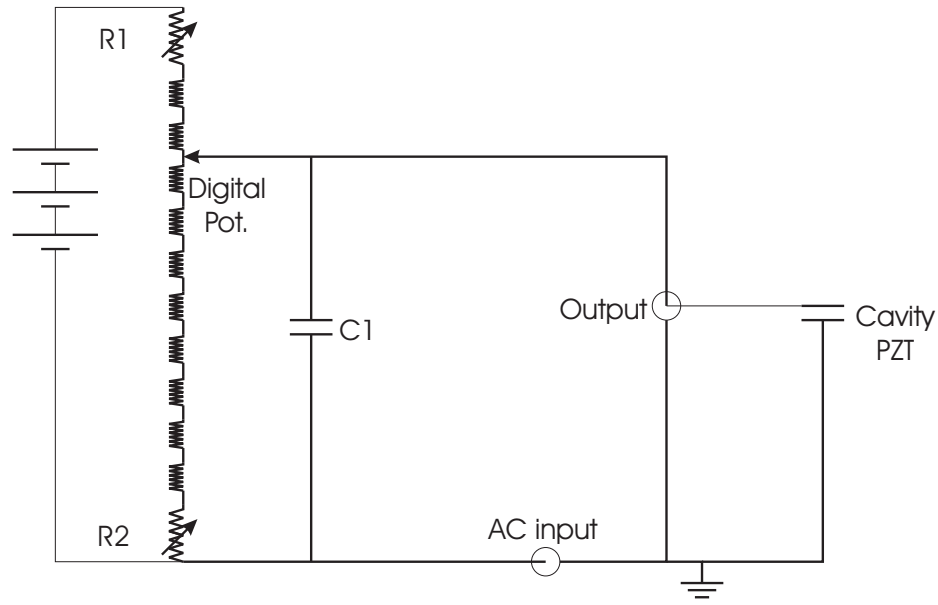
Figure 41: Battery box used to drive the cavity PZT. A "digital" potentiometer, fashioned out of a 10 way switch and ten 1 MΩ resistors selects a voltage range from the high voltage batteries. Capacitor C1 acts as a buffer for this voltage, while an AC-input controls fine motion of the cavity. Potentiometers R1 and R2 offer mid-range control at the low and high voltage ranges respectively.

A PI controller with a second DC-offset is used to tailor the output signal for optimum locking. Recall from above that only a few tens of μV are needed to move over the cavity linewidth. We thus attenuate the output of the PI controller with a 1/100 voltage divider to reduce noise and improve the cavity lock. A slow resistive switch, made with a single turn 10k potentiometer switches between the output of the voltage divider and a ramp generator. This generator allows us to scan the PZT and bring the cavity onto resonance for locking. The output of the resistive switch is then connected to the AC-input of our cavity battery box.

The cavity battery box allows operation over 8 digits of dynamic range. Batteries exhibit wonderfully low voltage noise and have no inherent reference to ground. We exploit this fact in our battery box design, shown in Fig. 41. Three 500 V Eveready flash batteries (No. 497, NEDA 741) in series provide the DC voltage needed to tune the cavity over $\lambda/2$. A "digital" potentiometer is constructed from a ten-way rotary switch and ten 1 MΩ resistors. This allows us to select a coarse voltage range to work in. Mid range adjustment

is accomplished by adjusting two 10-turn 100 kΩ potentiometers, R1 and R2.

For AC signals, a simple calculation reveals the following transfer function of the battery box:

$$V_c = V_{AC} \frac{1 + C_1 s R_t}{1 + C_1 s R_t + C_{PZT} s R_t} \tag{80}$$

Where R_t is the parallel resistance of the top and bottom portions of the voltage divider, s $= j\omega$, and $C_{PZT} = 2.5 nF$ is the capacitance of the cavity PZT. If we choose $C_1 >> C_{PZT}$ we can neglect the last term in the denominator, which gives a transfer function of 1 (In our system, C_1 is 20 nF). For a detailed discussion on transfer functions and their application in control theory we direct the reader to [116]. We measure an RMS noise of less than 1 μV from this battery box, which provides excellent locking of the cavity.

5.2.4.3 Locking Performance

In order to lock the cavity, we observe the transmission on the spectrum analyzer and scan the cavity PZT with the ramp generator while moving the transmission peak into the center of the scanning range with the mid-level potentiometers. The proportional feedback is left on, while the integral feedback remains initially off. The scan amplitude is reduced until the peak fills the screen at which point we adjust the resistive switch to engage the lock. The extreme voltage sensitivity of the cavity length requires a very low proportional feedback. With this method, it is simple to see if the proportional gain is too high, as the error signal will begin to oscillate at some point in the lock engagement. Once the proportional control has been properly adjusted and the lock has been fully engaged, the integral feedback is turned on locking the cavity on transition.

The locking time is given essentially by the integrator circuit in the PI control. Once this circuit reaches the rail voltage of the power supply, the cavity has drifted out of locking range and we lose the lock. This locking time can be augmented by an individual (typically the graduate student running the experiment) by observing the output of the PI controller. As this output reaches a voltage rail, and adjustment can be made with a mid-range potentiometer. With this technique the cavity can be locked for hours.

During the experiment we unlock the cavity to observe changes in the transmission due to atom-cavity interaction. This is done by sending a TTL pulse to the blanking input of the SRS pre-amp in Fig. 40 at the time we wish to observe an atomic signal. This in turn sends a zero error signal to the PI controller, indicating that nothing should be changed during the blanking cycle. The P of the control outputs 0 V, while the integrator remains at whatever previous value it was set at, holding the cavity's transmission stable. It is possible to remove the very slight natural drift of the cavity length by adjusting the DC-offset in the PI control. When the SRS sends its blanking signal to the PI, the small DC-offset will compensate for drift by slowly adjusting the integrator. In practice, one simply adjusts this offset until the cavity transmission remains constant during the blanking phase.

5.2.5 Balanced Heterodyne detection

Heterodyne detection is a very powerful technique for measuring both the amplitude and phase of optical signals. Additionally, it offers a 3dB improvement in signal-to-noise ratio (SNR) over an ideal noiseless detector. For a detailed discussion of heterodyne theory and performance, refer to [112]. Below we briefly highlight the theory behind this detection method. Then we discuss our heterodyne measurement setup.

A typically weak signal (Sig) beam is overlapped with a stronger phase coherent local oscillator (LO). This results in the field amplitude:

$$E_d = A_l \, e^{i\omega_l t} + A_s \, e^{i\omega_s t} \tag{81}$$

with $A_l = |A_l| \, e^{i\phi_l}$, $A_s = |A_s| \, e^{i\phi_s}$ and ω_l, ω_s the amplitude and frequency of the LO and Sig beams respectively. The intensity seen by the detector is thus:

$$I \propto |A_l \, e^{i\omega_l t} + A_s \, e^{i\omega_s t}|^2$$

$$I \propto |A_l|^2 + |A_s|^2 + 2|A_l||A_s| \cos((\omega_l - \omega_s)t + (\phi_l - \phi_s))$$

$$\tag{82}$$

The product of this intensity with the detector area gives the incident optical power:

$$P = P_l + P_s + 2\sqrt{P_l P_s} \, \cos((\omega_l - \omega_s)t + (\phi_l - \phi_s))$$

(83)

Which is converted inside the detector to a photocurrent and then to a voltage via Ohm's law:

$$V = i \, 50\,\Omega = \eta \, P \, 50\,\Omega$$

(84)

Where η is the optical power to photocurrent conversion in A/W. Typically the power in the LO is many orders of magnitude larger than the power in the Sig beam, allowing us to approximate:

$$V \approx V_l + 2\sqrt{V_l V_s} \, \cos((\omega_l - \omega_s)t + (\phi_l - \phi_s))$$

(85)

We see that the AC component of this signal oscillates at $(\omega_l - \omega_s)$ with an amplitude of $2\sqrt{V_l V_s}$. This allows us to selectively detect the Sig beam at the known difference frequency. By increasing the power in the LO, we can optically amplify this signal with virtually no added noise, which allows us to easily overcome electronic detector noise.

Variations in the intensity of the LO beam can lead to unwanted noise at the selected detection frequency. Balanced heterodyne detection avoids this problem by incorporating a second detector as shown in Fig. 42. Here the light from the LO and Sig. beams is combined on a beam splitter and detected with two identical detectors. A π phase shift due to reflection in one arm gives the two signals:

$$V_1 = V_l/2 + V_s/2 + \sqrt{V_l V_s} \, \cos((\omega_l - \omega_s)t + (\phi_l - \phi_s))$$
$$V_2 = V_l/2 + V_s/2 - \sqrt{V_l V_s} \, \cos((\omega_l - \omega_s)t + (\phi_l - \phi_s))$$

(86)

Subtracting these two signals removes the LO fluctuations from the signal, while retaining the Sig information.
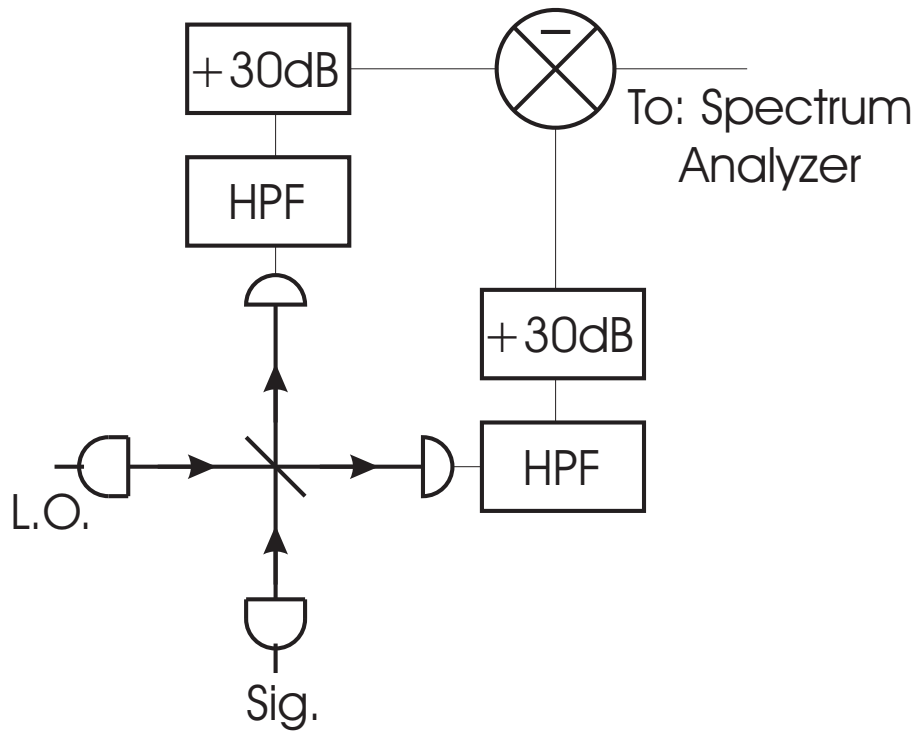
Figure 42: A schematic of the dual heterodyne detection scheme. The signal and local oscillator beams are combined on a beamsplitter and detected with EOT ET-2030 low noise silicon pin detectors. A bias-T sends only the AC component of this signal to a 30 dB amplifier. The signals are then subtracted and sent to a spectrum analyzer for measurement.

In our experiment, we use balanced heterodyne detection to measure very weak light signals from the cavity in real time. Light from the cavity laser, locked 211 MHz below the $F = 2$ to $F' = 3$ transition, is split into the LO and Sig beams. The local oscillator is passed directly to the heterodyning setup (see Fig. 42) while the signal beam is passed through two AOMs of non-commensurate frequency (i.e. 104 MHz and 107 MHz) which add to 211 MHz. This is done so that we do not obtain spurious RF pickup of harmonics at this frequency. The now resonant signal beam drives the cavity mode, which is then coupled to a SMPM optical fiber and brought to the heterodyne setup. There, the light is recombined with the LO on a 50/50 beamsplitter and detected with two identical EOT ET-2030 silicon pin detectors.

A 24 dB amplifier (ZFL-500LN) then multiplies these voltages by $\sim \sqrt{250}$ before they are subtracted from one another and sent to a spectrum analyzer. This signal is detected on the spectrum analyzer set at zero span at 211 MHz and recorded by the computer via the video-out port.

5.3   *Experimental Results in Cavity QED*

In this section, we will describe the results obtained in the cavity QED experiment. We will first show preliminary results obtained with only a single FORT beam and no optical lattice where we observe atomic signals, optical bistability, and a record-high atomic cooperativity parameter. Data from optically transported atoms via our optical lattice will then be presented. Finally we will show delivery of a single atom into the cavity mode, and discuss the current limitation in this experimental apparatus.

5.3.1   Alignment and Initial Observations

In our first experiment, atoms are collected in the MOT and "funnelled" into the cavity mode via a traveling wave dipole force trap that overlaps both the MOT and the cavity. We observe atomic passage through the cavity mode as modifications in the transmission of a resonant cavity probe beam detected with a heterodyning setup (see Sec. 5.2.5). The alignment of the FORT laser is critical due to the small size of the cavity mode and FORT beam. Below, we describe the 3-step alignment process used to couple atoms into the
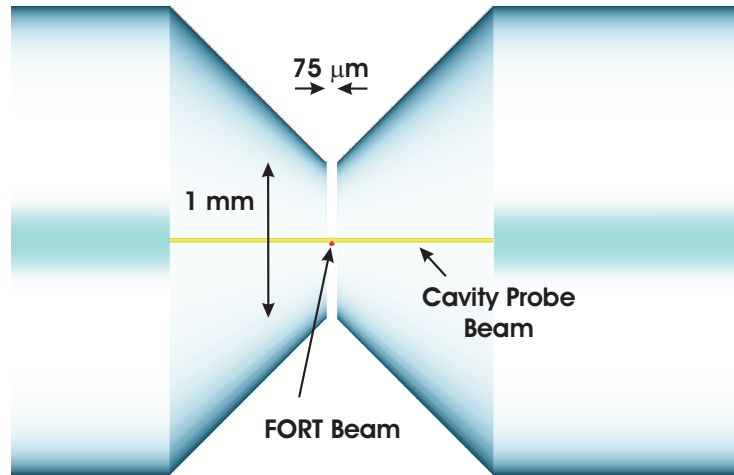
Figure 43: A schematic of the mirror spacing, cavity probe beam, and FORT beam drawn to scale. The alignment of this system is very delicate.

cavity. After this alignment, we observe a remarkably efficient loading mechanism allowing observation of an atomic cooperativity parameter $C=Ng_0^2/\gamma\kappa$ of 5400, almost two orders of magnitude larger than previous work [117].

Step 1

First, we align the vertical FORT beam through the cavity by observing its transmission on an infrared (IR)-card or IR-scope. The beam is properly aligned when it passes through the center of the mirrors and exhibits minimal distortion. One needs five degrees of freedom for proper alignment of this system because the focus must overlap exactly at the center of the cavity (3), and pass through the plane defined by the mirror gap (2). For this system, we simply used a 5-axis translation stage, however one can also use two 2-axis mirror mounts and a 1-D translation stage for the z-positioning of the focus. This rough alignment does not guarantee that the waists of the cavity and FORT beams overlap. Indeed Fig. 43 shows that this final alignment is much more difficult to achieve.

Step 2

Once the FORT has been aligned to the cavity, a second alignment process overlaps the MOT with the FORT to ensure proper loading. This is done by moving the MOT

coils with a translation stage. Initially, resonant light can be inserted into the fiber along with the FORT beam to make a rough alignment of the MOT location. Even for very small powers, the MOT will be greatly perturbed by this light. Observing this perturbation with a CCD camera allows for real-time feedback of the MOT alignment. However, since the traveling wave does not provide confinement in the vertical direction, we must retro-reflect the beam to make an optical lattice to observe loading into the FORT. In a lattice, the atoms are supported against gravity and we can measure a fluorescence signal from trapped atoms after the MOT has fallen away. This signal is proportional to the number of atoms trapped in the FORT and enables us position the MOT to maximize this number. Our MOT contains about 10^6 atoms, of which about 10% are typically transferred to the FORT. Although this is far from optimal [105], our ultimate goal is to work with single atoms in the cavity.

Step 3

A final alignment process overlaps the FORT beam with the cavity mode by monitoring the transmission of resonant light through the cavity as the atoms are guided by the FORT. The FORT beam is swept through the mirror gap until a drop in transmission is observed. We then increase the power and iterate the alignment process. In this way the coupling into the cavity mode can be maximized.

The data in Fig. 44 shows transmission through the cavity for several different input powers as the atom cloud is guided through the cavity mode. Here, the cavity is detuned $\delta_c = 2\pi \cdot 4 \times 10^6$ rad/s below both the atom's (ω_a) and the probe beam's (ω_l) frequency. Although the atomic profile in the vertical direction is approximately gaussian, we observe abrupt switching of the transmission signal. For the lowest powers, spikes in the trans-mission at the leading and trailing edges of the cloud indicate individual atomic transits through the cavity mode.

The abrupt nonlinearity of the cavity transmission discussed above is due to the absorp-tive bistability of the system resulting from a saturable medium interacting with the cavity. In this case, the saturable medium is in the form of many radiating atoms [117, 118, 119]. With many atoms in the cavity mode, the relation (note that this is *not* a *function* of the
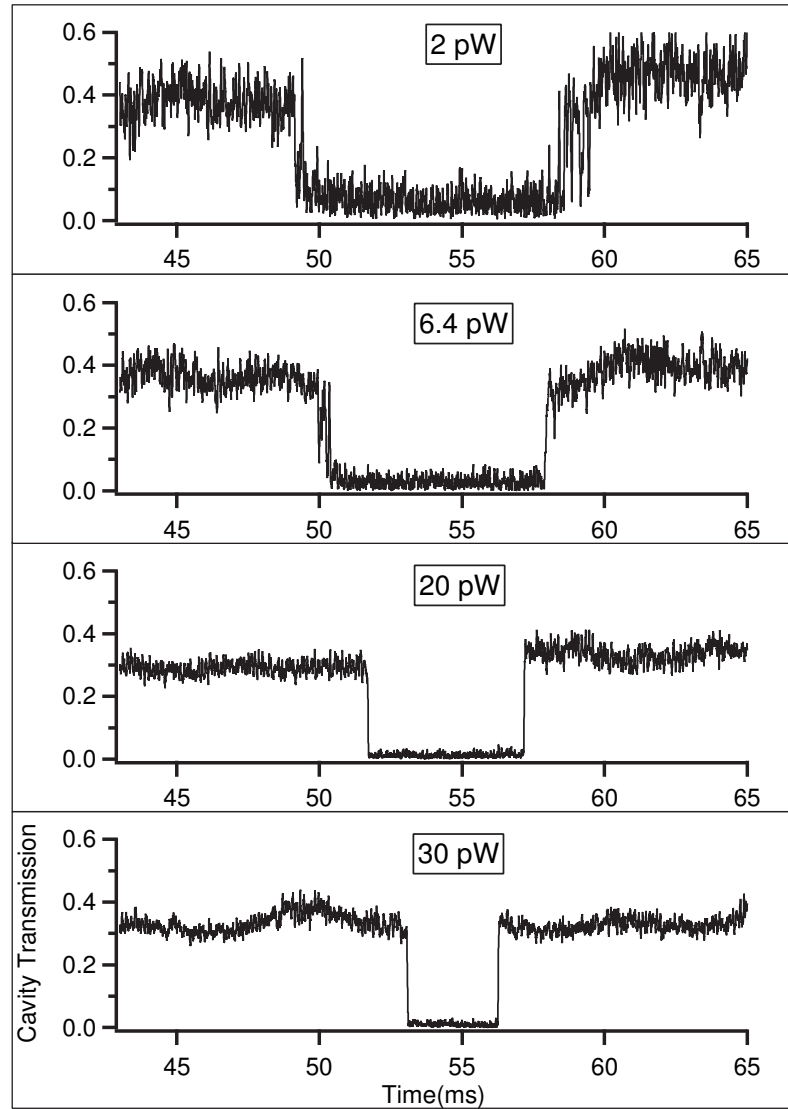
Figure 44: The transmissions of four different probe beam powers are plotted versus time as the atomic cloud is guided through the cavity by the FORT beam.
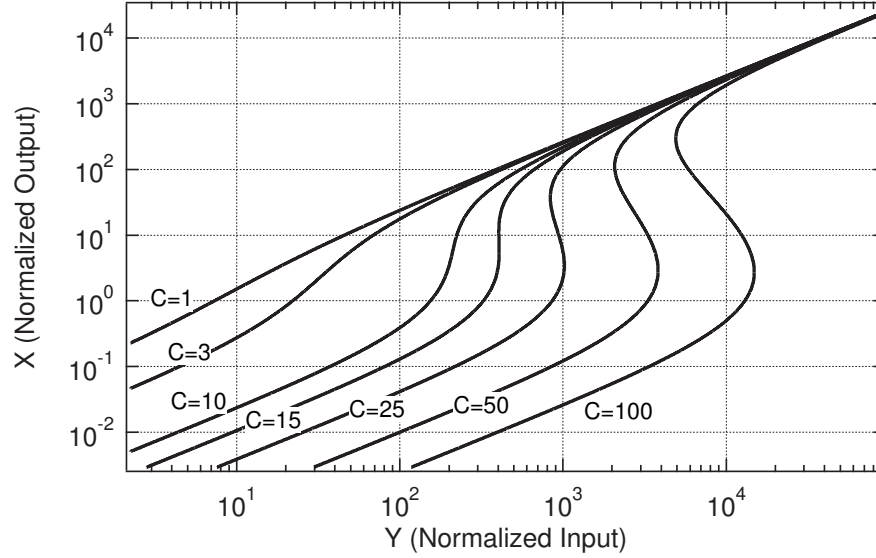
Figure 45: Output versus input intensity for several values of the cooperativity C. These plots were generated using Eqn: 87 and $\delta_c/\kappa = 1.66$. Note the onset of bistability at C=15.

input intensity) between input and output intensities is given by [120]:

$$Y = X[(1 + 2C\chi)^2 + (\delta_c/\kappa)^2] \tag{87}$$

where $X = (I_o)/(I_{sat}T)$ and $Y = (I_i)/(I_{sat}T)$ are the output and input intensities normalized to the saturation intensity I_{sat} and cavity transmission T (we convert between the values of X and Y and the measured power with $P = XTI_0\pi w_0^2/2$), δ_c is the cavity detuning from the atomic resonance and

$$\chi = 3\ln[((1 + \sqrt{(1 + 8X/3)})/2)]/(2X). \tag{88}$$

The value of 8/3 appearing in the expression for χ is a geometrical factor obtained by averaging over the standing wave gaussian profile in the cavity. This is valid because the cloud of atoms inserted into the cavity is localized to $\sim w_{FORT}$=30 μm, which spans many nodes of the cavity field (spaced at ($\lambda = 780nm/2$). For values of C>15 Eq. 87 predicts two stable output intensities for certain values of the input intensity.

We can measure this bistability directly by allowing the atomic cloud to enter the cavity with the probe beam initially off. We then ramp the probe beam to a high power and back
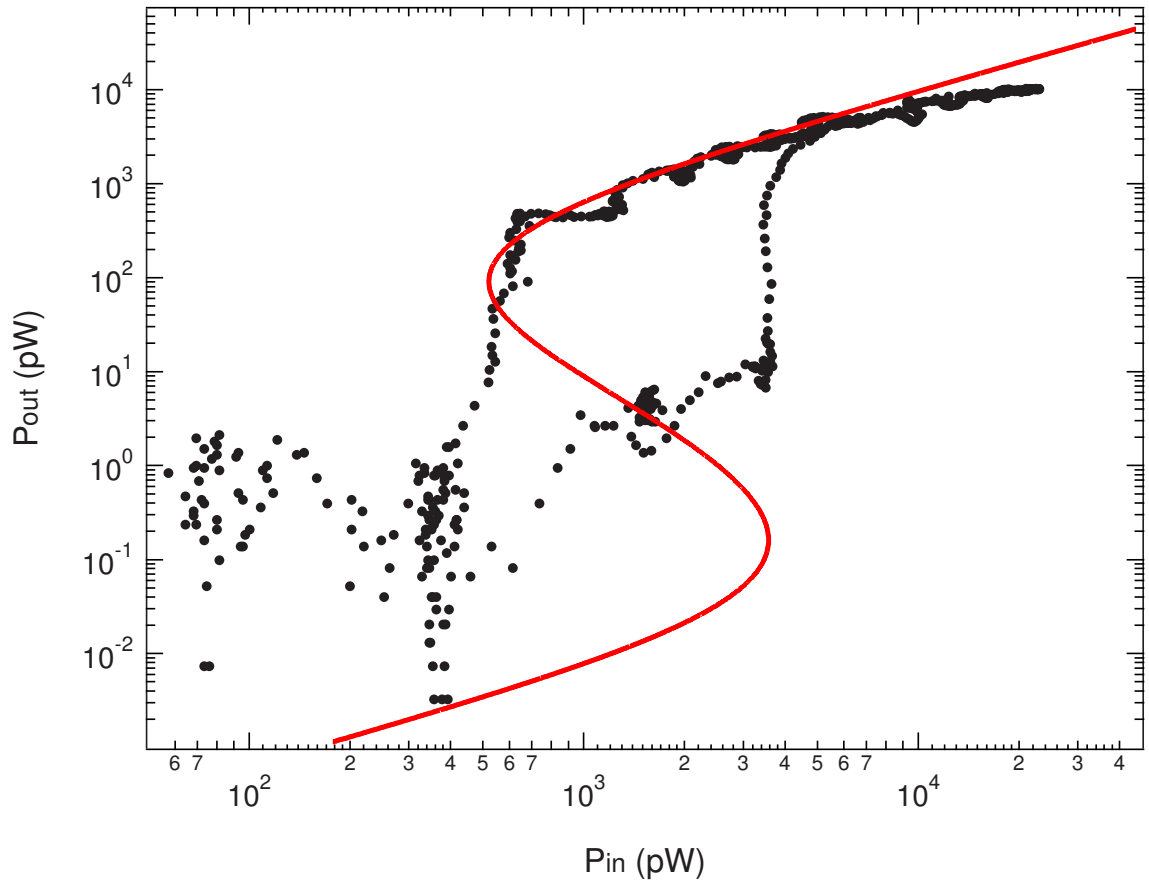
Figure 46: A plot of cavity input power versus output power. This data was collected in 1 ms while the center of the atomic cloud overlapped the cavity mode. The curve shows a plot from Eqn. 87 with C=200.

over a timescale that is much shorter than the cloud transit time. We assume here that the cooperativity is constant during this probe. The results of this measurement are shown in Fig. 46 where the hysteresis is clearly evident. These data are taken from a single experimental run in real time, unlike the experiments of [117, 118] performed with atomic beams. We fit a bistability curve with $C = 200$ to this data with good agreement at higher powers and for the switching points. For lower powers, the agreement is less satisfactory although the noise floor of the heterodyne measurement complicates the analysis of this data.

The data in Fig. 44 corresponds to a slightly different situation. Here, the input power to the cavity is held constant while the atom number and hence the cooperativity C is changed. We can understand this behavior by plotting the output power versus cooperativity (as done in Fig. 47). For each of these powers, we see two distinct regions of high and low transmission. As the atomic cloud enters and leaves the cavity, we move to the right and then back to the left on these curves. The sharp drop in observed cavity transmission corresponds to crossing into the low transmission region. Also, the asymmetry observed in Fig. 44 corresponds to the bistability observed for higher input powers in Fig. 47.

5.3.2 Observations of Large Atomic Cooperativity

We saw in the last section that the response of the cavity transmission to the introduction of many atoms is described quite well by the theory of absorptive optical bistability. We have used this technique to measure the number of atoms coupled into the cavity mode by implicitly solving the bistability equation (Eq. 87) for C with known input and output parameters. Then, by increasing the probe power, we can map out the cooperativity versus time.

For this experiment, we use a Ti:Sapphire laser (described in detail in Ch. 6) at 850 nm with a power of 400 mW focused to 22 μm, which increased the trap depth to 240 μK. Additionally we introduce an additional repump beam (as in [83]) perpendicular to the cavity axis to prevent atoms from being pumped into the $F = 1$ state, which is dark to the probe light. The cavity's and probe laser's frequencies are identical to those used in the
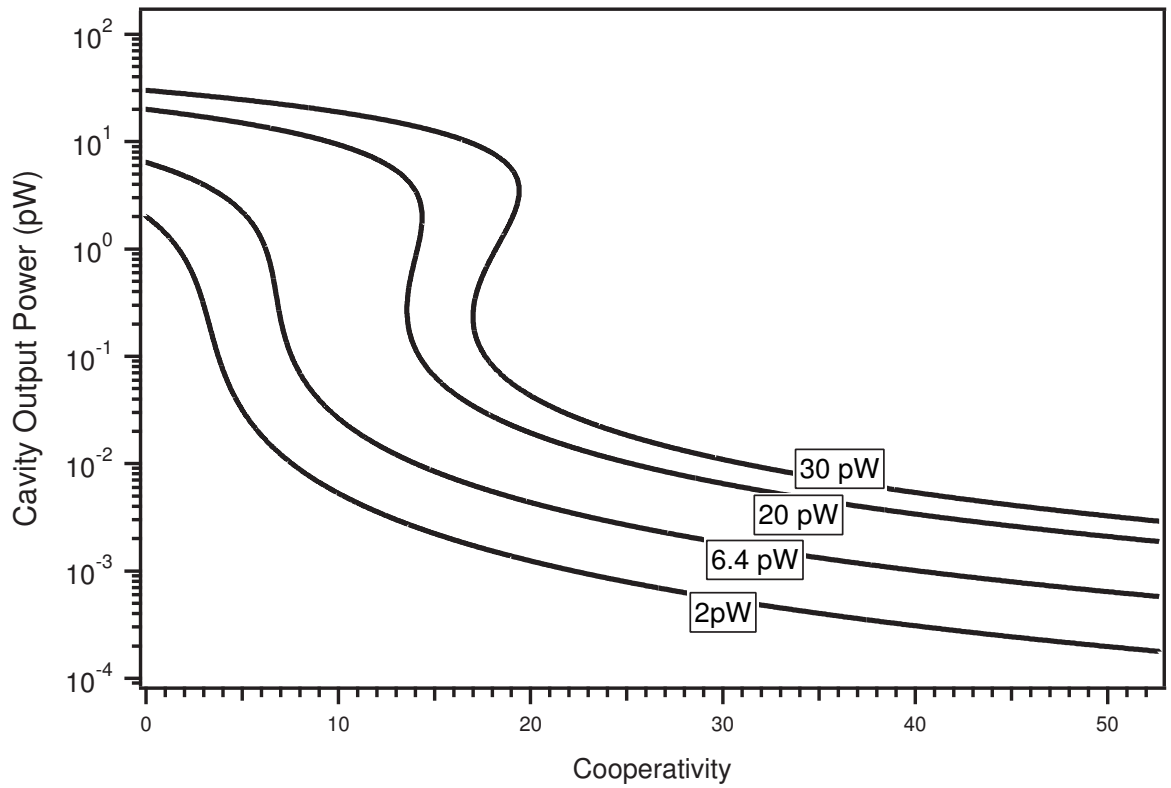
Figure 47: A plot of the output power versus cooperativity for several input powers. These input powers correspond to those used in Fig. 44.
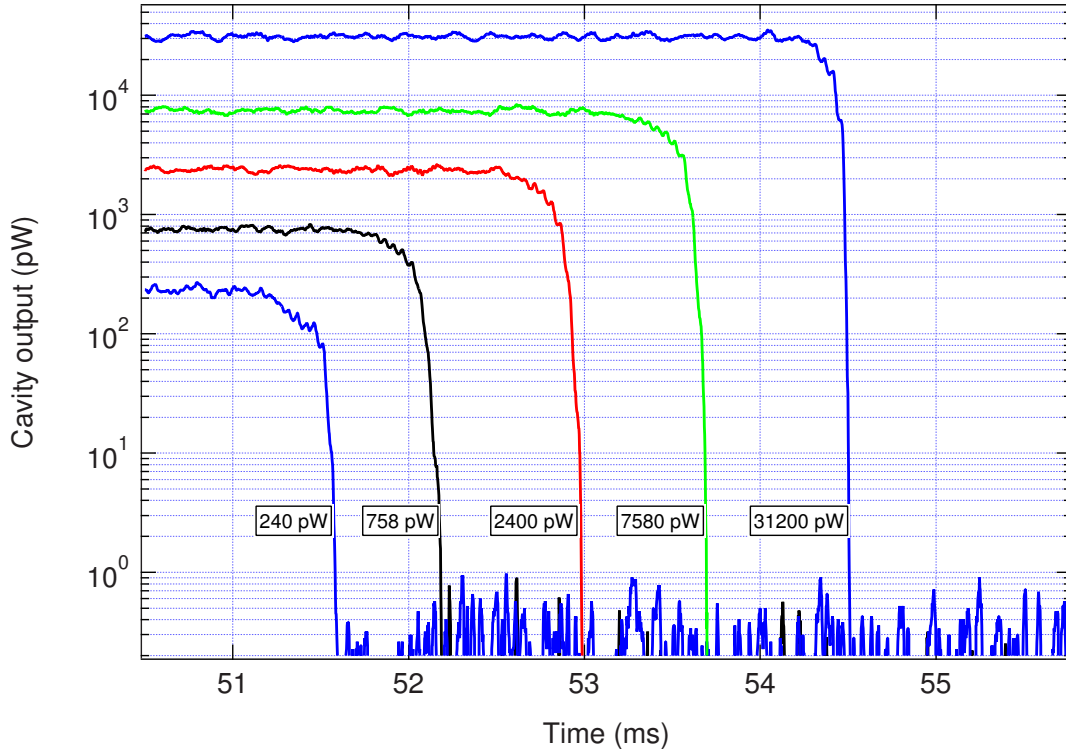
Figure 48: Transmission curves at several different input powers as the atomic cloud enters the cavity. The data from the abrupt drop in transmission is fitted to bistability curves in Fig. 49 to extract cooperativity data.

last experiment. This laser offered improved loading from the MOT which allowed larger numbers of atoms to be coupled into the cavity.

Fig. 48 shows the results of these measurements with higher probe beam powers. We observe switching of larger probe powers at later times, corresponding to a higher number of intracavity atoms. For powers greater than 31,200 pW, the transmission does not drop during the atomic transit. We plot the data points from Fig. 48 against bistability curves in Fig. 49 (Top). From these fits, we can extract a cooperativity parameter from each data set. These values of C are given in Fig. 49 (Bottom). Cooperativities of up to 5400 were measured, corresponding to a maximum intracavity atom number of $\sim$100 and an atomic density of $\sim 10^{10}$ cm^{-3} inside the cavity. The maximum switched probe output power is 8 nW, corresponding to an intracavity intensity of $7 \times 10^5 I_{sat}$. It is remarkable that such a large intensity can be extinguished by only 100 atoms.
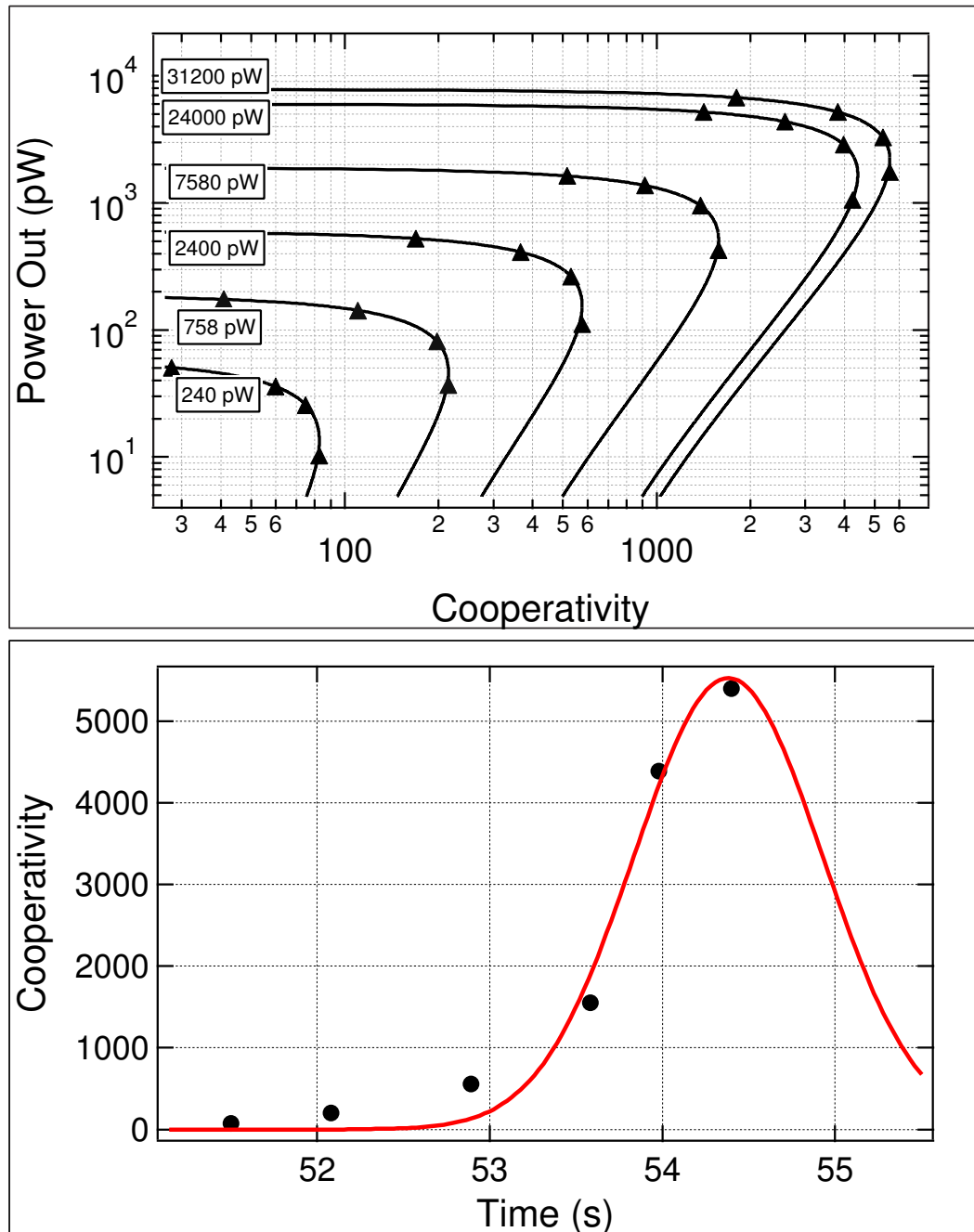
Figure 49: (Top):Data from Fig. 48 are fitted to bistability curves to extract cooperativity data. (Bottom) These data map out the atomic cooperativity inside the cavity versus time. The maximum value of 5400 is the highest atomic cooperativity ever observed to date.

5.3.3   Optically Transported Atoms in the Cavity

The next experiment allows groups of transported atoms to be deterministically introduced into the cavity. This system has demonstrated atoms transported back and forth through the cavity mode, as well as the delivery of a single atom. The previous two experiments utilized a FORT to guide atoms from the MOT into the cavity mode. Although these atoms do not randomly enter the cavity after ballistic expansion from a MOT as in [77, 111] or from an atomic fountain as in [121, 79, 82, 122],individual atomic arrival time is determined by the random distribution of atoms in the cooled atomic cloud.

For this experiment, we add a second FORT beam that is tuneable in frequency over $\Delta\nu = \pm 1$ MHz counterpropagating to the first to create a standing wave. The second beam is derived from the same Ti:Sapphire laser used in the previous experiment and its frequency is modulated with an AOM as described in section 5.2.1. Since the light from the Ti: Sapphire has to be split into two beams, there is only 200 mW available per beam. However, because the optical lattice has four times the trap depth of a traveling wave trap, the trap depth at the focus increases to 480 μK. Near the MOT, the beam diverges to a waist of 185 μm, decreasing the trap depth to only 7 μK.

The standing wave potential generated by interfering the two beams is given by Eq 69:

$$U(r,z,t) = U_0 \frac{w_0^2}{w(z)_0^2} \, e^{\frac{-2r^2}{w(z)^2}} \cos^2(\pi\Delta\nu t - kz).$$

(89)

This represents a lattice that retains its gaussian profile in the transverse direction but moves with a velocity of:

$$v = \frac{\pi\Delta\nu}{k} = \frac{\lambda\Delta\nu}{2}$$

(90)

along the z axis. Thus we can transport these atoms into the cavity simply by adjusting this difference frequency. This technique of moving neutral atoms was first demonstrated by Meschede *et al* [104], however they do not use a cavity in their system.

Some atoms are not bound in the lattice, but are still guided by the transverse optical potential into the cavity. This leads to an observable atomic signal caused by unbound
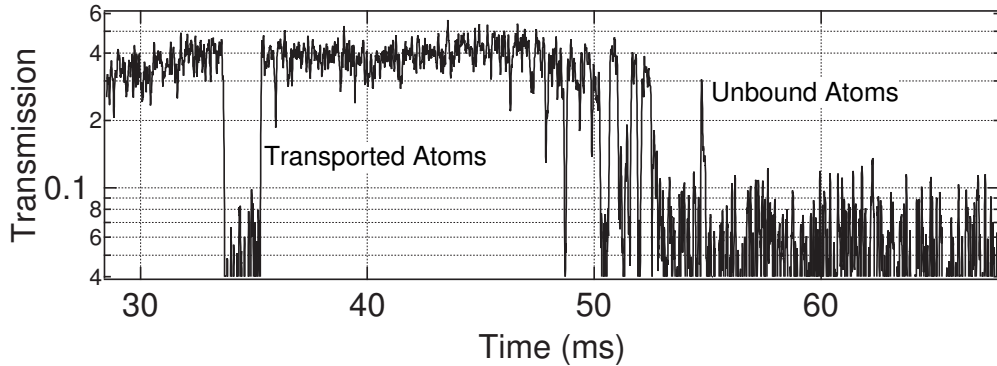
Figure 50: Optically transported atoms into the cavity mode. A trace of the normalized cavity transmission versus time shows atoms delivered to the cavity 21 ms before the unbound atoms at an acceleration of 1.6 g. This data was taken with an input power of 2 pW.

atoms that is present in all the data sets containing delivered atoms as well. However, these atoms are distinctly discernable from other features and shall be omitted when appropriate. It is conceivable that a reduction of the trap losses and improvement in lattice contrast could eliminate this signal altogether.

Our first demonstration of atomic delivery is shown in Fig. 50. Here atoms trapped in the wells of the lattice are accelerated at 1.6 g to a maximum speed of 53 cm/s. The input power into the cavity for these measurements is 2 pW, which allows observation of the single atom trickle observable at the leading edge of the unbound atomic signal.

By reducing the intensity of the MOT beams and increasing the field gradient of the MOT coils, we can reduce the atomic loading into the lattice such that the average number of atoms loaded is much less than one. Delivery of a single atom is shown in Fig. 51. Unlike [123], we do not have the imaging capability to independently verify that we have indeed loaded exactly one atom. However, for this data we have lowered the number of atoms loaded into the lattice such that we observe only one transit signal in twenty iterations. We thus argue along the same lines as [77, 78, 80] that when an atomic signal is observed, it is indeed due to a single atom. A more rigorous verification of the atom number would have been possible, if the lifetime of the lattice trap had allowed us to hold the atom in the cavity. Recent improvements to the system show that this will be possible in future experiments.

108
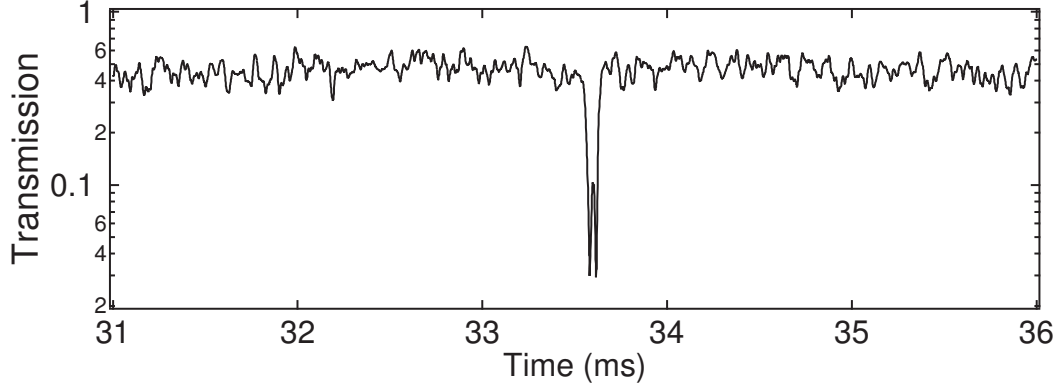
Figure 51: A single atom delivered into the cavity. This atom arrives 21 ms before the unbound atoms arrive into the cavity mode.

In a final demonstration of atomic delivery, we accelerate the occupied lattice sites down into the cavity mode. The trapped atoms pass through the cavity and are brought momentarily to rest. Then they pass through the cavity again as the lattice velocity is reversed and they are returned to their original position. A time series of the atoms being lowered down to the cavity is shown in Fig. 52. The maximum velocity of the atoms is 30 cm/s, and the maximum acceleration imparted is 1.5 g. The graph in Fig. 53 (Bottom) shows the position and velocity of the lattice sites measured relative to the cavity axis, while Fig. 53 (Top) shows the cavity transmission for this event.

The unbound atoms are detected at 55 ms (as in every trace) as a dip in the transmission. The two thinner and more pronounced drops in transmission are due to the atom packet tightly confined in the lattice moving back and forth through the cavity mode. The gradual drop in transmission seen on the far right side of the top graph in Fig. is due to heating of the cavity mirrors by the FORT laser beam.

We can calculate the positional uncertainty in the second pass through the cavity based on the known position of the first. This allows us to assign a figure of merit to the deterministic delivery of the second group of atoms into the cavity. Fig. 54 shows the results of this measurement. Time is measured between the points at which the cavity transmission falls to 10% in the first and the second atomic passage through the cavity mode. Data is collected from 70 different experimental runs and converted from temporal uncertainty into positional uncertainty using the known velocity during the second atomic passage. An
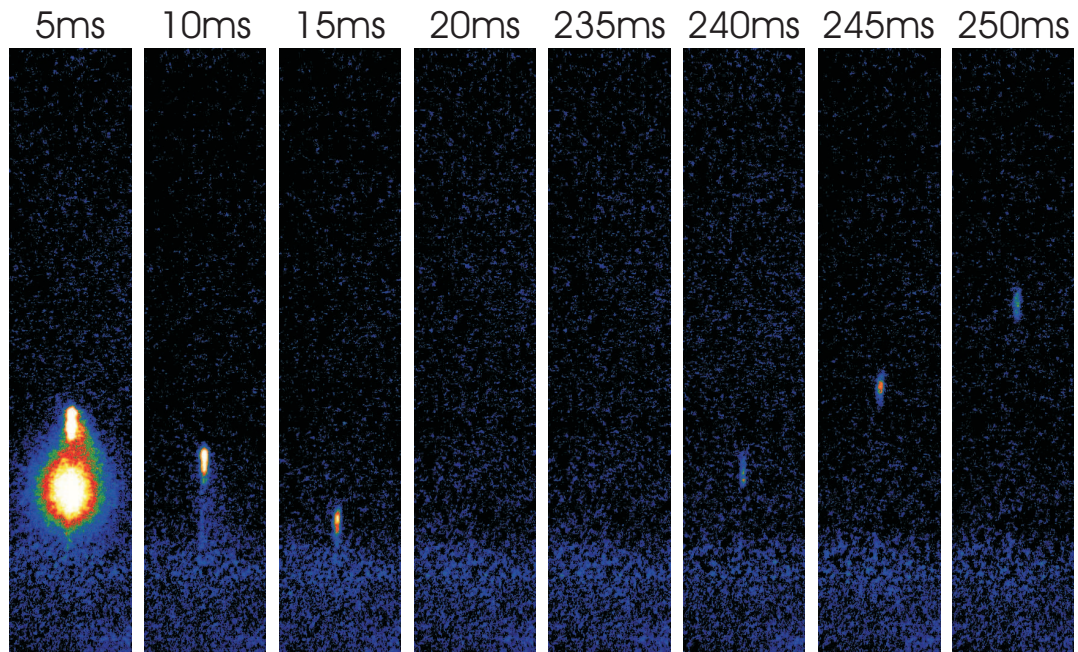
Figure 52: An image series of the atoms trapped in the optical lattice as they are lowered into the cavity and returned. In the first image, the unbound atomic cloud can be seen as it falls away from the trapped atoms in the lattice. Losses out of the lattice trap can be seen in the weak atomic signal of the last images. The transmission of the cavity for this process is shown in Fig. 53.
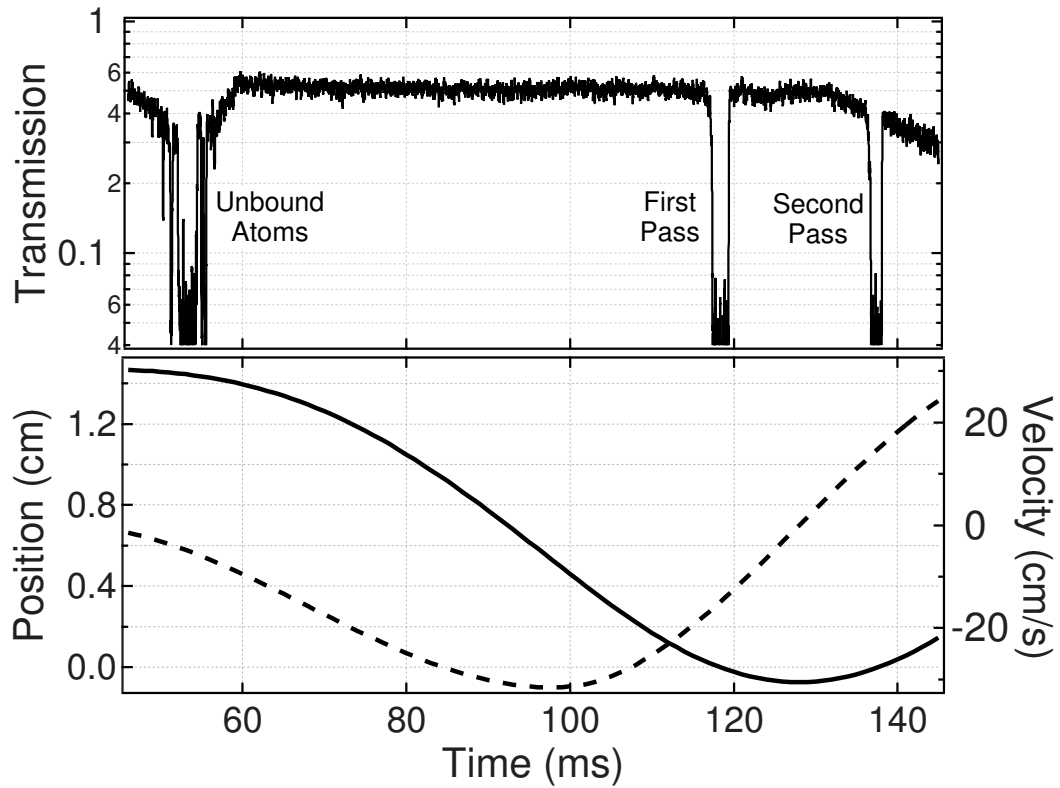
Figure 53: (Top) Transmission of the cavity probe beam shows a group of ~ 5 atoms transported first down and then back up through the cavity. The first dip in transmission at 55 ms is due to unbound atoms as they fall through the cavity (240 pW probe power). (Bottom) Position (solid line) and velocity (dashed line) of the atoms trapped in the optical lattice.
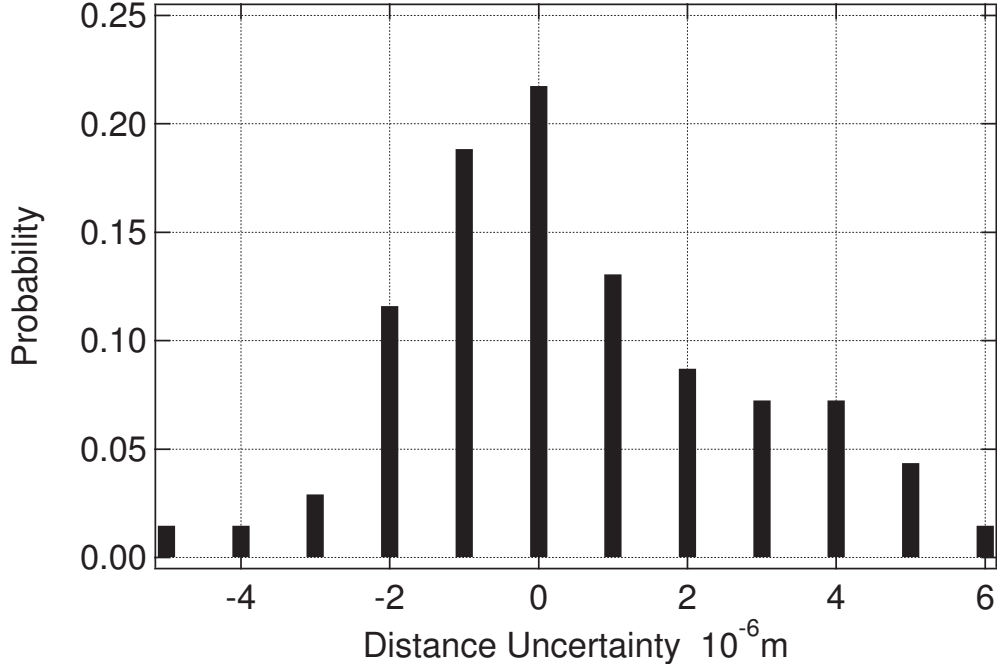
Figure 54: A histogram plot of positional uncertainty in atomic delivery. This plot represents data collected from 70 data sets.

RMS deviation in the position of 4.6 μm is observed. We expect positional control of the lattice to be better than $\lambda/2 = 0.43\mu$m as in [104], a factor of 10 smaller than observed. However, we attribute this uncertainty to trap losses during the abrupt reversal of velocity rather than errors in the optical positioning system. If atoms are lost from the lattice, the maximum cooperativity will be reduced. This will cause fluctuations in the point at which the transmission falls. The random nature of these losses then produces uncertainty in the cooperativity versus time, which is what we have recorded. Note however, that this nevertheless allows accurate positioning to within $\sim 1/4$ of the cavity waist with a corresponding reduction of only 6% in the atom-cavity coupling $g(r)$.

5.4   Summary of Cavity QED Experiment

We have realized a cavity QED system with optically trapped and transported atoms. Initial observations indicate that our unique cavity design, suspension system, and electronic control system produce an optical cavity with a passive length stability that is unsurpassed. Groups of atoms can be deterministically delivered to the cavity mode. The delivery of

this large atomic density into a strongly coupled cavity system provide for a measured atomic cooperativity C up to 5400, the largest observed in a system to date for atom cavity systems. The successful demonstration of this scalable trapping geometry opens exciting opportunities in the implementation of quantum gate protocols, and quantum information networking.

A major limitation in the achievement of deterministic coupling of a single atom to the mode of our cavity is the heating of the cavity mirrors induced by the trapping laser. This heating is shown to be responsible for large movements of the cavity length, in spite of only minimal absorption by the glass mirrors. A solution to this problem is presented in the form of an off-resonant locking system, which is currently under construction in our laboratory.

5.5   *Current Experimental Limitations*

The preliminary results from this experiment are limited mainly by two factors: First, the lifetime of the optical lattice trap is on the order of the transit time from the location of the MOT to the cavity. Furthermore, the translation of the lattice sites causes additional losses from the trap. Second, a portion of the light from the FORT laser is absorbed by the cavity mirrors, which causes thermal fluctuations in the length and thus the resonance frequency of the cavity. Below we highlight details of each of these limitations.

The most troubling limit is the losses associated with positioning the atoms. Our quantum computing scheme (see section 4.1) relies on the ability to deterministically position single atoms within the mode of a high-finesse optical cavity for the duration of a calculation. A large portion of our efforts at Georgia Tech have recently been devoted to characterizing and improving both the lifetime and the positioning integrity of the optical lattice. A detailed discussion of this work will be provided in the next section.

We have calculated that the cavities resonance frequency will shift one linewidth in 10 ms due to thermal expansion if the cavity mirrors absorb only 0.04% of the FORT beam power. We cannot accurately determine the amount of power absorbed by the frosted glass on the coned tip of these mirrors, because vacuum windows and other components attenuate the FORT beam more than the cavity. However, even for a perfectly focused gaussian beam,

the aperture defined by the cavity mirrors blocks 0.15% of the light. This illustrates a somewhat fundamental problem with our scheme. In order to produce a lattice trap that does not cause decoherence due to excessive photon scattering, the detuning of the FORT must be large. But this large detuning demands a large power to maintain adequate trap depth. This large power must be focused between the mirrors of the cavity, which must be kept close together to produce a strongly coupled atom-cavity system.

As a result, we must either produce a thermal shield (such as a gold coating of the coned surface) or encorparate a locking scheme that does not affect the atoms while in the cavity, such that it can remain on during the experiments. In fact, we have chosen to implement a similar locking system to that used by the Kimble group [83] and the Rempe group [84]. In this scheme, a second laser copropagating with the cavity probe beam but detuned by exactly one FSR is used to lock the cavity. This system requires a second transfer cavity and an additional laser but produces a locking system that does not affect the atoms because of its large detuning from the atomic resonance. This system is currently under construction in our lab.

CHAPTER VI

EXPERIMENTAL RESULTS IN ATOMIC POSITIONING

As mentioned in the last chapter, a major limitation in the successful implementation of our quantum computing scheme has been the atomic positioning control. Heating and losses in the stationary optical lattice, as well as additional losses from atomic transportation, currently limit this control to those results already presented in Ch. 5. We have expended a great deal of effort characterizing and improving this mechanism, which is the subject of the next few sections.

6.1 Heating and Loss Mechanisms in FORTs

There are several well documented heating and loss mechanisms in traveling wave dipole force traps, including off-resonant atomic excitation [102], parametric heating due to intensity fluctuations and pointing instabilities [124], photoassociative collisional losses [125], and ground state polarization dependent dipole force fluctuation heating [51, 126]. We can rule out the latter possibility, because these are induced by elliptical polarizations in the FORT laser beam, where our beams are linear. Also we do not believe that photoassociative collisional losses play a role in our trap, because they exhibit a unique wavelength dependance that we did not observe. Below, we will describe the first two heating mechanisms and their predicted loss rates.

6.1.1 Absorption and Spontaneous Re-emmision

Absorption and spontaneous re-emission of trapping photons cause heating due to their random nature [127]. Fluctuations in absorption lead to an average increase in kinetic energy corresponding to the recoil energy per photon:

$$E_{rec} = k_b T_{rec}/2 = \frac{h^2}{2M\lambda^2} \tag{91}$$

Where M is the mass of the atom and λ is the *atom's* resonant wavelength. The re-emmission process contributes the same amount of energy so that for every scattering event, the total kinetic energy increases on average by $2E_{rec}$. For a red-detuned 3D harmonic trap, where the kinetic energy of the atoms is much less than the trap depth ($k_B T << U$), this leads to a heating rate of [102]:

$$\dot{T} = \frac{2}{3} T_{rec} \frac{\Gamma}{\hbar |\Delta|} U \tag{92}$$

This equation predicts a linear heating of the atoms in the trap, for it does not depend on the temperature itself. However, the condition $k_B T << U$ is not fulfilled once the atom has undergone significant heating because a hot atom will spend more time in regions of lower intensity and scattering rate, lowering the effective heating rate. We can nevertheless deduce the relevant timescale for heating an atom out of the trap by comparing the increase in kinetic energy to the trap depth:

$$\tau_{sc} \approx \frac{U}{k_b \dot{T}} = \frac{3\hbar |\Delta|}{2 k_B T_{rec} \Gamma} \tag{93}$$

The trap depth vanishes from this expression, which clearly shows the advantage of large detunings. Indeed, if this were the only heating mechanism, one would expect the lifetime of the trap to linearly increase with detuning. Of course, this expression is only valid for a two-level atom. For multi-level atoms, like those used in most cooling and trapping experiments, the detuning relative to each transition must be taken into account (such as in Eq. 64). The corrections to the scattering rate for those wavelengths used in our experiment (781.2 nm, 783.4 nm, 850 nm) are always less than a factor of two, so that this expression still leads us to the relevant timescales. Fig. 55 shows the expected lifetime versus wavelength of the trapping light. We see that even for the smallest detunings shown, corresponding to 781 nm, a lifetime of almost 3 s can be expected, whereas for 850 nm, we should see lifetimes $\tau > 100$ s. We note that this heating process is fundamental and sets a lower (although rarely experimentally attainable) limit on the trap lifetime.
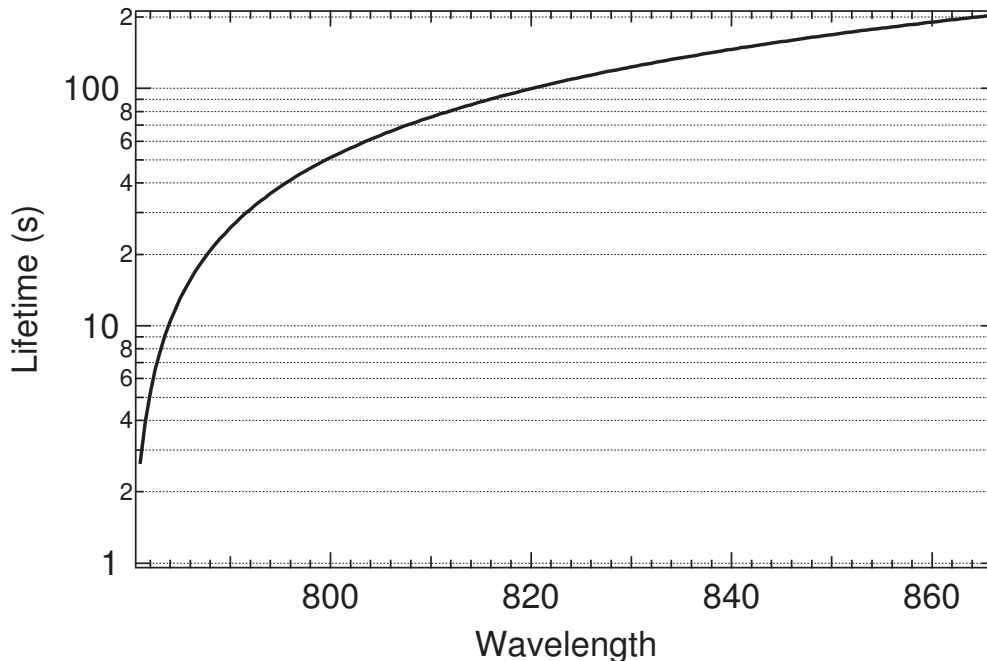
Figure 55: Calculated lifetime of ^{87}Rb in FORT due only to heating from spontaneous scattering of photons. Here, only the interaction of the light with the D2 line is taken into account. This removes a singularity at the D1 line, but does not change the timescale of the heating process for relevant wavelengths.

6.1.2   Intensity Fluctuations and Pointing Instabilities

Non-fundamental technical heating due to intensity fluctuations and pointing instabilities can dominate trap losses if they occur at the right (or more appropriately, the wrong) frequencies. Savard *et al.* [124] have shown that a laser with a one-sided power spectrum of the fractional intensity noise $S_\epsilon(\omega)$ will induce a heating rate in an harmonic potential of:

$$\langle \dot{E} \rangle = \frac{\pi}{2} \omega_{tr}^2 S_\epsilon(2\omega_{tr}) \langle E \rangle \tag{94}$$

Where $\langle E \rangle$ is the average kinetic energy of the trapped atoms and ω_{tr} is the trap frequency. We see that the average energy in the trap increases exponentially and that this process is parametric because it depends on the second harmonic of the trap frequency [128]. For a multi-dimensional trap with more than one frequency, there is a contribution from each frequency that is weighted according to the distribution of kinetic energy among the individual dimensions. In particular, in the case of equal energy distribution, the effective heating rate

117

is the mean heating rate in the x, y, and z directions. Ironically, one can exploit this loss mechanism to experimentally verify the trap frequencies as done in [129]. An example of frequency measurement by parametric resonance is given in Fig. 67.

Pointing instabilities can also lead to heating in dipole force traps. Fluctuations in the position of the trap center lead to a heating rate of [124]:

$$\langle \dot{E} \rangle = \frac{\pi}{2} M \omega_{tr}^4 S_x(\omega_{tr}) \tag{95}$$

Where $S_x(\omega)$ is the one-sided spectrum of position fluctuations in the trap center. This heating mechanism is not parametric, for it occurs at the trap frequency itself. Furthermore it is a linear heating mechanism, unlike intensity fluctuations.

This heating mechanism is also responsible for losses induced by frequency fluctuations in the trap laser. A mismatch in path lengths combines with these fluctuations to produce a shift in the trap center along the propagation axis. If the frequency of these fluctuations matches the trap frequency, it can lead to the loss rate mentioned above.

6.1.3   Estimating Trap Loss

For those heating mechanisms that do not depend explicitly on the density and hence the number of atoms in the trap, we can calculate the loss rate from the trap using the same fundamental principles as those used in evaporative cooling [130, 131] by adding a heating term. The rate of change of energy in the trap is given by:

$$\langle \dot{E_{kin}} \rangle N = \langle \dot{E_{heat}} \rangle N + \frac{\partial E}{\partial N} \dot{N} \tag{96}$$

Where $\langle E_{kin} \rangle$ is the kinetic energy per atom, and $\langle \dot{E_{heat}} \rangle$ is the heating rate. The change in kinetic energy of the atoms is simply the heating rate minus the energy taken away by each atom that leaves the trap. This equation can lead to complicated dynamics, especially if $\langle \dot{E_{heat}} \rangle$ depends explicitly on $\langle E_{kin} \rangle$. However, we are only interested in the steady state solution of this equation where $\langle \dot{E_{kin}} \rangle$=0 and hence the temperature of the atoms is constant

such that the heating is balanced by losses from the trap. In this approximation, the loss rate for all such heating mechanisms will be exponential:

$$-\langle \dot{E_{heat}}\rangle N = \frac{\partial E}{\partial N}\dot{N} \tag{97}$$

If we take, for example, the heating rate for spontaneous emission:

$$\langle \dot{E_{heat}}\rangle = \frac{2}{3}k_b T_{rec}\frac{\Gamma}{\hbar|\Delta|}U \tag{98}$$

and the energy taken away by each atom to be the trap depth U, we arrive at the following equation for the number of atoms in the trap versus time:

$$N = N_0\, e^{-t/\tau} \tag{99}$$

With τ defined as above in Eqn: 93. Agreeing with the estimated lifetime given in section 6.1.1.

6.2   Free Running Diode FORT system

The first experiments implement a free running diode laser tuned 3-5 nm above the Rb D2 line. This laser is split into two beams of equal power and passed through two AOMs before being coupled into separate SMPM optical fibers. The light out of each fiber is collimated by a 6.8 mm aspheric lens, expanded to a $1/e^2$ waist of 1.25 mm using plano-convex lenses and focused to a 30 μm waist with a 150mm plano-convex lens. We position the FORT beams with two 5-axis translation stages mounted vertically above and below the chamber. Only about 16mW of power is available at the location of the cavity, which typically produces a trap depth at 782.5 nm of 72 μK and a scattering rate of 76 s^{-1} in the traveling wave configuration. We estimate the linewidth of this laser to be < 100MHz, which produces a coherence length longer than any relevant distance in the experiment and was therefore not a concern.
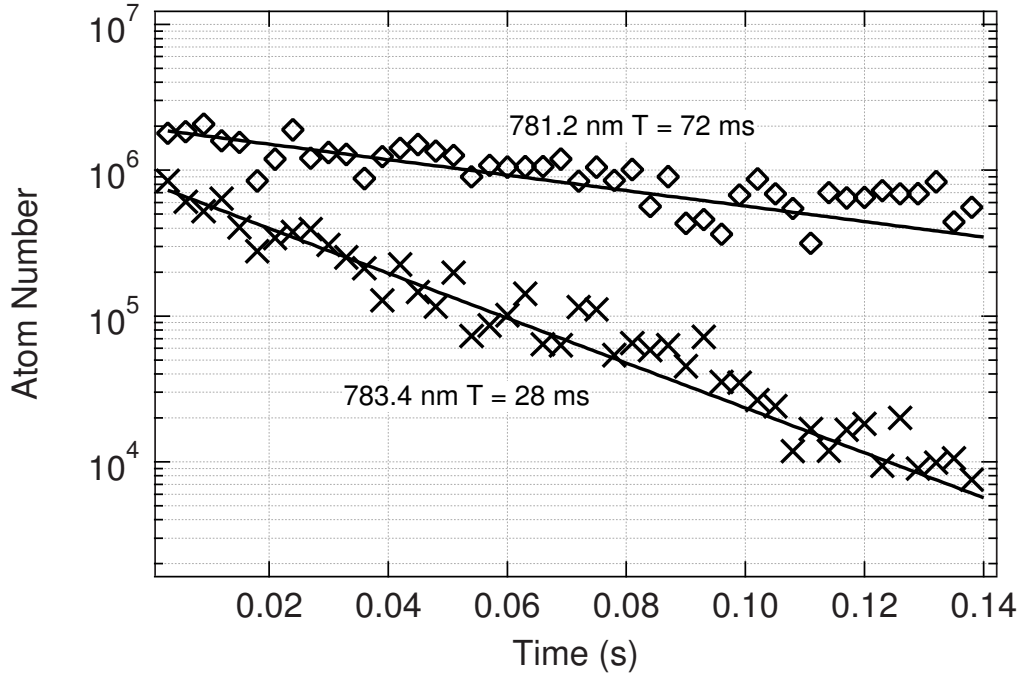
Figure 56: Lifetime of the optical lattice at two different wavelengths. This lattice was produced with 15 mW of power in each beam focused to a $1/e^2$ waist of 30 μm.

A figure of merit for evaluating the trapping laser systems described in this chapter is their trap lifetime. This lifetime sets the timescale over which the cavity QED experiment can occur. We define the $1/e$ lifetime of all traps as the value of τ when an exponential $Ae^{-t/\tau}$ is fit to the number of atoms remaining in the trap versus time. For this laser system, lifetimes vary between 25-72 ms. An example of the losses from this trap is shown in Fig. 56, where we see a 28 ms lifetime at 783.4 nm and a 72 ms lifetime at 781.2 nm.

We also observe that the trap losses are very sensitive to the wavelength of the trapping laser, but do not follow the behavior predicted in Fig. 55. On the contrary, we routinely, though not always, observe the opposite trend. We have purposely selected two such data sets for Fig. 56 where the wavelength dependence follows the opposite trend, for the trap with a wavelength closer to resonance actually shows a larger trapping lifetime!

In an attempt to understand more about the nature of these losses, we change the trapping geometry so that the FORT laser runs horizontal in a plane parallel to the table. Gravity effects the horizontal trap depth much less than the vertical trap due to the small size of the FORT laser's waist. Although this geometry does not intersect the cavity, it does
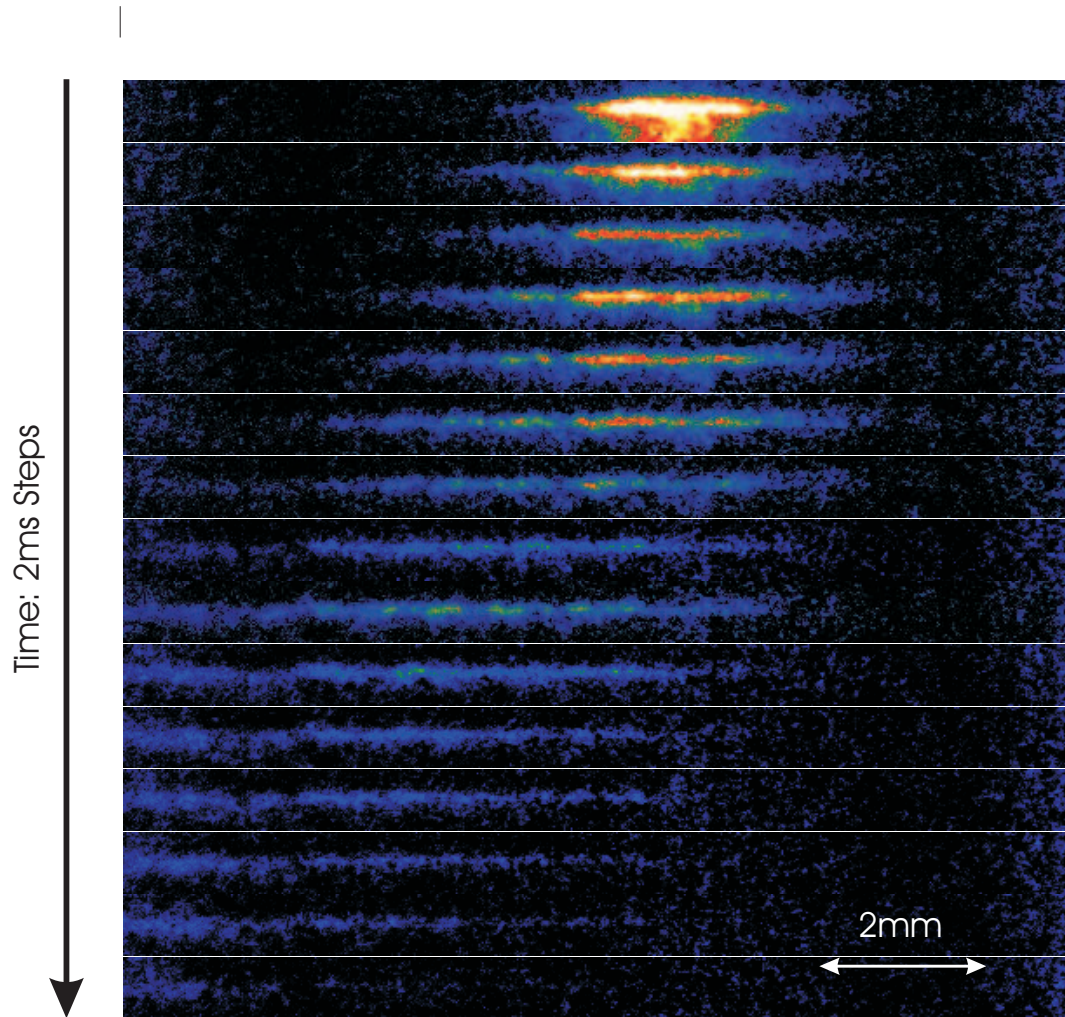
Figure 57: A time series of atoms trapped in a horizontal traveling wave trap shows atoms being "pushed" to the left. The atoms are pushed in the direction of FORT laser beam propagation.

allow us to trap atoms with a single traveling wave, thus eliminating complications from an optical lattice.

Trap lifetime in the horizontal traveling wave geometry was similar to that of the vertical standing wave. However, we noticed for the first time, that the atoms were being "pushed" to one side of the trap in the direction of FORT beam propagation. A time series in Fig. 57 shows the movement of the atoms to the left, which was not due to a tilt in the FORT beam. It appeared that some scattering mechanism was imparting momentum to the atoms.

What we didn't consider while taking this data (but was later pointed out to us by Prof. Alex Kuzmich) is that diode lasers have a broad pedestal of emitted wavelengths that can reach out over many nm [132] in addition to their primary lasing wavelength. An example of this pedestal is given in Fig. 58. This data was taken using an optical spectrum analyzer with light from a free running diode tuned to 783.4 nm. The data is normalized such that the maximum power corresponds to 0 dB.

We notice two striking features about this pedestal. First, even at a primary wavelength that is 3.2 nm above resonance we still have resonant light at the -40 dB level. This might at first appear negligible, but in fact leads to a considerable scattering rate. We can estimate this scattering rate by finding the intensity distributed over the resonant transition:

$$I_r = \frac{2P_r}{\pi w_0^2} = \frac{2P_l A \Delta \lambda_\gamma}{\pi w_0^2 B} \tag{100}$$

Where P_l is the power in the laser, A is the reduction from 0 dB at the resonant wavelength (10^{-4} for -40 dB), B is the resolution bandwidth of the optical spectrum analyzer in nm, and $\Delta \lambda_\gamma$ is the natural linewidth of the atom in nm units (converted at $\lambda = 780$ nm). Inserting this into Eq. 9 yields the appropriate scattering rate. We see that for 783.4 nm this results in a predicted lifetime of $\sim$2 ms for -40 dB and $\sim$20 ms for -50 dB. For 781.2 nm trapping light, we calculate a lifetime of $\sim$1.3 ms for -33 dB and $\sim$31 ms for -47 dB. While both of these calculations appear to underestimate the measured trapping lifetime, we would like to point out that as the atom is heated in the trap, it will spend less time in the areas of high intensity and consequently see a reduced scattering rate. This, if included

122

in this model, would increase the predicted lifetime.

Second, we note that there is a large oscillation in the amplitude of resonant light versus wavelength (as seen in Fig. 58 (Bottom)). Although the frequency of the oscillation may not be correct due to aliasing (observed frequency is about twice the resolution bandwidth of the optical spectrum analyzer), we nevertheless point out that this oscillation would explain the observed sensitivity in trapping lifetime to the wavelength.

Indeed, we believe it is this pedestal that causes the poor lifetime in the traps produced with the free running diode laser. However, it is unlikely that this pedestal could be removed by filters when the trapping wavelength is only 1-5 nm detuned from atomic resonance. Even the most narrow of available interference filters typically offer a 3 dB bandwidth of several nm. However, an optical cavity could serve as a narrow filter, which could be tuned to eliminate the unwanted light at the resonance frequency. Alternatively, the trapping light could be passed through a heated, optically dense Rb cell to remove the unwanted resonant light. These additional experimental complications may make other laser systems, such as the one described in the next section, more attractive.

6.3 Ti:Sapphire FORT System

For most of the experiments in this thesis, a Schwartz Electro Optics *Titan* Ti:Sapphire laser, pumped originally by a 7 watt Coherent Argon-Ion Innova 200 provides dipole trapping light at 850 nm. We extract 1-2 W from this laser, which we then pass through two optical isolators (46 dB attn. each) and finally couple into a single SMPM optical fiber. The fiber delivers light to the experiment table where the light is then split into two beams, passed through separate AOM's and expanded with a 4.5x telescope. Each beam propagates 2.15 m to a 300 mm achromat where it is focused between the cavity mirrors. Two adjustment mirrors follow the final focusing lenses to allow positional and angular adjustment of each beam. A PZT stack on one mirror axis allows for fine control of the FORT position inside the cavity. A maximum of 200 mW can be delivered through the cavity, which produces a trap depth of 256 μK and a scattering rate of 7 s^{-1} at a 30 μm waist in the lattice configuration. The linewidth of this laser was measured to be 2 GHz giving a
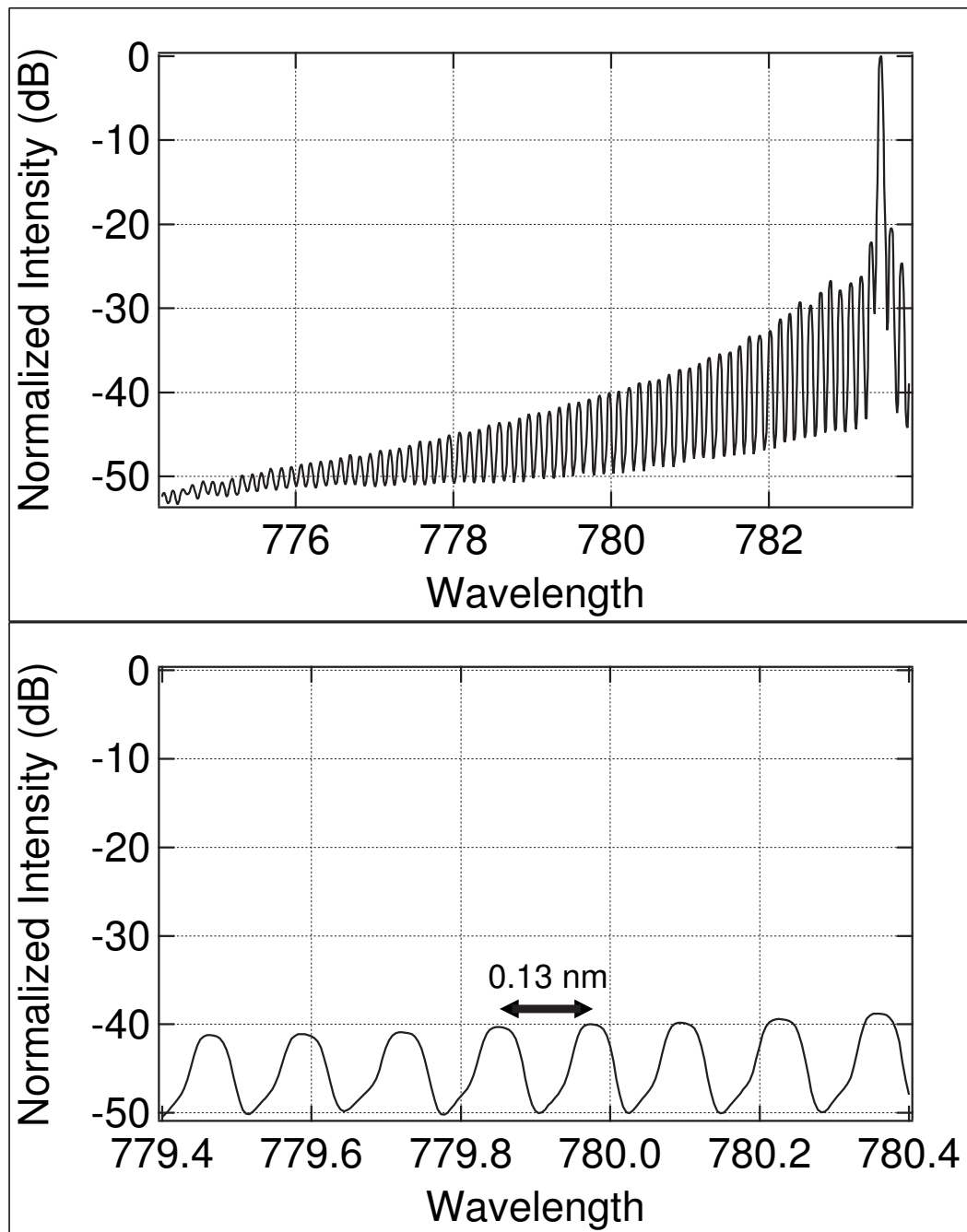
Figure 58: (Top) The broad spectral pedestal emitted by one of our laser diodes. (Bottom) Strong fluctuations with a period of ~0.13 nm make wavelength selection for the FORT very sensitive.

coherence length of 15 cm, which required us to make the path length of each arm equal.

The 10 fold increase in power induces considerable heating in the cavity mirrors, leading to drifting of the cavity resonance frequency during the experiment. This was minimized by spatial filtering of the beam in the telescope after the AOM's. Although the beam originates from an optical fiber, the spatial quality deteriorates inside the AOM, increasing the spot size of the focused beam inside the cavity. Achromats were selected to minimize spherical aberrations and extra care is taken while aligning these lenses. Nevertheless, we still observe considerable heating of the cavity mirrors.

The loading number and trap lifetime with this laser are shown in Fig. 59. We again observe an exponential decay in the number of atoms with a lifetime of 2.1 s in the traveling wave trap. This represents a thirty-fold improvement compared to the previous laser system. Unfortunately, this lifetime fell to only 104 ms if measured in the horizontal lattice configuration.

The difference in lifetimes between the traveling and standing wave configurations gives clues about the nature of the loss mechanism. The losses probably do not come from scattering, because this would be similar in both traps. Stiffening the optical components to reduce pointing instabilities also did not improve the lattice lifetime. If this had improved the system, it would have been counterintuitive because the trapping frequency along the propagation axis is typically much higher than acoustic frequencies and we do not observe such losses in the traveling wave that has frequency components susceptible to acoustic vibrations.

Other heating mechanisms could be ruled out by observation of the loss rate or by adjustment of experimental parameters. Thus, the exponential decay in atom number eliminates the possibility of density dependent losses. Furthermore, we were able to rule out losses due to photoassociative collisions by tuning the Ti:Sapp's wavelength over several nm while observing no significant effect on the lattice lifetime. In [125], the authors show a graph of losses due to such collisions to be very sensitive to wavelengths around 850 nm. Even though this experiment was performed with ^{85}Rb, we would expect similar results for ^{87}Rb.
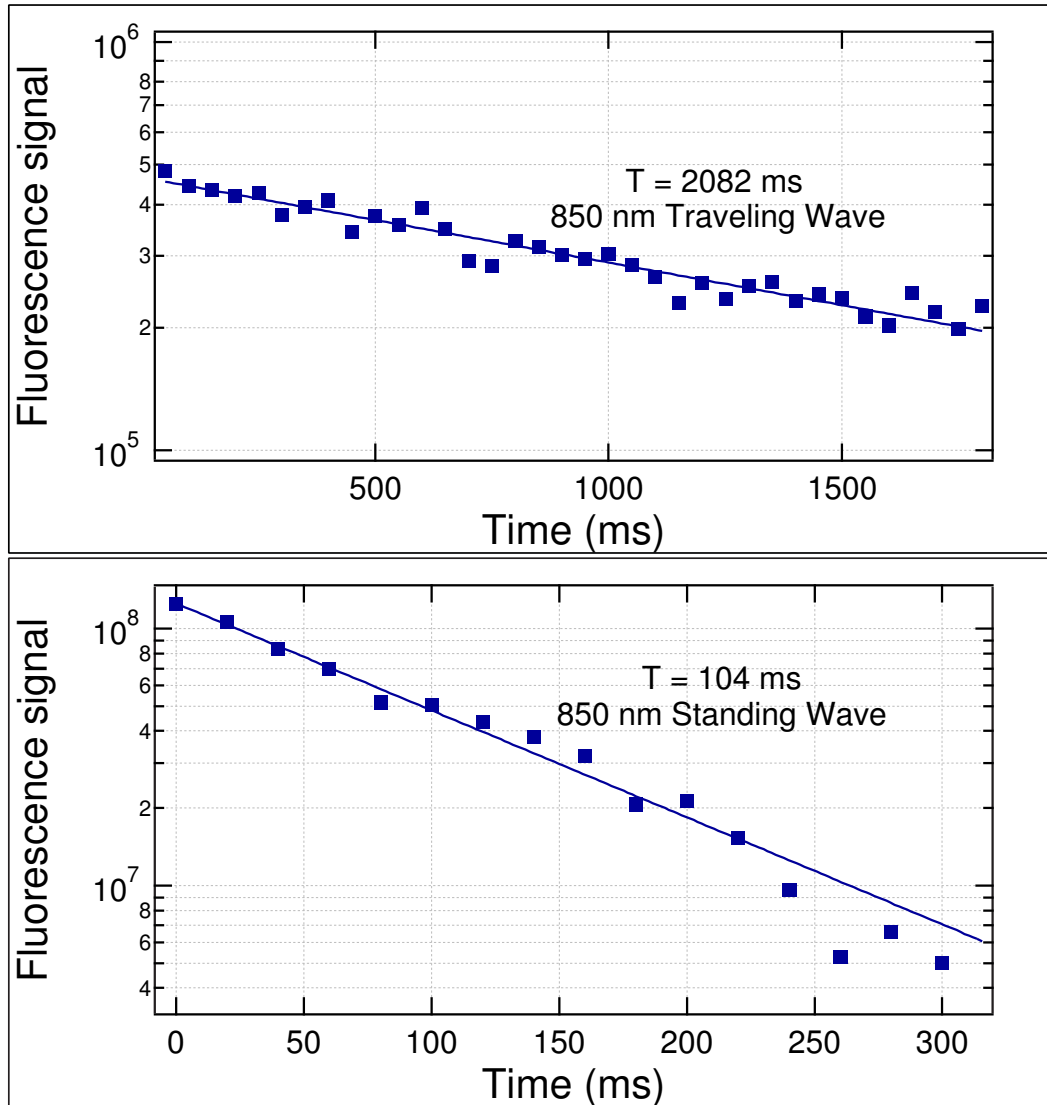
Figure 59: Lifetime of the FORT produced by the Ti:Sapp at 200 mW per beam. The top graph shows the lifetime observed in the horizontal traveling wave configuration, while the bottom graph shows the lifetime in the horizontal lattice configuration.
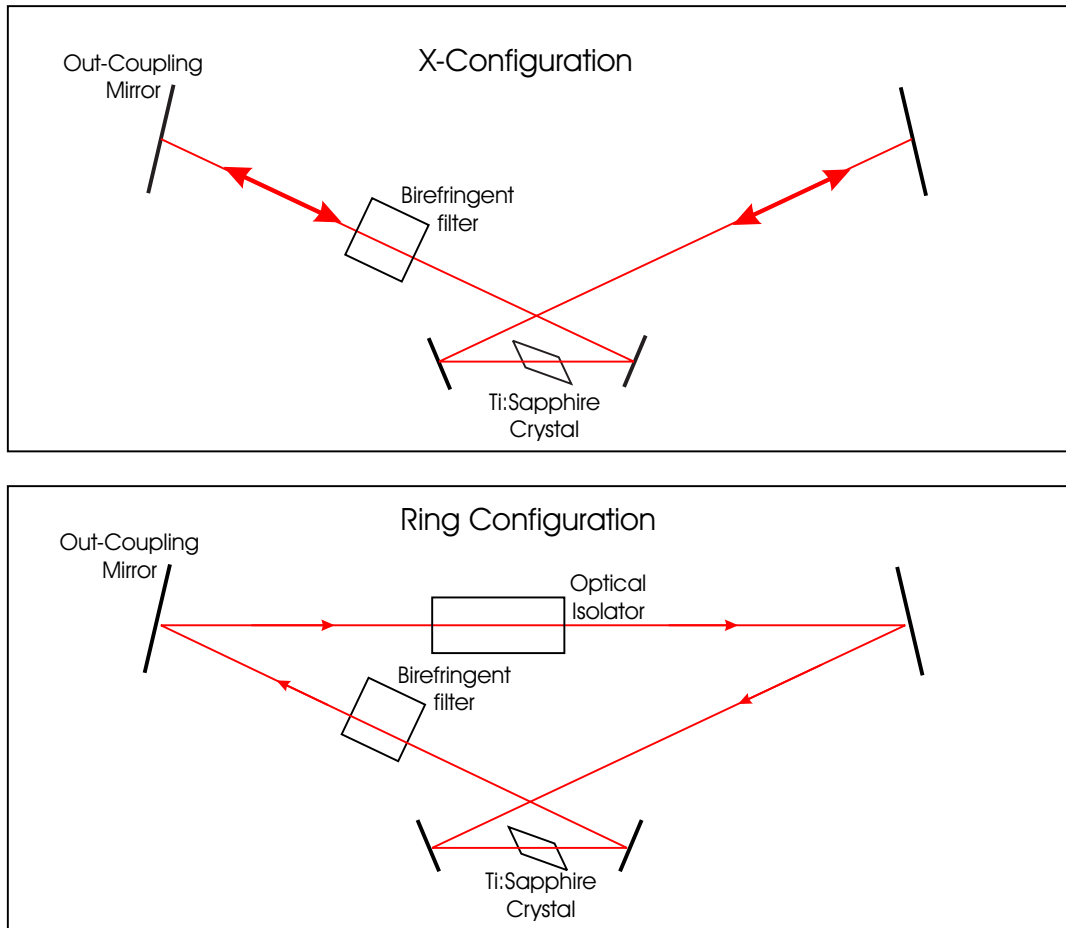
Figure 60: Two possible configurations of the Ti:Sapphire laser. The "X" configuration, shown on top, allows easy alignment and is more robust in daily operation. The "ring" configuration lowers the linewidth of the laser and increases its output power.

The most critical improvement of lattice lifetime came from an internal adjustment in the FORT laser. Our Ti:Sapphire laser can be operated in one of two separate configurations, shown in Fig. 60. In the "X" configuration, there is a standing wave inside the laser cavity which produces a system that is easier to set up and more tolerant to misalignment. In the "ring" configuration, there is a traveling wave inside the laser cavity which produces a system with increased output from 1 W to 2 W. Also, we measure a decrease in the linewidth from $\sim$2 GHz to $\sim$70 MHz. A very talented scientist working in the Georgia Tech Physics department named Mark Kimmel was kind enough to show us how to quickly swing this unfamiliar laser from the X to the ring configuration. In this configuration, the lifetime of the standing wave trap increased to $\sim$ 1.2 s.
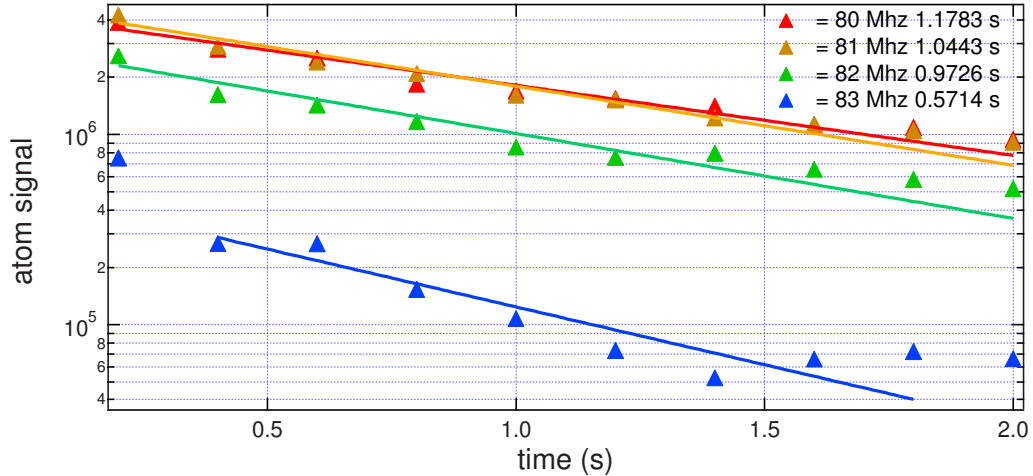
Figure 61: Lifetime dependence on AOM frequency. This data was taken with both AOMs set to the same frequency so the atoms remained stationary. Beam steering most likely caused the drop in lifetime.

Despite a tenfold improvement in lattice lifetime, the system was still unable to transport atoms 1.5 cm down to the cavity and back without the considerable losses seen in Fig. 52. A reduction in atom number to 1/7 of its original value is observed after transportation in only 250 ms. We investigated these losses by changing the frequencies of both AOMs to several different values, simulating deflection by the AOMs but holding the lattice stationary to make lifetime measurements. Although this did lower the lifetime, as seen in Fig. 61, it was not sufficient to explain the severe losses measured during transport. The decrease in lifetime observed here is most likely due to reduction in contrast caused by beam steering.

We also made investigations into the power spectrum of the FORT laser. Argon-Ion pump lasers are notorious for their high frequency intensity fluctuations, which show up as intensity fluctuations on the output of the Ti:Sapphire. Even though we did not measure these losses when the trap was stationary, it is possible that the atoms move through a resonance because the trap frequency changes during the transport process. This would cause losses via the mechanism described in section 6.1.2. The intensity fluctuations were thus measured using a high speed low noise power detector (EOT 3020) and a dynamic signal analyzer (see Fig. 62).

The intensity fluctuations of the Ti:Sapphire were reduced by introducing active intensity regulation. Here, an electro-optic modulator (EOM) in series with a Glan-Thompson

128

polarizing beam splitter cube quickly rotates the polarization of the light to adjust the output intensity. This "noise eater", a commercially available product from Con-Optics, reduces the intensity fluctuations by monitoring a portion of the output intensity and adjusting the voltage of the electro-optic modulator in a feedback loop with a bandwidth of 5 MHz. The reduction in intensity fluctuations of about 7 dB can be seen in Fig. 62. This improvement did not change the lattice lifetime, or the losses observed during transport in any significant fashion.

We were also able to borrow a Verdi-V5 solid state pump laser from Chandra Raman. These lasers exhibit much less intensity noise than Argon-Ion lasers, particularly at frequencies above 10 kHz. A comparison of this laser with both the regulated and unregulated Argon-Ion pump is shown in Fig. 62. Although this pump laser did not change the losses from the transport process, the lifetime in the standing wave did increase to over 2 seconds.

A New Chamber

Measuring the atomic temperature and trap frequencies of the lattice would shed light on the nature of our transport and heating problems. However, temperature measurement requires the release of atoms from the trap and imaging during free-expansion, which lowers the density of the atomic cloud and hence the fluorescent signal. Unfortunately, the cavity chamber is not designed for imaging of atoms, but rather for signals derived from the cavity itself. Its imaging port subtends a small solid angle, which made it impossible to collect enough light for temperature measurements.

We decided to build a new experiment in a new chamber to study the transport process in greater detail. This chamber has a much larger imaging port, and larger ports for MOT beams, which allow collection of many more atoms in the MOT [133]. Also, the chamber is larger and has no contents that would limit the baking temperature. This allows us to bake the chamber at a higher temperature and achieve a vacuum of below 10^{-10} Torr. An image of this chamber is shown in Fig. 63. For accurate comparison with previous measurements, the size of the FORT beam and the MOT loading and transfer parameters are the same as those used in the old chamber. We owe thanks to Chris Hamley for constructing this
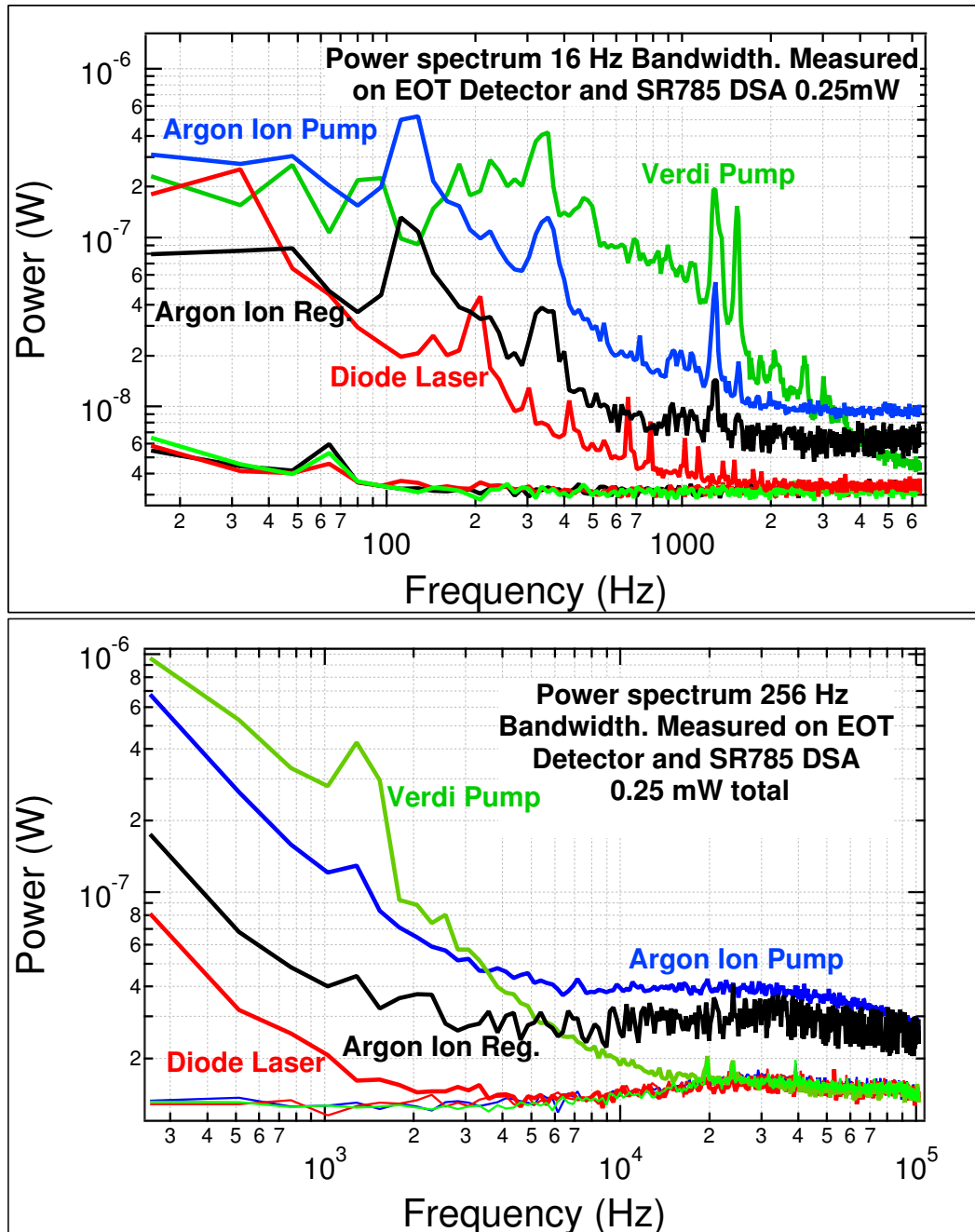
Figure 62: Power spectrum for the Ti:Sapphire at 850 nm pumped with the Argon-Ion, power regulated Argon-Ion, and the Verdi. The spectrum from a grating stabilized diode laser at 780 nm (the master MOT laser) is shows for comparison. The top graph shows the spectrum from 0.01 to 6.4 kHz, while the bottom graph shows the spectrum from 0.2 to 100 kHz. In each graph, 0.25 mW is incident upon an EOT 3020 low noise optical detector. At the bottom of each graph, a calibration curve of the noise floor made prior to each measurement shows the output of the detector with no light input.
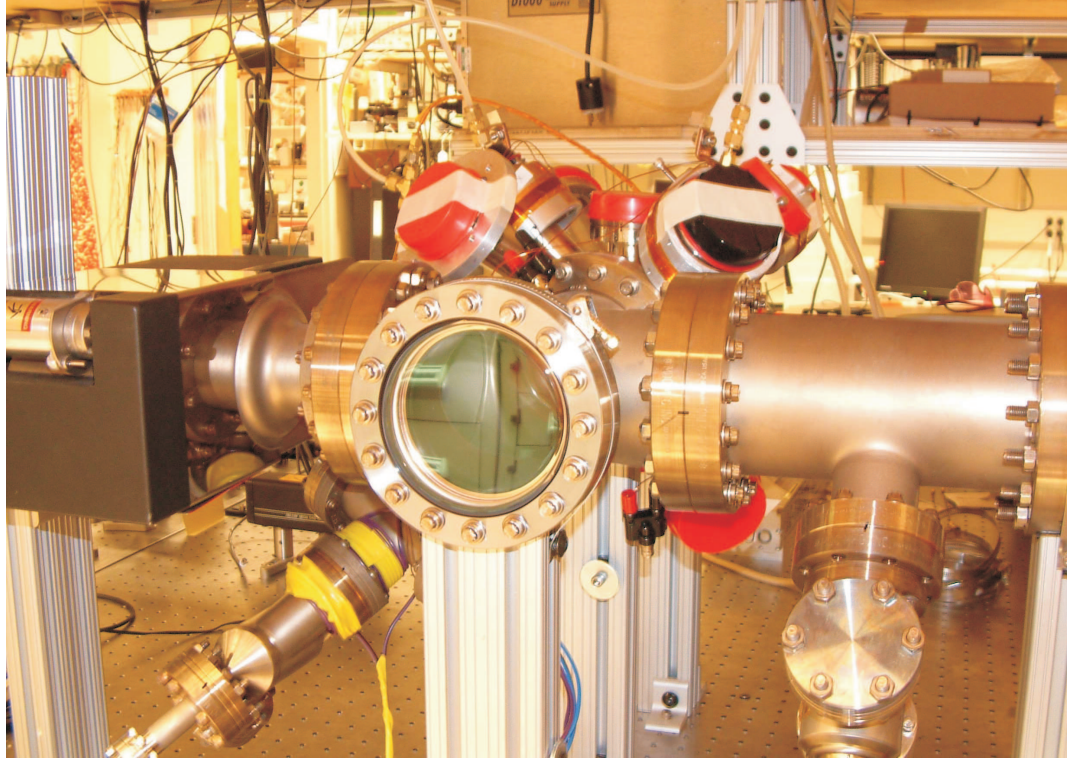
Figure 63: A schematic of the new chamber shown without optics or MOT coils. The large imaging ports allow much better optical access for imaging and temperature measurements. A large conductance to the ion pump increases pumping speed at the center of the chamber.

chamber as a project in our laboratory.

The lifetime of the traveling wave in the new chamber is an impressive 10 s! This is most likely due to better vacuum achieved through a higher pumping speed, higher bakeout temperature, inclusion of a Titanium-Sublimation pump, and no foreign objects inside the chamber (such as a cavity, Torr-Seal epoxy, and pieces of viton.) Also, the combination of a larger MOT ($3\text{-}5 \cdot 10^7$ atoms) and better imaging allows us to lower the power in the FORT beam and investigate the lifetime dependence. We verify that this lifetime does not depend on the power in the FORT beam (shown in Fig. 64).

We eliminated all unnecessary complications from this system by retro-reflecting the FORT light with a curved mirror to make a lattice. We also removed the AOMs used to shift the frequency, which also perturb the spatial beam quality. Once again, the observed lattice lifetime is measured to be ~ 1.3 s, similar to that of the old chamber. However, this chamber allows us to make new measurements on the lattice, including an extended trap
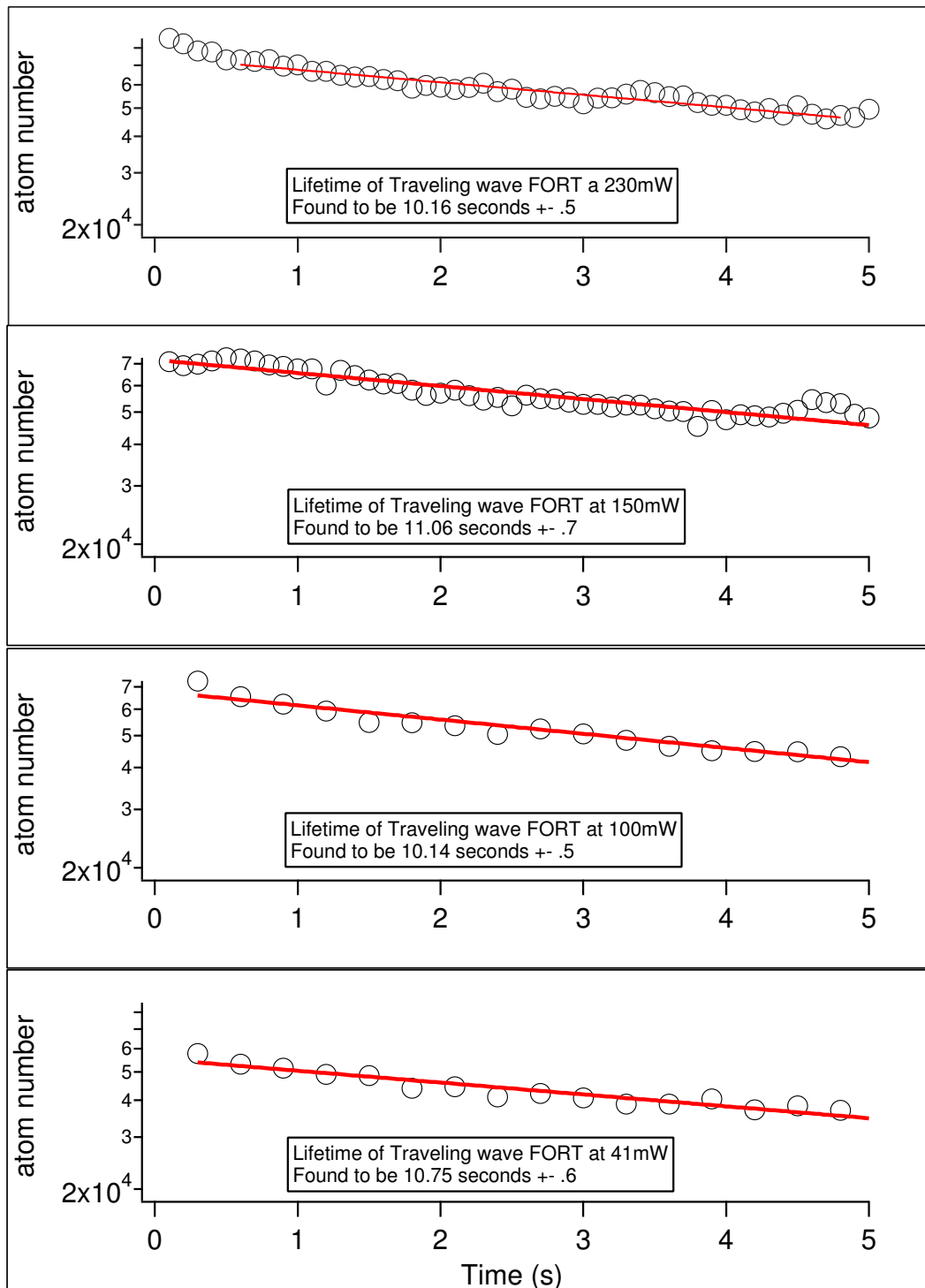
Figure 64: Atom number in traveling wave trap versus time for the new chamber. The lifetime does not depend on the power in the FORT laser beam.
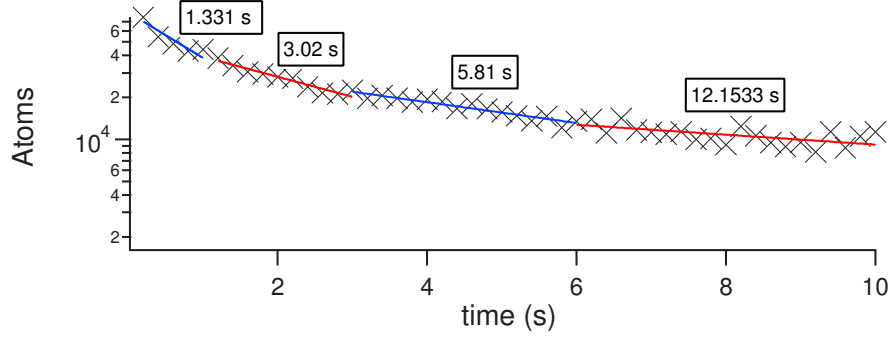
Figure 65: The lifetime of the lattice trap in the new chamber could be observed for up to ten seconds. We see that this data no longer fits an exponential curve. Approximate exponential lifetimes are shown for the different sections of the trap.

time observation, temperature measurements, and an evaluation of the trap frequency.

The improved imaging in the new chamber allows us to observe as little as 4000 atoms in the lattice trap. This extends the useful observation time of the lifetime measurement to over ten seconds. Fig. 65 shows a graph of the lifetime in this trap. We notice that this curve is no longer described by a simple exponential. Instead, there appears to be a high loss rate during the first second, followed by a reduced loss rate from one to ten seconds.

The temperature question could also be answered in the new chamber. We measured temperatures of the trapped atoms by releasing them from the lattice and allowing them to free expand. Fig. 66 shows a constant temperature of 67 μK throughout the periods of varying atomic loss. This data was taken with 360 mW per beam in the lattice, giving a calculated trap depth of 461 μK. This represents an $\eta = \frac{U}{k_b T}$ value of ~ 6.8.

Returning to Eq. 96, we see that if the temperature and thus the kinetic energy of the atoms remains constant, there must be an exponential decay in the number of atoms unless the trap heating is somehow dependent upon the number of atoms:

$$-N \langle \dot{E}_{heat} \rangle (N) = \frac{\partial E}{\partial N} \dot{N} \tag{101}$$

This means that we must have some density dependent losses, although the nature of this remains a mystery.

The trap frequency is important for characterizing the quality of the atomic conveyor
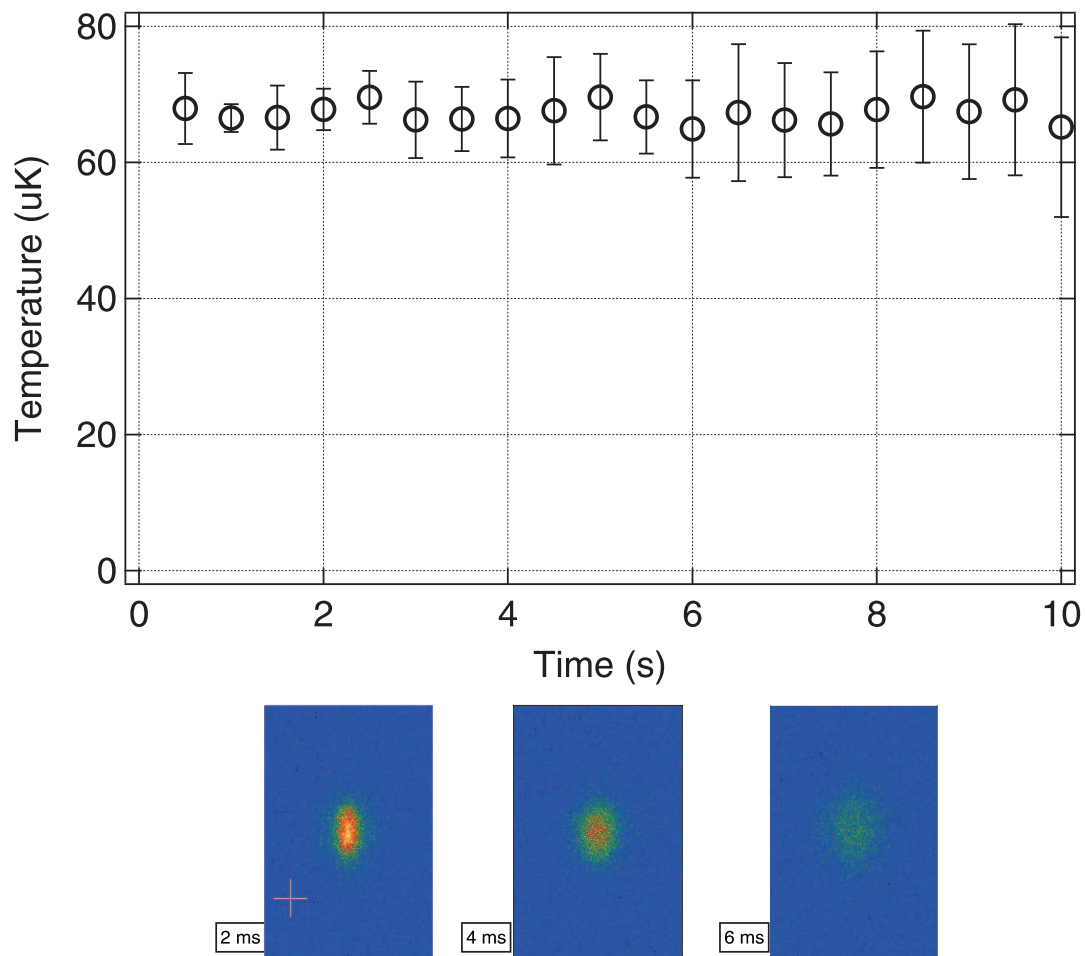
Figure 66: The temperature in the lattice is found to be constant throughout regions of varying atomic loss. The larger error bars at longer times indicate the decrease in SNR with low atom numbers. The images at the bottom of the graph indicate the quality of the imaging system in the new chamber. Here, only 20,000 atoms produce enough signal to make an accurate temperature measurement.
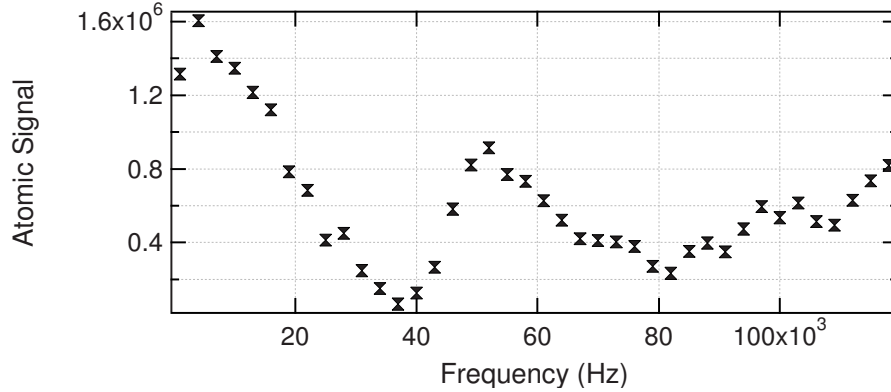
Figure 67: A parametric resonance at 39 kHz reveals that the trap frequency is much lower than expected.

belt. Indeed, this frequency sets a limit on how fast the atoms can be accelerated. We use parametric resonance to measure trap frequencies in out FORT. This is done by modulating the trap depth sinusoidally and recording the losses from the trap caused by the intensity fluctuations (as shown in section 6.1.2). Though the calculated trap frequency for this system along the z-axis should be ~ 350 kHz, we measure a resonance at only 39 kHz. This frequency is much too low for the axial direction, but also much too high for the radial direction, which should be 2.2 kHz. This result would most likely indicate that we have poor contrast in our standing wave. However, we independently measured a contrast over 90% in a Michelson-Morley interferometer where the path length difference was equal or longer than twice the distance from the center of the trap to the retro-reflecting mirror.

It was at this point when we concluded that there were simply too many unanswered questions and too many difficulties associated with this laser system. Furthermore, we did not wish to spend any more time studying a system that was subordinate to our primary goal. Moreover, the Meschede group had reported transportation of single atoms with great precision and high transportation efficiency using a Nd:YAG laser system [104]. Although the Nd:YAGs larger detuning (1064 nm versus 850 nm) offers a lower scattering rate, the thought of focusing the necessary 1.5 W through a 75 μm slit between mirrors that must be stabilized to femtometers was not particularly inviting. We thus decided on a different solid state laser system that is described in detail in the next section.

6.4   Twin TA FORT System

The final FORT laser system consists of an extended cavity diode laser at 850 nm and two tapered amplifiers (TA) (Toptica TA-100). We split 30 mW from the diode laser and shift it 80 MHz with two AOM's. It is then injected into the TA's which can output 500mW each with a seed power of 15 mW. An optical isolator prevents light from feeding back to the TAs in our standing wave configuration. Laser line filters (Omega Optical XL19) placed after the isolators suppress the diode pedestal background by > 60dB at the D1 and D2 lines. Optics after these filters are identical to those described in the previous section, including the spatial filters, focusing lenses, and adjustment mirrors. Approximately 250 mW per beam can be delivered to the center of the chamber, giving a trap depth of 320 μK and a scattering rate of 9 s^{-1} in the lattice configuration. This system has been tested with and without fibers inserted after the tapered amplifiers each producing identical results.

The placement of the AOMs before the TA's guarantee that the beam steering would not be a problem because the spatial mode coming out of the TA's is independent of the input beam. Instead, steering of the input beams by the AOMs simply changes the coupling and thus the output power of the TA's, but this amounts to less than 3% because of the close proximity to the modulators. Also, because optical fibers can be placed after the TA's, we expect a better spatial quality at the focus and thus less mirror heating.

In addition to the new laser system, we chose to build a third vacuum chamber. This vacuum chamber had a large imaging port like its predecessor, but with a main chamber that was only five inches off the optics table. This would ensure that we could avoid acrobatic optical setups, which might have induced pointing instabilities into the system. Huge MOT coils, necessary for the geometry of the chamber, could produce a magnetic field gradient that was strong enough to trap against gravity. This chamber also had a new "getter" source of Rb atoms. This consisted of a wire doped with Rb that would emit when conducting a nominal current. The getter source seems to perform well only when it is in immediate proximity to and directed at the location of the MOT. A schematic of the vacuum chamber and optics setup is shown in Fig. 69.

The third chamber offered similar atomic loading parameters to the second, with and
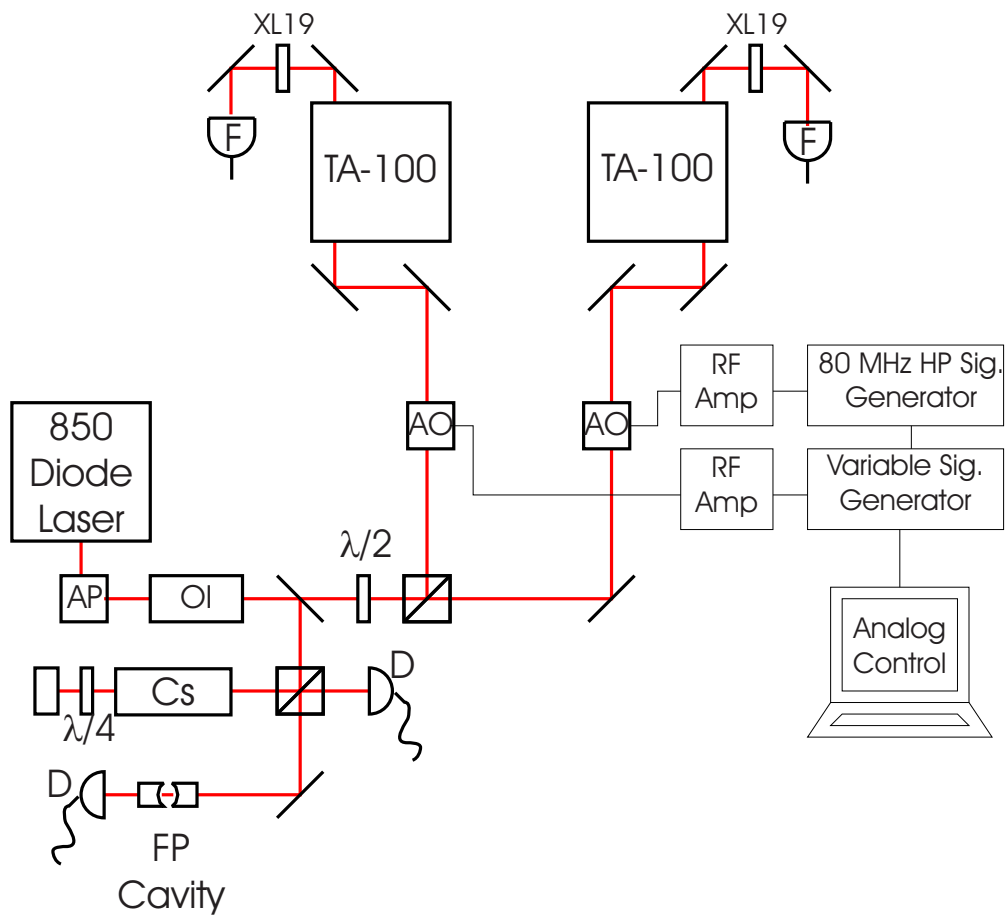
Figure 68: A schematic of the dual tapered amplifier FORT laser system. AP-Anamorphic Prism, OI-Optical Isolator, CS-Cesium Vapor Cell, FP-Scanning Fabry-Perot Interferometer, D-Thorlabs PDA55 optical detector, F-SMPM optical fiber, XL19-Laser line filters.
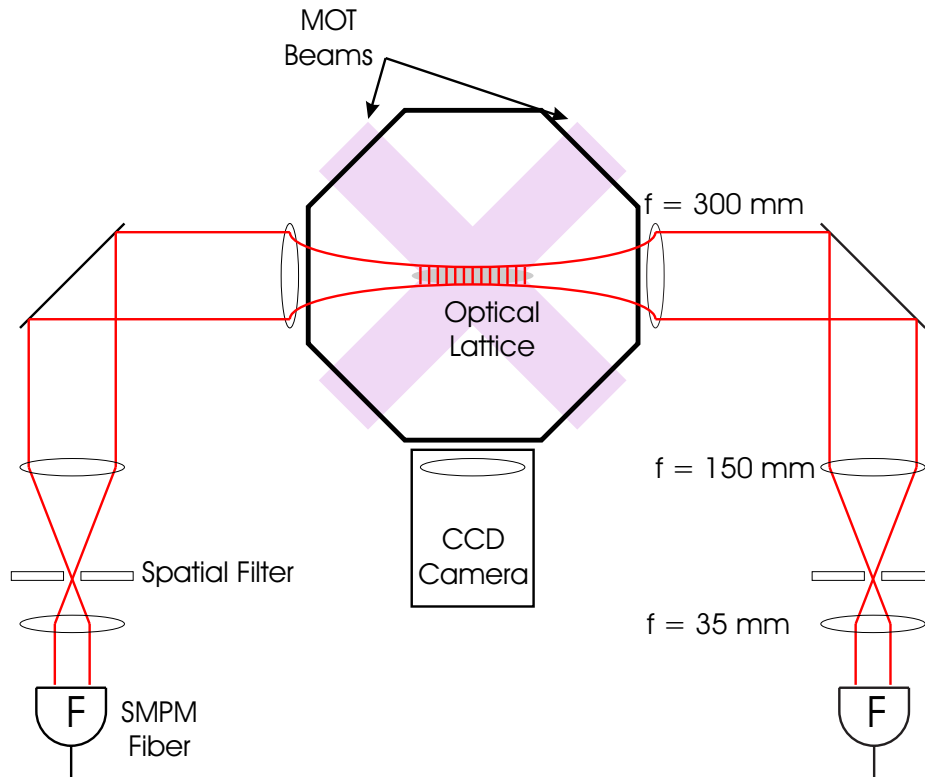
Figure 69: A schematic of the optical transport system with light from the TAs delivered in optical fibers.

atom number of $5 - 9 \cdot 10^7$ and a vacuum limited lifetime of >22 s. We measured the lifetime by producing the lab's first 3D magnetic trap (recall that the storage ring was a 2D magnetic *guide*). If the MOT coils in a chamber can produce the required magnetic field gradient, the magnetic trap allows for simple measurement of the upper limit on the vacuum limited lifetime.

The lifetime results in the new chamber were very positive. Fig. 70 shows a 19.5 s lifetime for the traveling wave and 5.5 s for the standing wave. This data was taken by summing the fluorescent signal from a 200 μs exposure for all atoms trapped in the FORT. Without the laser line filters centered at 850 nm, the lifetime in both configurations drops to only 0.5 s. We have measured the diode pedestal from the TA's at 780 nm to be at the -67 dB level using an optical spectrum analyzer with a 0.06 nm bandwidth. This would explain the drop in lifetime due to the scattering rate calculated from equation 100.

We also measure this lifetime to be very sensitive to adjustments in the seeding laser's
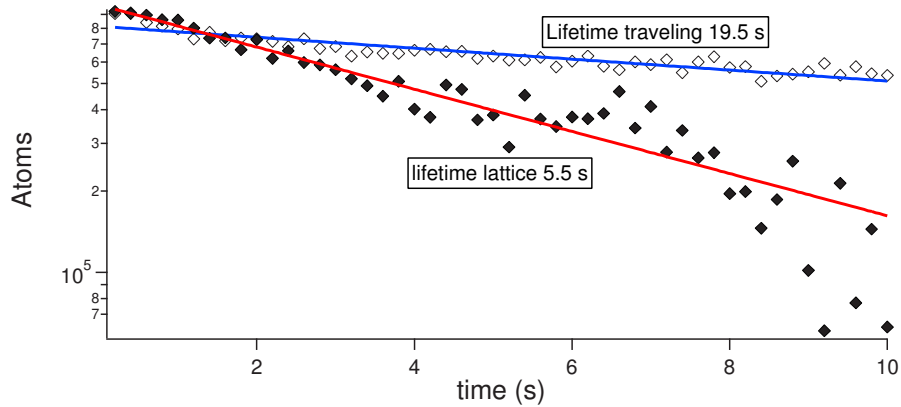
Figure 70: The lifetime in traveling and standing wave configurations with the TA system.

current. In particular, there are mode-hop free regions in the current setting that correspond to different lifetimes. Each of these regions is typically characterized by a certain wavelength and the regions differ in wavelength by ~ 0.015 nm in our system. It is well known that diode lasers exhibit a hysteresis with respect to adjustments of the drive current. Hysteresis causes some of the regions to overlap, so that two different lifetimes can correspond to the same current setting. This indicates that the lifetime dependency is probably not due to electronic noise in the current controller. Furthermore, the different lifetimes all correspond to single mode operation of the diode laser, measured by observing the transmission peaks on a scanning Fabry-Perot interferometer. We also cannot currently correlate the lifetime dependence to any change in the laser's linewidth, although we note that the linewidth of the Fabry-Perot interferometer at 850 nm corresponds to > 30 MHz, which is presumably much larger than the linewidth of the diode laser. Finally we note that we have also observed different lifetimes with vastly different current settings, but having the same wavelength. Even though this last comment seems to indicate that this effect is not wavelength dependant, we nevertheless give the "magic" wavelength here which produces the longest lifetimes and best transportation results (852.269 nm).

The atomic conveyor results were also very good. We simulated "quantum gate operations" by transporting atoms over a distance of 5 mm, where the next generation cavity would be located. We then moved the chain of occupied lattice sites back and forth over a distance of 115 μm. A time series of images spaced 5 ms apart shows the transport of

these atoms in Fig. 74. Here, a 1 ms exposure illuminates 200,000 atoms transported by the conveyor at 250 mW of FORT power and 852 nm. The oscillations at the end of this transport simulate introducing a chain of six individually addressable atoms into the cavity mode sixty times, or 360 single-bit operations. Of course, we did not have a cavity and the average occupation in each lattice site is 85 atoms. However, the losses of less than 2% of the total atom number during this process pose a very promising starting point for future experiments.

We measure the maximum transport distance of the atoms by moving at a constant velocity to a distance d, then reversing this velocity and returning to the atoms to the original position. The number of atoms remaining in the trap versus d is shown in Fig. 72. Each data point represents an average from 20 measurements. For this measurement, the power in the FORT beam is 250 mW. The probability to successfully transport atoms drops quickly after 8 mm. If the power is reduced to 200 mW, this value does not change. However, below 200 mW per beam, the maximum distance is reduced. We expect a fundamental limit in maximum transport distance where gravity reduces the trap depth to 0. The trap depth including gravity is given by:

$$U = U_0 \frac{w_0^2}{w(d)} e^{\frac{-2r^2}{w(d)^2}} + mgr \tag{102}$$

Where U_0 is the trap depth at the focus, and r is the radial distance from the optical axis. We have chosen the direction of $\mathbf{r}$ to be vertical. The waist w depends on the axial distance d from the center of the trap as:

$$w = w_0 \sqrt{1 + (d/d_r)^2} \tag{103}$$

Where d_r is the rayleigh range of the FORT beam. A plot of this potential with the inclusion of gravity is shown in Fig. 73. We see that at 15 μm the FORT can no longer support atoms against gravity. Our observed limit of 8 mm is lower than this calculated limit, but we note that imperfect contrast could lead to a lower limit. Also, the atoms are not at zero
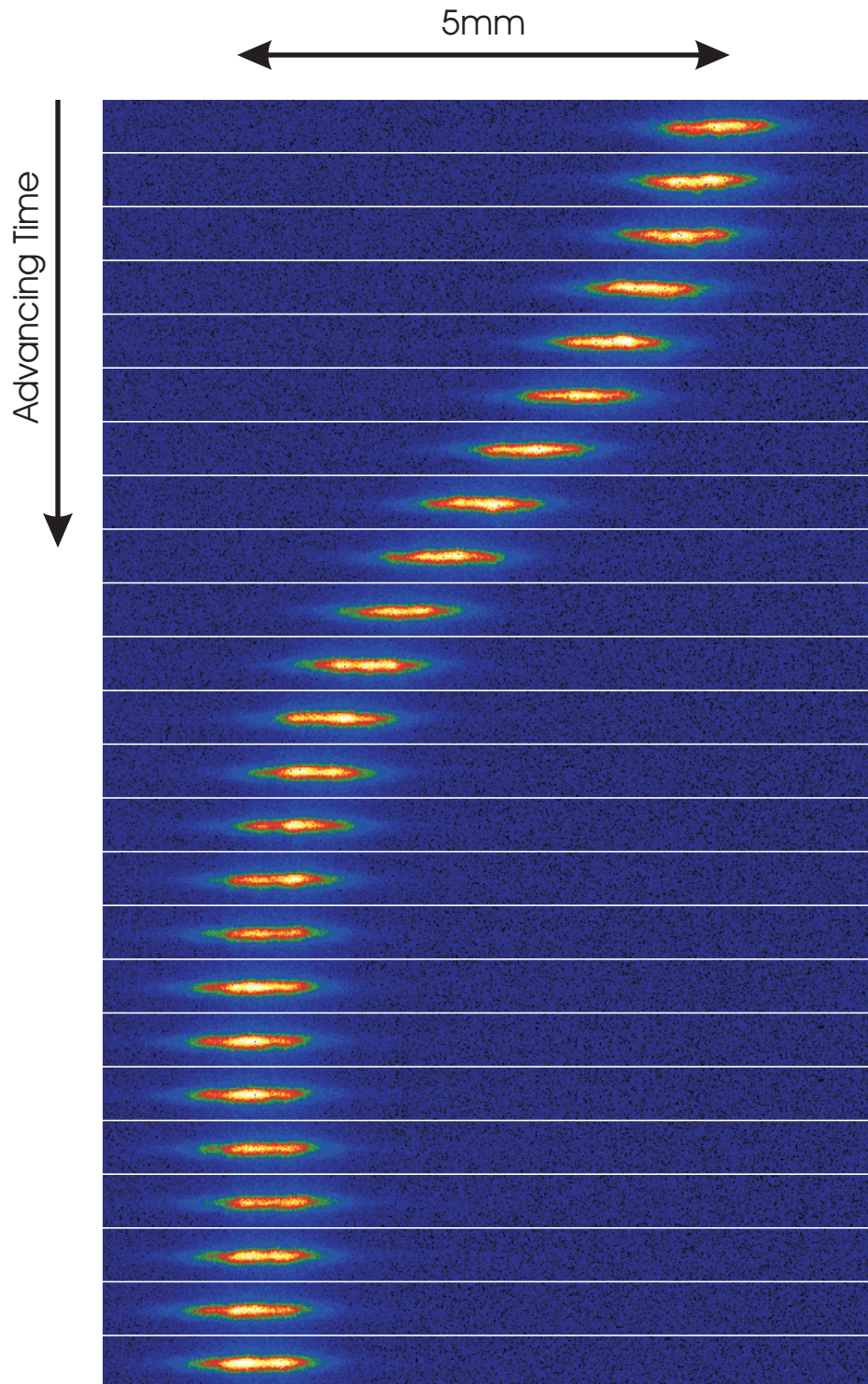
Figure 71: An image series of the atoms as they are transported over 5 mm, they then oscillate 60 times over a distance of 115 μm. The small oscillation can not be seen due to aliasing and imaging resolution. The images are spaced 5 ms apart. This was done to simulate delivery of the atoms to a cavity, and subsequent gate operations in the cavity.
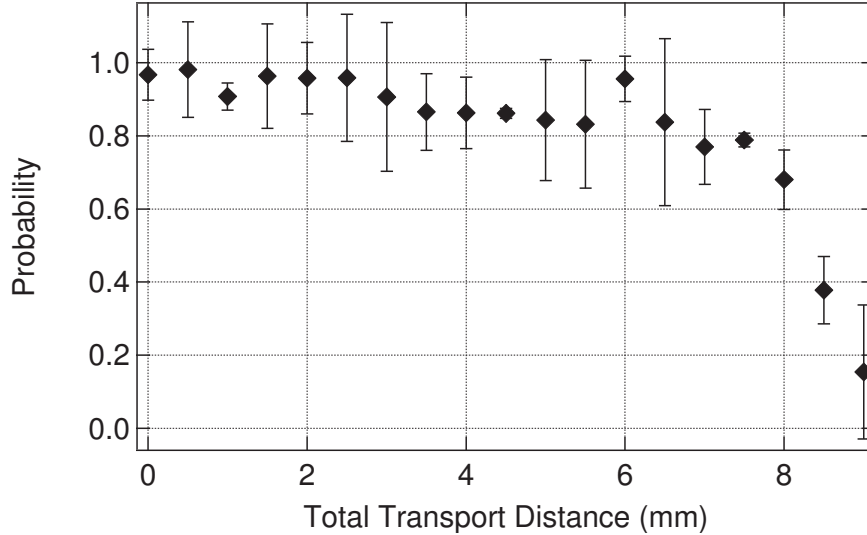
Figure 72: Probability to transport over a specified distance. Here, we transport the atomic cloud a known distance, return it to its original location and image the remaining atoms in the cloud.

temperature in the lattice so even the reduction in trap depth at 8 mm could be sufficient to reduce the transport probability.

We have also overcome the severe acceleration limit of the Ti:Sapphire transport system. Previously, we were limited to small accelerations ($< 4g$), which, when combined with our small transport lifetime, forced us chose a compromise between two loss mechanisms. Since we have made improvement in both of these mechanisms, we can now apply fast oscillations with large amplitudes as shown in Fig. 74. This would be necessary for example, to rapidly shuttle atoms between two optical cavities. Accelerations of up to 300 m/s are measured with very low losses. This value is limited by the bandwidth of the frequency modulation in our RF signal generator.

6.5 Summary of Atomic Positioning Experiment

We saw in chapter five, that a key limiting factor in the cavity system is the optical transport system. We have conducted an extensive study of the trapping characteristics of three different laser systems. The free-running diode system is found to resonantly excite the trapped atoms due to its broad pedestal of emitted wavelengths. The Ti:Sapphire system offers longer lifetime and allows us to demonstrate many of our results in cavity QED, in
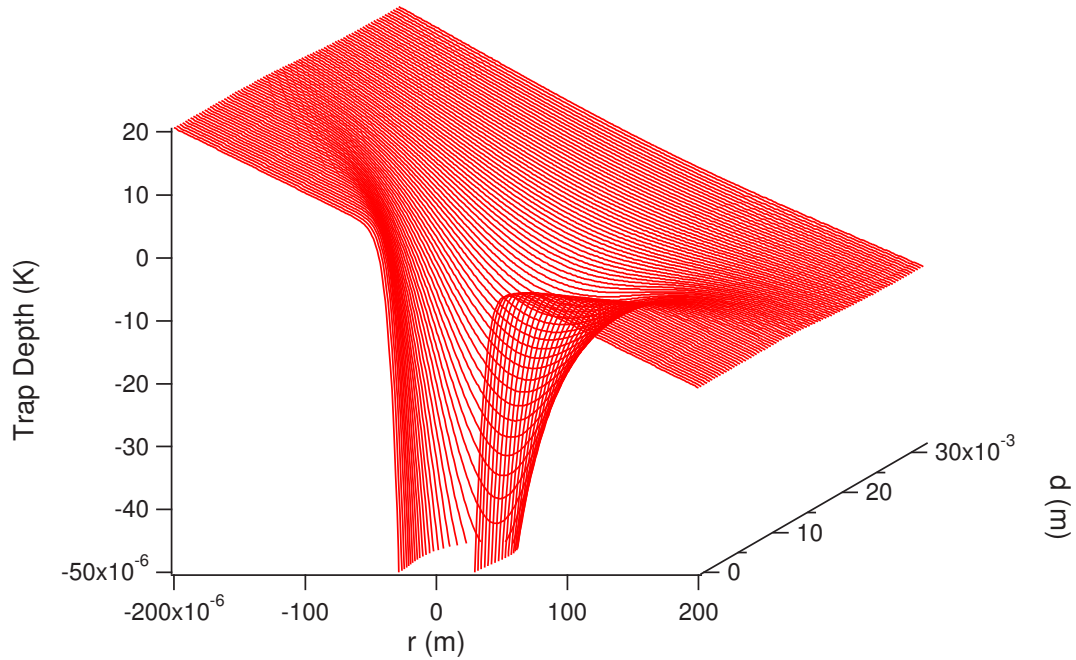
Figure 73: A theoretical plot of the trap depth of the lattice as modified by gravity. This was calculated for our experimental parameters of 250 mW per beam and a 30 μm waist. Trap depth is severely reduced at 12-15 mm from the focus.

spite of its observed losses during atomic transportation. The trap from this laser was found to have lower frequencies than expected, limiting both the acceleration and total travel distance of the atoms. Most recently, we employ a very successful tapered amplifier trapping system that offers a long lifetime and positional range. This system proves to be a very promising solution towards complete motional control of atoms in cavity QED.

6.6   Future Directions

There are many areas of improvement in this first generation experiment, a number of which are currently being implemented in the lab. We observe the need for a combination of higher rigidity and better damping for the cavity mount, as well as a reduction in the necessary drive voltage for the PZT active length stabilization. An imaging system capable of detecting single atoms should be constructed to provide overlap with detection through the cavity response. Also, the aforementioned off-resonant locking system should be made robust, to eliminate uncertainty during experimental runs. Finally, phase coherent generation of two
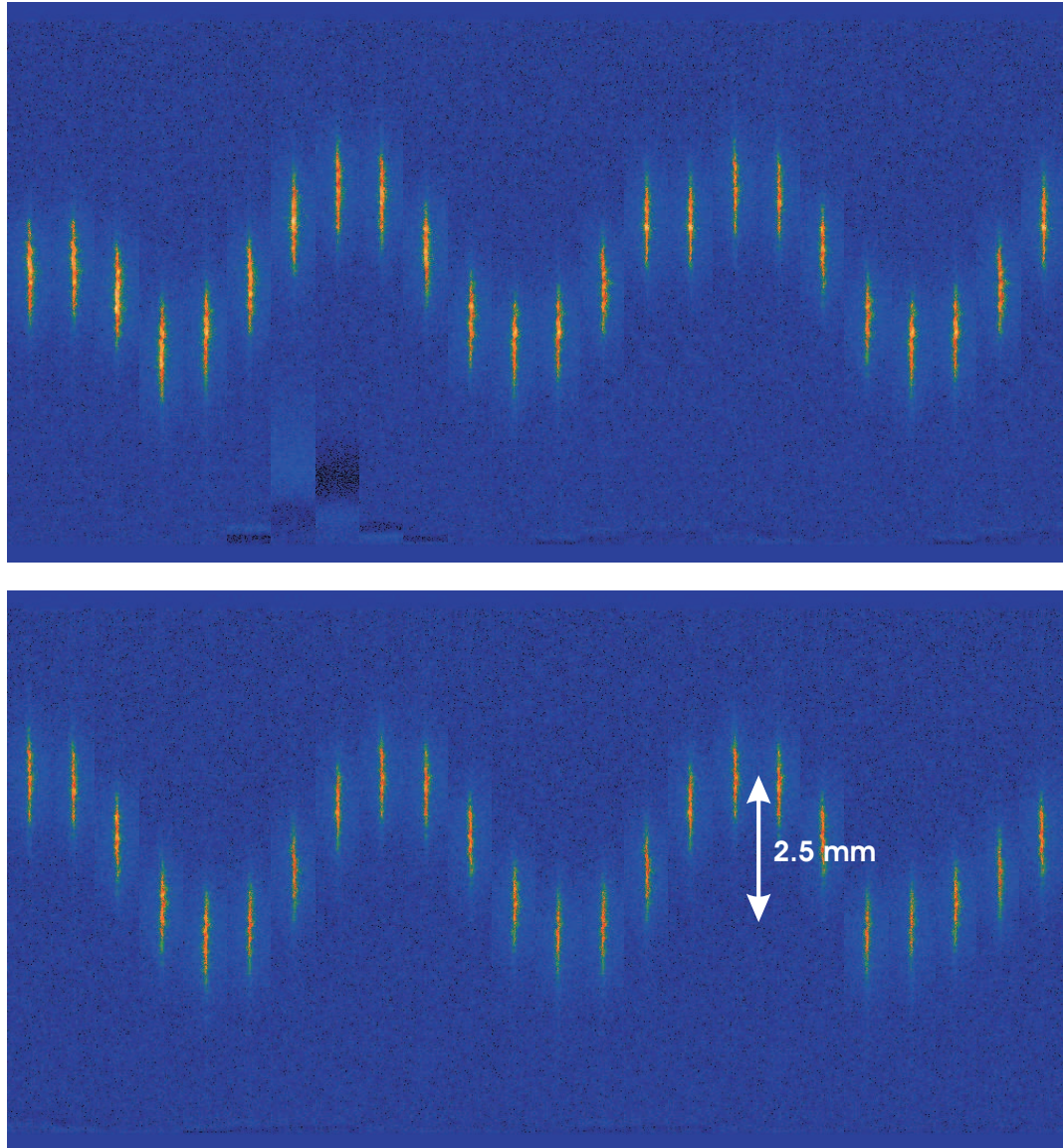
Figure 74: An image series shows many oscillations of the atoms in the optical conveyor. There is a 1 ms delay between each image.

different RF frequencies should be improved.

We have recently completed construction of a new cavity mount with improved rigidity. This mount is 5 cm long and made of a rectangular piece of solid oxygen-free copper that weighs 180 g (shown in Fig. 75). Springs, mounted in deep holes that run to the top of the mount, provide a suspension system with a frequency of $\nu_s = 7$ Hz. These holes lower the frequency via Eq. 72 by allowing larger extension of the springs into the mount's main body. A large cylindrical hole through the center of the mount allows FORT access in the horizontal direction. This hole narrows near the cavity so there is sufficient support for the PZT that controls the cavity length.

Additionally, a new cavity has been constructed. A summary of the cavity design parameters is given below:

$$l = 225 \ \mu m$$

$$r = 5 \ cm$$

$$\kappa = 2\pi \cdot 0.85 \cdot 10^6 \ \text{rad/s}$$

$$F = 400,000$$

$$g_0 = 2\pi \cdot 14 \cdot 10^6 \ \text{rad/s}$$

$$C_1 = 39$$

$$N_0 = 0.06$$

$$\tag{104}$$

The cavity length was chosen to avoid length fluctuations due to FORT laser heating. However, the increase in length narrows the linewidth of the cavity to $\kappa = 0.85$ MHz. We have locked the cavity to the resonant transition in ^{87}Rb, but there are frequency components in the transmission intensity that indicate fluctuations in the coupling between the probe laser and the cavity (shown in Fig. 76). A similar measurement of the laser frequency noise in the saturated absorption signal of ^{87}Rb shows that the main three peaks of this spectrum are caused by the laser itself. A new cavity laser should therefore be
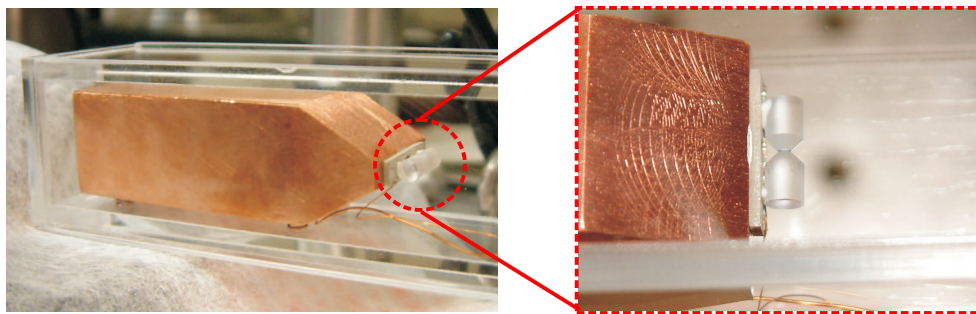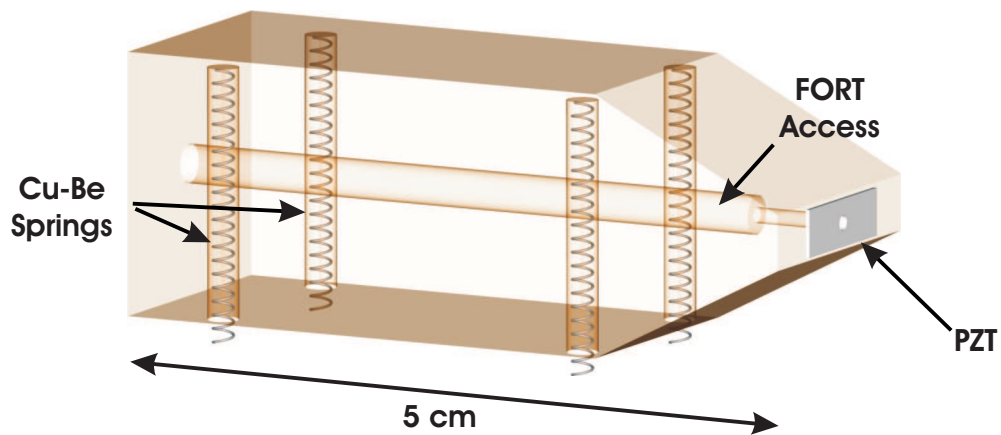
Figure 75: The top illustration shows the new cavity mount design. Springs inside the copper body provide vibration isolation, while the large footprint ratio increases rigidity. Holes drilled in the copper allow for access of the FORT beam and a PZT mounted on one end provides length control for the cavity mirrors. At the bottom are images of the completed mount and cavity construction. The image on the lower right shows the details of the cavity.

constructed to meet new linewidth requirements and reduce these noise fluctuations to a minimum.

A new imaging system with a large numerical aperture should be constructed so that we can independently verify the transportation of single atoms into the cavity. To this extent, we have designed a new glass cell vacuum chamber, also shown in Fig. 75, allowing superb optical access to the atoms in the FORT. The problem of scatter inside the walls of this glass cell must be reduced with spatial filtering or a new illumination geometry. One possibility is to couple red detuned near resonant light into the same fiber that delivers the FORT beam. This light scatters very little because it only contacts the glass far outside the imaging area. A dichroic mirror, reflecting 850 nm light, but passing 780 nm could be used to block the very intense FORT beam, while allowing imaging of the fluorescing atoms. Direct imaging of the atoms inside the cavity will not be possible due to the small solid angle defined by the cavity mirrors.

A new off-resonant locking system should be made to lock well within the cavity's linewidth and for long periods of time. The latter point is very important because this experiment involves many complex nontrivial systems that must all simultaneously function for successful implementation of the proposed quantum computing scheme. Even with a low failure probability rate per system p_f, the success decreases exponentially with the number n of these systems:

$$P_s = (1 - p_f)^n \tag{105}$$

This simple argument is indeed very powerful. We see that as the number of systems increases (we count 17 independent systems in our current setup) they must become extremely reliable. Furthermore, the diagnostics of one system can easily hinge upon results from another, cascading failures through the experiment and coupling the failure rates. This new locking technique is a perfect example of a complex system that must be made reliable to accelerate progress in other areas.

Finally, there is room for improvement in the RF signal generation for the FORT laser
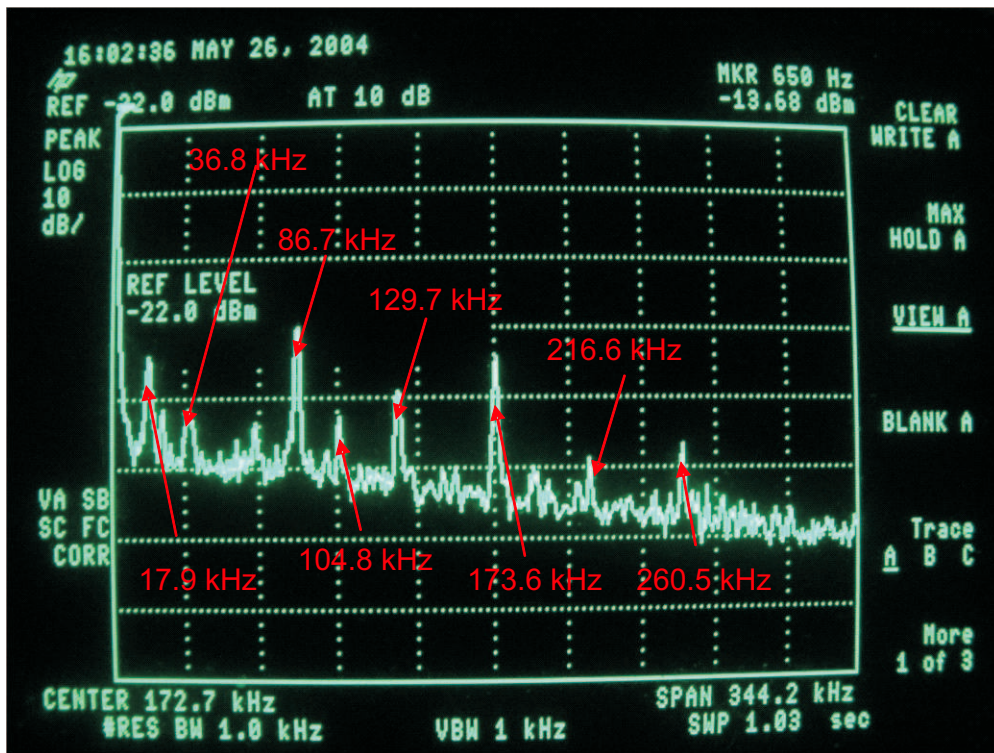
Figure 76: The transmission noise on the new cavity when locked is principally due to noise on the cavity laser.

AOMs. These AOMs must be driven with two phase coherent signals of different frequency. Furthermore, this difference frequency must be quickly and accurately adjusted over 1-3 MHz in less than 1 ms. Our current system can provide the necessary tuning range, but is limited by the input modulation bandwidth of the HP signal generator. We also measure phase noise in the beat signal between the two RF outputs as reported in [104]. It would be most desirable to obtain a signal generator that could be programmed in situ to perform a frequency ramp (this can be done with extremely low phase noise) that can be triggered by an external TTL input. Communications with Agilent Technologies lead us to believe that the HP / Agilent 83751A/B Synthesized Microwave Sweeper will perform programmed frequency ramps with low noise. However, this is a very expensive piece of equipment, and its purchase should be delayed until made necessary by progress in other portions of the experiment.

—-

Acronyms

AOM	Acousto-Optic Modulator
BEC	Bose-Einstein Condensate
CW	Continuous Wave (Refers to steady state operation, typically of lasers, rather than pulsed operation)
EOM	Electro Optic Modulator
FORT	Far Off Resonant Trap
FM	Frequency Modulation
FSR	Free Spectral Range
FWHM	Full Width Half Max
HWHM	Half Width Half Max
IGBT	Integrated Gate Bipolar Transistor
IR	Infrared: in this thesis this refers to the electromagnetic spectrum with λ=700-1800 nm
LO	Local Oscillator
MOT	Magneto-Optical Trap
PI	proportional-integral
PZT	Piezo-Electric Transducer (actually the acronym PZT comes from the crystal: Lead (**P**b), Ziroconate (**Z**), Titanate (**T**) used in the transducer)
RF	Radio Frequency. In this thesis, RF refers to frequencies above 5 MHz but below 10 GHz.
SA	Saturated Absorption
SMPM	Single Mode Polarization Maintaining
SNR	Signal-to-Noise Ratio
TEC	Thermo-Electric Cooler
UHV	Ultra-High Vacuum

REFERENCES

[1] D. Thompson, R. V. E. Lovelace, and D. M. Lee, "Storage-rings for spin-polarized hydrogen," *Journal of the Optical Society of America B-Optical Physics*, vol. 6, no. 11, pp. 2227–2234, 1989.

[2] W. Ketterle and D. E. Pritchard, "Trapping and focusing ground-state atoms with static fields," *Applied Physics B-Photophysics and Laser Chemistry*, vol. 54, no. 5, pp. 403–406, 1992.

[3] D. P. Katz, "A storage ring for polar molecules," *Journal of Chemical Physics*, vol. 107, no. 20, pp. 8491–8501, 1997.

[4] F. M. H. Crompvoets, H. L. Bethlem, R. T. Jongma, and G. Meijer, "A prototype storage ring for neutral molecules," *Nature*, vol. 411, no. 6834, pp. 174–176, 2001.

[5] D. W. Keith, C. R. Ekstrom, Q. A. Turchette, and D. E. Pritchard, "An interferometer for atoms," *Physical Review Letters*, vol. 66, no. 21, pp. 2693–2696, 1991.

[6] O. Carnal and J. Mlynek, "Youngs double-slit experiment with atoms - a simple atom interferometer," *Physical Review Letters*, vol. 66, no. 21, pp. 2689–2692, 1991.

[7] M. Kasevich and S. Chu, "Atomic interferometry using stimulated raman transitions," *Physical Review Letters*, vol. 67, no. 2, pp. 181–184, 1991.

[8] F. Riehle, T. Kisters, A. Witte, J. Helmcke, and C. J. Borde, "Optical ramsey spectroscopy in a rotating frame - sagnac effect in a matter-wave interferometer," *Physical Review Letters*, vol. 67, no. 2, pp. 177–180, 1991.

[9] T. L. Gustavson, P. Bouyer, and M. A. Kasevich, "Precision rotation measurements with an atom interferometer gyroscope," *Physical Review Letters*, vol. 78, no. 11, pp. 2046–2049, 1997.

[10] G. Moore, "Cramming more components onto integrated circuits," *Electronics*, vol. 38, no. 8, 1965.

[11] R. P. Feynman, "Simulating physics with computers," *International Journal of Theoretical Physics*, vol. 21, no. 6-7, pp. 467–488, 1982.

[12] D. Deutsch, "Quantum-theory, the church-turing principle and the universal quantum computer," *Proceedings of the Royal Society of London Series a-Mathematical Physical and Engineering Sciences*, vol. 400, no. 1818, pp. 97–117, 1985.

[13] P. Shor, "Proc. 35th annual symposium on the foundations of computer science," S. Goldwasser, Ed. IEEE Computer Society Press, Los Alamitos, California, 1994, p. 124.

[14] L. K. Grover, "Quantum mechanics helps in searching for a needle in a haystack," *Physical Review Letters*, vol. 79, no. 2, pp. 325–328, 1997.

[15] J. I. Cirac and P. Zoller, "Quantum computations with cold trapped ions," *Physical Review Letters*, vol. 74, no. 20, pp. 4091–4094, 1995.

[16] "Please visit http://qist.lanl.gov/ for a roadmap of quantum computing."

[17] M. E. Michelson A., *American Journal of Science*, vol. 34, no. 333, 1887.

[18] L. Marton, "Electron interferometer," *Physical Review*, vol. 85, no. 6, pp. 1057–1058, 1952.

[19] H. Maierleibnitz and T. Springer, "Ein interferometer fur iangsame neutronen," *Zeitschrift Fur Physik*, vol. 167, no. 4, p. 386, 1962.

[20] G. Sagnac, *Comptes Rendus*, vol. 157, no. 708, p. 1410, 1913.

[21] A. Lenef, T. D. Hammond, E. T. Smith, M. S. Chapman, R. A. Rubenstein, and D. E. Pritchard, "Rotation sensing with an atom interferometer," *Physical Review Letters*, vol. 78, no. 5, pp. 760–763, 1997.

[22] T. L. Gustavson, A. Landragin, and M. A. Kasevich, "Rotation sensing with a dual atom-interferometer sagnac gyroscope," *Classical and Quantum Gravity*, vol. 17, no. 12, pp. 2385–2398, 2000.

[23] O. Zobay and B. M. Garraway, "Controllable double waveguide for atoms," *Optics Communications*, vol. 178, no. 1-3, pp. 93–101, 2000.

[24] E. A. Hinds, C. J. Vale, and M. G. Boshier, "Two-wire waveguide and interferometer for cold atoms," *Physical Review Letters*, vol. 86, no. 8, pp. 1462–1465, 2001.

[25] W. Hansel, J. Reichel, P. Hommelhoff, and T. W. Hansch, "Trapped-atom interferometer in a magnetic microtrap," *Physical Review A*, vol. 6406, no. 6, pp. –, 2001.

[26] E. Andersson, T. Calarco, R. Folman, M. Andersson, B. Hessmo, and J. Schmiedmayer, "Multimode interferometer for guided matter waves," *Physical Review Letters*, vol. 88, no. 10, 2002.

[27] A. L. Migdall, J. V. Prodan, W. D. Phillips, T. H. Bergeman, and H. J. Metcalf, "1st observation of magnetically trapped neutral atoms," *Physical Review Letters*, vol. 54, no. 24, pp. 2596–2599, 1985.

[28] K. J. Kugler, K. Moritz, W. Paul, and U. Trinks, "Nestor - a magnetic storage ring for slow-neutrons," *Nuclear Instruments and Methods in Physics Research Section a-Accelerators Spectrometers Detectors and Associated Equipment*, vol. 228, no. 2-3, pp. 240–258, 1985.

[29] V. S. Bagnato, G. P. Lafyatis, A. G. Martin, E. L. Raab, R. N. Ahmadbitar, and D. E. Pritchard, "Continuous stopping and trapping of neutral atoms," *Physical Review Letters*, vol. 58, no. 21, pp. 2194–2197, 1987.

[30] R. Vanroijen, J. J. Berkhout, S. Jaakkola, and J. T. M. Walraven, "Experiments with atomic-hydrogen in a magnetic trapping field," *Physical Review Letters*, vol. 61, no. 8, pp. 931–934, 1988.

[31] H. F. Hess, G. P. Kochanski, J. M. Doyle, N. Masuhara, D. Kleppner, and T. J. Greytak, "Magnetic trapping of spin-polarized atomic-hydrogen," *Physical Review Letters*, vol. 59, no. 6, pp. 672–675, 1987.

[32] W. Petrich, M. H. Anderson, J. R. Ensher, and E. A. Cornell, "Stable, tightly confining magnetic trap for evaporative cooling of neutral atoms," *Physical Review Letters*, vol. 74, no. 17, pp. 3352–3355, 1995.

[33] K. B. Davis, M. O. Mewes, M. R. Andrews, N. J. Vandruten, D. S. Durfee, D. M. Kurn, and W. Ketterle, "Bose-einstein condensation in a gas of sodium atoms," *Physical Review Letters*, vol. 75, no. 22, pp. 3969–3973, 1995.

[34] M. D. Barrett, J. A. Sauer, and M. S. Chapman, "All-optical formation of an atomic bose-einstein condensate," *Physical Review Letters*, vol. 8701, no. 1, pp. art. no.– 010 404, 2001.

[35] J. Schmiedmayer, "A wire trap for neutral atoms," *Applied Physics B-Lasers and Optics*, vol. 60, no. 2-3, pp. 169–179, 1995.

[36] J. Denschlag, D. Cassettari, and J. Schmiedmayer, "Guiding neutral atoms with a wire," *Physical Review Letters*, vol. 82, no. 10, pp. 2014–2017, 1999.

[37] D. Muller, D. Z. Anderson, R. J. Grow, P. D. D. Schwindt, and E. A. Cornell, "Guiding neutral atoms around curves with lithographically patterned current-carrying wires," *Physical Review Letters*, vol. 83, no. 25, pp. 5194–5197, 1999.

[38] N. H. Dekker, C. S. Lee, V. Lorent, J. H. Thywissen, S. P. Smith, M. Drndic, R. M. Westervelt, and M. Prentiss, "Guiding neutral atoms on a chip," *Physical Review Letters*, vol. 84, no. 6, pp. 1124–1127, 2000.

[39] M. Key, I. G. Hughes, W. Rooijakkers, B. E. Sauer, E. A. Hinds, D. J. Richardson, and P. G. Kazansky, "Propagation of cold atoms along a miniature magnetic guide," *Physical Review Letters*, vol. 84, no. 7, pp. 1371–1373, 2000.

[40] B. K. Teo and G. Raithel, "Loading mechanism for atomic guides," *Physical Review A*, vol. 6303, no. 3, pp. –, 2001.

[41] D. Cassettari, B. Hessmo, R. Folman, T. Maier, and J. Schmiedmayer, "Beam splitter for guided atoms," *Physical Review Letters*, vol. 85, no. 26, pp. 5483–5487, 2000.

[42] D. Muller, E. A. Cornell, M. Prevedelli, P. D. D. Schwindt, A. Zozulya, and D. Z. Anderson, "Waveguide atom beam splitter for laser-cooled neutral atoms," *Optics Letters*, vol. 25, no. 18, pp. 1382–1384, 2000.

[43] W. Hansel, J. Reichel, P. Hommelhoff, and T. W. Hansch, "Magnetic conveyor belt for transporting and merging trapped atom clouds," *Physical Review Letters*, vol. 86, no. 4, pp. 608–611, 2001.

[44] E. Majorana, *Nuovo Cimento*, vol. 9, no. 43, 1932.

[45] R. Folman, P. Kruger, D. Cassettari, B. Hessmo, T. Maier, and J. Schmiedmayer, "Controlling cold atoms using nanofabricated surfaces: Atom chips," *Physical Review Letters*, vol. 84, no. 20, pp. 4749–4752, 2000.

[46] W. Hansel, P. Hommelhoff, T. W. Hansch, and J. Reichel, "Bose-einstein condensation on a microelectronic chip," *Nature*, vol. 413, no. 6855, pp. 498–501, 2001.

[47] J. Reichel, W. Hansel, P. Hommelhoff, and T. W. Hansch, "Applications of integrated magnetic microtraps," *Applied Physics B-Lasers and Optics*, vol. 72, no. 1, pp. 81–89, 2001.

[48] J. Prodan, A. Migdall, W. D. Phillips, I. So, H. Metcalf, and J. Dalibard, "Stopping atoms with laser-light," *Physical Review Letters*, vol. 54, no. 10, pp. 992–995, 1985.

[49] S. Chu, L. Hollberg, J. E. Bjorkholm, A. Cable, and A. Ashkin, "3-dimensional viscous confinement and cooling of atoms by resonance radiation pressure," *Physical Review Letters*, vol. 55, no. 1, pp. 48–51, 1985.

[50] H. J. Metcalf and P. Van der Straten, *Laser cooling and trapping*, ser. Graduate texts in contemporary physics. New York: Springer, 1999.

[51] J. P. Gordon and A. Ashkin, "Motion of atoms in a radiation trap," *Physical Review A*, vol. 21, no. 5, pp. 1606–1617, 1980.

[52] K. Lindquist, M. Stephens, and C. Wieman, "Experimental and theoretical-study of the vapor-cell zeeman optical trap," *Physical Review A*, vol. 46, no. 7, pp. 4082–4090, 1992.

[53] K. E. Gibble, S. Kasapi, and S. Chu, "Improved magnetooptic trapping in a vapor cell," *Optics Letters*, vol. 17, no. 7, pp. 526–528, 1992.

[54] T. Walker, D. Sesko, and C. Wieman, "Collective behavior of optically trapped neutral atoms," *Physical Review Letters*, vol. 64, no. 4, pp. 408–411, 1990.

[55] D. Sesko, T. Walker, C. Monroe, A. Gallagher, and C. Wieman, "Collisional losses from a light-force atom trap," *Physical Review Letters*, vol. 63, no. 9, pp. 961–964, 1989.

[56] M. H. Anderson, W. Petrich, J. R. Ensher, and E. A. Cornell, "Reduction of light-assisted collisional loss rate from a low-pressure vapor-cell trap," *Physical Review A*, vol. 50, no. 5, pp. R3597–R3600, 1994.

[57] C. G. Townsend, N. H. Edwards, K. P. Zetie, C. J. Cooper, J. Rink, and C. J. Foot, "High-density trapping of cesium atoms in a dark magneto-optical trap," *Physical Review A*, vol. 53, no. 3, pp. 1702–1714, 1996.

[58] P. D. Lett, R. N. Watts, C. I. Westbrook, W. D. Phillips, P. L. Gould, and H. J. Metcalf, "Observation of atoms laser cooled below the doppler limit," *Physical Review Letters*, vol. 61, no. 2, pp. 169–172, 1988.

[59] M. Barrett, "A quest for bec: An all optical alternative," Ph.D. dissertation, Georgia Institute of Technology, 2002.

[60] K. B. Macadam, A. Steinbach, and C. Wieman, "A narrow-band tunable diode-laser system with grating feedback, and a saturated absorption spectrometer for cs and rb," *American Journal of Physics*, vol. 60, no. 12, pp. 1098–1111, 1992.

[61] K. G. Libbrecht, R. A. Boyd, P. A. Willems, T. L. Gustavson, and D. K. Kim, "Teaching physics with 670-nm diode-lasers - construction of stabilized lasers and lithium cells," *American Journal of Physics*, vol. 63, no. 8, pp. 729–737, 1995.

[62] C. C. Bradley, J. Chen, and R. G. Hulet, "Instrumentation for the stable operation of laser-diodes," *Review of Scientific Instruments*, vol. 61, no. 8, pp. 2097–2101, 1990.

[63] K. G. Libbrecht and J. L. Hall, "A low-noise high-speed diode-laser current controller," *Review of Scientific Instruments*, vol. 64, no. 8, pp. 2133–2135, 1993.

[64] A. E. Siegman, *Lasers*. Mill Valley, CA.: University Science Books, 1986.

[65] P. Horowitz and W. Hill, *The art of electronics*, 2nd ed. Cambridge [England] ; New York: Cambridge University Press, 1989.

[66] P. D. D. Schwindt, "Magnetic traps and guides for bose-einstein condensates on an atom chip: Progress toward a coherent atom waveguide beamsplitter," Ph.D. dissertation, Iniversity of Colorado, 2003.

[67] W. Ketterle, D. S. Durfee, and D. M. Stamper-Kurn, "Making, probing, and understanding bose-einstein condensates," *cond-mat*, p. 9904034, 1999.

[68] D. S. Weiss, E. Riis, Y. Shevy, P. J. Ungar, and S. Chu, "Optical molasses and multilevel atoms - experiment," *Journal of the Optical Society of America B-Optical Physics*, vol. 6, no. 11, pp. 2072–2083, 1989.

[69] J. F. O'Hanlon, *A user's guide to vacuum technology*, 2nd ed. New York: Wiley, 1989.

[70] P. Cren, C. F. Roos, A. Aclan, J. Dalibard, and D. Guery-Odelin, "Loading of a cold atomic beam into a magnetic guide," *European Physical Journal D*, vol. 20, no. 1, pp. 107–116, 2002.

[71] A. Einstein, B. Podolsky, and N. Rosen, *Physical Review*, vol. 47, p. 777, 1935.

[72] J. S. Bell, "On problem of hidden variables in quantum mechanics," *Reviews of Modern Physics*, vol. 38, no. 3, p. 447, 1966.

[73] W. H. Zurek, "Decoherence and the transition from quantum to classical," *Physics Today*, vol. 44, no. 10, pp. 36–44, 1991.

[74] C. Monroe, D. M. Meekhof, B. E. King, W. M. Itano, and D. J. Wineland, "Demonstration of a fundamental quantum logic gate," *Physical Review Letters*, vol. 75, no. 25, pp. 4714–4717, 1995.

[75] Q. A. Turchette, C. J. Hood, W. Lange, H. Mabuchi, and H. J. Kimble, "Measurement of conditional phase-shifts for quantum logic," *Physical Review Letters*, vol. 75, no. 25, pp. 4710–4713, 1995.

[76] Q. A. Turchette, C. S. Wood, B. E. King, C. J. Myatt, D. Leibfried, W. M. Itano, C. Monroe, and D. J. Wineland, "Deterministic entanglement of two trapped ions," *Physical Review Letters*, vol. 81, no. 17, pp. 3631–3634, 1998.

[77] H. Mabuchi, Q. A. Turchette, M. S. Chapman, and H. J. Kimble, "Real-time detection of individual atoms falling through a high-finesse optical cavity," *Optics Letters*, vol. 21, no. 17, pp. 1393–1395, 1996.

[78] C. J. Hood, M. S. Chapman, T. W. Lynn, and H. J. Kimble, "Real-time cavity qed with single atoms," *Physical Review Letters*, vol. 80, no. 19, pp. 4157–4160, 1998.

[79] P. Munstermann, T. Fischer, P. Maunz, P. W. H. Pinkse, and G. Rempe, "Dynamics of single-atom motion observed in a high-finesse cavity," *Physical Review Letters*, vol. 82, no. 19, pp. 3791–3794, 1999.

[80] J. Ye, D. W. Vernooy, and H. J. Kimble, "Trapping of single atoms in cavity qed," *Physical Review Letters*, vol. 83, no. 24, pp. 4987–4990, 1999.

[81] C. J. Hood, T. W. Lynn, A. C. Doherty, A. S. Parkins, and H. J. Kimble, "The atom-cavity microscope: Single atoms bound in orbit by single photons," *Science*, vol. 287, no. 5457, pp. 1447–1453, 2000.

[82] P. W. H. Pinkse, T. Fischer, P. Maunz, and G. Rempe, "Trapping an atom with single photons," *Nature*, vol. 404, no. 6776, pp. 365–368, 2000.

[83] J. McKeever, J. R. Buck, A. D. Boozer, A. Kuzmich, H. C. Nagerl, D. M. Stamper-Kurn, and H. J. Kimble, "State-insensitive cooling and trapping of single atoms in an optical cavity," *Physical Review Letters*, vol. 90, no. 13, 2003.

[84] T. Fischer, P. Maunz, P. W. H. Pinkse, T. Puppe, and G. Rempe, "Feedback on the motion of a single atom in an optical cavity," *Physical Review Letters*, vol. 88, no. 16, 2002.

[85] A. Kuhn, M. Hennrich, and G. Rempe, "Deterministic single-photon source for distributed quantum networking," *Physical Review Letters*, vol. 89, no. 6, pp. –, 2002.

[86] J. McKeever, A. Boca, A. D. Boozer, R. Miller, J. R. Buck, A. Kuzmich, and H. J. Kimble, "Deterministic generation of single photons from one atom trapped in a cavity," *Science*, vol. 303, no. 5666, pp. 1992–1994, 2004.

[87] M. S. Chapman, L. You, and T. A. B. Kennedy, "Proposal for aro/nsa grant g-41-z05 (unpublished)."

[88] T. Pellizzari, S. A. Gardiner, J. I. Cirac, and P. Zoller, "Decoherence, continuous observation, and quantum computing - a cavity qed model," *Physical Review Letters*, vol. 75, no. 21, pp. 3788–3791, 1995.

[89] L. You, X. X. Yi, and X. H. Su, "Quantum logic between atoms inside a high-q optical cavity," *Physical Review A*, vol. 67, no. 3, pp. –, 2003.

[90] X. X. Yi, X. H. Su, and L. You, "Conditional quantum phase gate between two 3-state atoms," *Physical Review Letters*, vol. 90, no. 9, pp. –, 2003.

[91] P. R. Berman, *Cavity quantum electrodynamics.* Boston: Academic Press, 1994.

[92] H. Walther, "Generation and detection of fock-states of the radiation field," *Zeitschrift Fur Naturforschung Section a-a Journal of Physical Sciences*, vol. 56, no. 1-2, pp. 117–123, 2001.

[93] J. M. Raimond, M. Brune, and S. Haroche, "Colloquium: Manipulating quantum entanglement with atoms and photons in a cavity," *Reviews of Modern Physics*, vol. 73, no. 3, pp. 565–582, 2001.

[94] H. Mabuchi and A. C. Doherty, "Cavity quantum electrodynamics: Coherence in context," *Science*, vol. 298, no. 5597, pp. 1372–1377, 2002.

[95] H. Walther, "Generation of photon number states on demand," *Fortschritte Der Physik-Progress of Physics*, vol. 51, no. 4-5, pp. 521–530, 2003.

[96] E. T. Jaynes and F. W. Cummings, "Comparison of quantum and semiclassical radiation theories with application to beam maser," *Proceedings of the Ieee*, vol. 51, no. 1, p. 89, 1963.

[97] C. J. Hood, "Real-time measurments and trapping of single atoms by single photons," Ph.D. dissertation, California Inst. of Technology, 2000.

[98] H. M. Gibbs, S. L. Mccall, and T. N. C. Venkatesan, "Differential gain and bistability using a sodium-filled fabry-perot-interferometer," *Physical Review Letters*, vol. 36, no. 19, pp. 1135–1138, 1976.

[99] A. T. Rosenberger, L. A. Orozco, H. J. Kimble, and P. D. Drummond, "Absorptive optical bistability in 2-state atoms," *Physical Review A*, vol. 43, no. 11, pp. 6284–6302, 1991.

[100] S. Chu, J. E. Bjorkholm, A. Ashkin, and A. Cable, "Experimental-observation of optically trapped atoms," *Physical Review Letters*, vol. 57, no. 3, pp. 314–317, 1986.

[101] S. Kuhr, W. Alt, D. Schrader, M. Muller, V. Gomer, and D. Meschede, "Deterministic delivery of a single atom," *Science*, vol. 293, no. 5528, pp. 278–280, 2001.

[102] R. Grimm, M. Weidemuller, and Y. B. Ovchinnikov, "Optical dipole traps for neutral atoms," *Advances in Atomic Molecular, and Optical Physics, Vol. 42*, vol. 42, pp. 95–170, 2000.

[103] J. D. Jackson, *Classical electrodynamics*, 3rd ed. New York: Wiley, 1999.

[104] D. Schrader, S. Kuhr, W. Alt, M. Muller, V. Gomer, and D. Meschede, "An optical conveyor belt for single neutral atoms," *Applied Physics B-Lasers and Optics*, vol. 73, no. 8, pp. 819–824, 2001.

[105] S. J. M. Kuppens, K. L. Corwin, K. W. Miller, T. E. Chupp, and C. E. Wieman, "Loading an optical dipole trap," *Physical Review A*, vol. 6201, no. 1, 2000.

[106] G. Rempe, R. J. Thompson, H. J. Kimble, and R. Lalezari, "Measurement of ultralow losses in an optical interferometer," *Optics Letters*, vol. 17, no. 5, pp. 363–365, 1992.

[107] R. Blatt, "personal communication," 2002.

[108] P. L. Hansen and P. Buchhave, "Thermal self-frequency locking of a doubly resonant optical parametric oscillator," *Optics Letters*, vol. 22, no. 14, pp. 1074–1076, 1997.

[109] F. Jermann and J. Otten, "Light-induced charge-transport in linbo3fe at high light intensities," *Journal of the Optical Society of America B-Optical Physics*, vol. 10, no. 11, pp. 2085–2092, 1993.

[110] A. Douillet and J. T. Zondy, "Low-threshold, self-frequency-stabilized aggas2 continuous-wave subharmonic optical parametric oscillator," *Optics Letters*, vol. 23, no. 16, pp. 1259–1261, 1998.

[111] M. Hennrich, T. Legero, A. Kuhn, and G. Rempe, "Vacuum-stimulated raman scattering based on adiabatic passage in a high-finesse optical cavity," *Physical Review Letters*, vol. 85, no. 23, pp. 4872–4875, 2000.

[112] B. E. A. Saleh and M. C. Teich, *Fundamentals of photonics*, ser. Wiley series in pure and applied optics. New York: Wiley, 1991.

[113] W. D. Callister, *Materials science and engineering : an introduction*. New York: Wiley, 1985.

[114] R. W. P. Drever, J. L. Hall, F. V. Kowalski, J. Hough, G. M. Ford, A. J. Munley, and H. Ward, "Laser phase and frequency stabilization using an optical-resonator," *Applied Physics B-Photophysics and Laser Chemistry*, vol. 31, no. 2, pp. 97–105, 1983.

[115] E. Black, "Notes on the pound-drever-hall technique," *LASER INTERFEROMETER GRAVITATIONAL WAVE OBSERVATORY Technical Note*, 1998.

[116] W. L. Brogan, *Modern control theory*, 3rd ed. Englewood Cliffs, N.J.: Prentice Hall, 1991.

[117] G. Rempe, R. J. Thompson, R. J. Brecha, W. D. Lee, and H. J. Kimble, "Optical bistability and photon statistics in cavity quantum electrodynamics," *Physical Review Letters*, vol. 67, no. 13, pp. 1727–1730, 1991.

[118] J. Gripp, S. L. Mielke, L. A. Orozco, and H. J. Carmichael, "Anharmonicity of the vacuum rabi peaks in a many-atom system," *Physical Review A*, vol. 54, no. 5, pp. R3746–R3749, 1996.

[119] B. Nagorny, T. Elsasser, and A. Hemmerich, "Collective atomic motion in an optical lattice formed inside a high finesse cavity," *Physical Review Letters*, vol. 91, no. 15, pp. –, 2003.

[120] A. T. Rosenberger, L. A. Orozco, H. J. Kimble, and P. D. Drummond, "Absorptive optical bistability in 2-state atoms," *Physical Review A*, vol. 43, no. 11, pp. 6284–6302, 1991.

[121] P. Munstermann, T. Fischer, P. W. H. Pinkse, and G. Rempe, "Single slow atoms from an atomic fountain observed in a high-finesse optical cavity," *Optics Communications*, vol. 159, no. 1-3, pp. 63–67, 1999.

[122] P. Munstermann, T. Fischer, P. Maunz, P. W. H. Pinkse, and G. Rempe, "Observation of cavity-mediated long-range light forces between strongly coupled atoms," *Physical Review Letters*, vol. 84, no. 18, pp. 4068–4071, 2000.

[123] W. Alt, D. Schrader, S. Kuhr, M. Muller, V. Gomer, and D. Meschede, "Single atoms in a standing-wave dipole trap," *Physical Review A*, vol. 67, no. 3, 2003.

[124] T. A. Savard, K. M. OHara, and J. E. Thomas, "Laser-noise-induced heating in far-off resonance optical traps," *Physical Review A*, vol. 56, no. 2, pp. R1095–R1098, 1997.

[125] J. D. Miller, R. A. Cline, and D. J. Heinzen, "Photoassociation spectrum of ultracold rb atoms," *Physical Review Letters*, vol. 71, no. 14, pp. 2204–2207, 1993.

[126] K. L. Corwin, S. J. M. Kuppens, D. Cho, and C. E. Wieman, "Spin-polarized atoms in a circularly polarized optical dipole trap," *Physical Review Letters*, vol. 83, no. 7, pp. 1311–1314, 1999.

[127] V. G. Minogin and V. S. Letokhov, *Laser light pressure on atoms.* New York: Gordon and Breach Science Publishers, 1987.

[128] L. Landau and E. Lifschitz, *Mechanics.* Oxford, New York: Pergamon Press, 1969.

[129] S. Friebel, C. D'Andrea, J. Walz, M. Weitz, and T. W. Hansch, "Co2-laser optical lattice with cold rubidium atoms," *Physical Review A*, vol. 57, no. 1, pp. R20–R23, 1998.

[130] O. J. Luiten, M. W. Reynolds, and J. T. M. Walraven, "Kinetic theory of the evaporative cooling of a trapped gas," *Physical Review A*, vol. 53, no. 1, pp. 381–389, 1996.

[131] K. BergSorensen, "Kinetics for evaporative cooling of a trapped gas," *Physical Review A*, vol. 55, no. 2, pp. 1281–1287, 1997.

[132] P. A. Barton, C. J. S. Donald, D. M. Lucas, D. A. Stevens, A. M. Steane, and D. N. Stacey, "Measurement of the lifetime of the 3d d-2(5/2) state in ca-40(+)," *Physical Review A*, vol. 6203, no. 3, pp. art. no.–032 503, 2000.

[133] M. Stephens, K. Lindquist, and C. Wieman, "Optimizing the capture process in optical traps," *Hyperfine Interactions*, vol. 81, no. 1-4, pp. 203–215, 1993.